LOAD-ENHANCED LAMB WAVE METHODS FOR THE *IN SITU* DETECTION, LOCALIZATION, AND CHARACTERIZATION OF DAMAGE

A Thesis
Presented to
The Academic Faculty

by

Xin Chen

In Partial Fulfillment
of the Requirements for the Degree
Doctor of Philosophy in the
School of Electrical and Computer Engineering

Georgia Institute of Technology
May 2015

LOAD-ENHANCED LAMB WAVE METHODS FOR THE *IN SITU* DETECTION, LOCALIZATION, AND CHARACTERIZATION OF DAMAGE

Approved by:

Professor Jennifer E. Michaels,
Advisor
Committee Chair
School of Electrical and Computer Engineering
Georgia Institute of Technology

Professor Gregory D. Durgin
School of Electrical and Computer Engineering
Georgia Institute of Technology

Professor Thomas E. Michaels
Co-Advisor
School of Electrical and Computer Engineering
Georgia Institute of Technology

Professor Ying Zhang
School of Electrical and Computer Engineering
Georgia Institute of Technology

Professor Aaron D. Lanterman
School of Electrical and Computer Engineering
Georgia Institute of Technology

Professor Massimo Ruzzene
School of Aerospace Engineering
Georgia Institute of Technology

Date Approved: 6 January 2014

To my grandparents,

Zengshou and Yunxian

without whom this thesis would never have been written.

ACKNOWLEDGEMENTS

First and foremost, I would like to express my sincere gratitude to my advisors, Dr. Jennifer E. Michaels and Dr. Thomas E. Michaels, for their continuous support throughout my graduate studies. I want to thank Jenny for guiding me to the field of structural health monitoring, coaching me in methodologies for data analyzing and problem troubleshooting, and helping me with my technical writing skills. Her influence on me is far beyond the academic research and makes me a better person. I also want to thank Tom for his help in designing and conducting experiments, without which this thesis would never be finished. His insight on the physics behind experiments provides significant value to this research.

Thank you to all the other committee members, Dr. Aaron D. Lanterman, Dr. Gregory D. Durgin, Dr. Ying Zhang, and Dr. Massimo Ruzzene. Your time, efforts, and suggestions are sincerely appreciated.

It is a great honor for me to work with all the colleagues in QUEST lab. The friendship of Ross Levine is much appreciated and has led to many interesting and good-spirited discussions relating to this research. I am also grateful to our former post-doc, Dr. Sang Jun Lee, for teaching me all the techniques to conduct experiments and helping me form a good habit to keep a lab notebook. I want to further extend my thanks to Leo, Ler, Navneet, Fan, Honglei, Xander, Westin and all the other colleagues with whom I enjoyed sharing this invaluable experience at Georgia Tech.

Last, but not least, I would like to thank my father Jinlong, because of whom I chose the electrical engineering as my major, and my mother Liying, who greatly influenced my personality that makes me the person I am today. Great thanks to my girlfriend Yi for her love and encouragement. It is not easy to keep a long-distance

relationship but I am glad we made it. I also owe my gratitude to Kuni, Yang, Ningxin, Jing, and all my other friends both in the States and in China for their continuous support.

The work reported in this thesis was sponsored by the American Society for Nondestructive Testing (ASNT) in the form of a Graduate Fellowship. The load-dependent data were acquired as part of Contract No. FA8650-09-C-5206 from the Air Force Research Laboratory [1].

TABLE OF CONTENTS

DEDICATION . . . . . **iii**

ACKNOWLEDGEMENTS . . . . . **iv**

LIST OF TABLES . . . . . **x**

LIST OF FIGURES . . . . . **xi**

SUMMARY . . . . . **xiv**

I INTRODUCTION **1**

1.1 Background 1

1.2 Motivation and Research Goals 3

1.3 Contributions 5

1.4 Thesis Organization 6

II LITERATURE REVIEW **8**

2.1 Lamb Waves Background 8

2.2 Generation and Reception of Lamb Waves 11

2.2.1 Contact Transducers 12

2.2.2 Non-Contact Transducers 13

2.3 Interactions of Lamb Waves with Scatterers 14

2.4 Lamb Wave SHM Methods 18

2.4.1 Lamb Wave Detection 19

2.4.2 Lamb Wave Localization and Characterization 20

2.5 Environmental Effects on Lamb Wave SHM 23

2.5.1 Temperature Effects on Lamb Waves 23

2.5.2 Surface Wetting Effects on Lamb Waves 24

2.5.3 Load Effects on Lamb Waves 25

2.5.4 Load Effects on Wave-Based Methods for Defect Detection . 27

2.6 Research Context 28

III SCATTERING PATTERN ESTIMATION AND VALIDATION 30

3.1 Estimation Methodology 30

3.1.1 Signal Preprocessing 31

3.1.2 Initial Scattering Values 32

3.1.3 Radial Basis Function Interpolation 33

3.2 Experimental Setup 35

3.2.1 Sparse Array Measurements 35

3.2.2 Laser Vibrometer Measurements 37

3.3 Estimation Results 38

3.3.1 Signal Preprocessing 38

3.3.2 Initial Scattering Values 41

3.3.3 Estimated Scattering Matrix 42

3.4 Validation by Laser Measurements 45

3.5 Discussion on Estimation Errors 47

3.6 Summary 51

IV APPLICATIONS OF THE SCATTERING PATTERN ESTIMATION METHODOLOGY 53

4.1 Sparse Array Design Based upon Scattering Pattern Estimation . . . 53

4.1.1 Scattering Pattern Approach to Array Design and Analysis . 54

4.1.2 Analysis of Typical Array Configurations 56

4.1.3 Monte Carlo Simulation Results 57

4.2 Sparse Array Imaging with Estimated Scattering Patterns 62

4.2.1 Experimental Setup 62

4.2.2 Analysis Methodology 64

4.2.3 Results 67

4.3 Summary 70

V LOAD-ENHANCED METHODS FOR THE *IN SITU* DETECTION, LOCALIZATION, AND CHARACTERIZATION OF SCATTERERS 72

5.1 Analysis Methodology 72
5.2 Fatigue Test #1: Simple Plate 73
5.2.1 Experimental Setup 73
5.2.2 DAS Imaging with Damage-Free Reference Signals 75
5.2.3 Crack Detection Using Load-Differential DAS Imaging 80
5.2.4 Crack Localization Using Load-Differential DAS Imaging . . 84
5.2.5 Features Extracted from Load-Differential Images for Automated Crack Detection 85
5.2.6 Crack Characterization Using Load-Differential MV Imaging 89
5.3 Fatigue Test #1: Plate with a Bonded Doubler and Tightened Bolts 95
5.3.1 Experimental Setup 95
5.3.2 Crack Detection Using Load-Differential DAS imaging 96
5.3.3 Automated Crack Detection Using Features Extracted from Load-Differential DAS Images 100
5.3.4 Crack Characterization Using Load-Differential MV Imaging 102
5.4 Fatigue Test #2: Plate with Four Drilled Through-Holes 108
5.4.1 Experimental Setup 108
5.4.2 Crack Detection Using Load-Differential DAS imaging 110
5.4.3 Automated Crack Detection Using Features Extracted from Load-Differential DAS Images 113
5.4.4 Crack Characterization Using Load-Differential MV Imaging 114
5.5 Fatigue Test #3: Plate with an Initially Bonded Doubler 116
5.5.1 Experimental Setup 116
5.5.2 Crack Detection Using Load-Differential DAS imaging 118
5.5.3 Automated Crack Detection Using Features Extracted from Load-Differential DAS Images 118
5.5.4 Crack Characterization Using Load-Differential MV Imaging 120
5.6 Summary 121

VI CONCLUSIONS AND RECOMMENDATIONS 123

6.1 Conclusions 123
6.2 Recommendations for Future Work 125

LIST OF TABLES

1 Summary of data sets acquired for demonstrating the use of estimated scattering patterns for defect characterization 63

2 Summary of data sets acquired from fatigue test #1 : simple plate . . 75

3 Summary of data sets acquired from fatigue test #1: added geometric complexities 96

4 Summary of data sets acquired from fatigue test #2 109

5 Summary of data sets acquired from fatigue test #3 117

LIST OF FIGURES

1 Phase velocity dispersion curves for a 6061-T6 aluminum plate 11

2 Illustration of incident and scattered angles 15

3 Experimental setup for scattering pattern estimation 36

4 Experimental setup for laser vibrometry measurements to validate estimated scattering patterns 38

5 Lamb wave propagation loss curves 39

6 Results of signal preprocessing on sparse array data 40

7 Examples of extracting initial scattering values from the envelope of residual signals 41

8 The estimated scattering matrix of a 10 mm notch originating from a 5 mm diameter through-hole at a $-90°$ orientation for the 100 kHz, 5 cycle A_0 mode 43

9 Estimated scattering matrices of 1.6 mm, 5.4 mm, 10 mm, and 14 mm notches originating from a 5 mm diameter through-hole at a $-90°$ orientation for the 100 kHz, 5 cycle A_0 mode 44

10 Transducer and bonding variations from laser measurements 46

11 Validation results of the estimated scattering patterns 48

12 The effect of shape parameter on estimation results 51

13 The scattering matrix obtained from FEM used for sparse array design 55

14 Analysis of the typical array configuration #1 58

15 Analysis of the typical array configuration #2 59

16 Analysis of the typical array configuration #3 60

17 Array configurations from the results of the Monte Carlo simulation . 61

18 Experimental setup for demonstrating the use of estimated scattering patterns for defect characterization 63

19 Estimated scattering matrices of 4 mm and 8 mm notches originate from a 5 mm diameter through-hole at a $-50°$ orientation for the 100 kHz, 3 cycle A_0 mode 67

20 DAS and MV images for the two notches originating from a through-hole in the small plate 68

21 Orientation curves for the 4 mm and 8 mm notches 70

22 Experimental setup for fatigue test #1: simple plate 74

23 DAS images of the through-hole under matched loads 76

24 DAS images of the through-hole under mismatched loads 76

25 DAS images of the 5.4 mm through-thickness fatigue crack under matched loads 78

26 DAS images of the 5.4 mm through-thickness fatigue crack under mismatched loads (current data are under 0 MPa load) 79

27 DAS images of the 5.4 mm through-thickness fatigue crack under mismatched loads (reference data are under 0 MPa load) 79

28 Pair-wise load-differential signals 81

29 Load-differential signals from data set 10 of fatigue test #1 82

30 Load-differential DAS images from data sets 1–14 of fatigue test #1 . 83

31 Load-differential DAS images from data set 12 of fatigue test #1 . . 84

32 Load-differential signals at the maximum differential load levels for data sets 1–14 of fatigue test #1 86

33 Automated crack detection using the total energy feature from the load-differential images of fatigue test#1 87

34 Automated crack detection using the 2-D correlation coefficient feature from the load-differential images of fatigue test#1 89

35 An estimated scattering matrix of a 4 mm notch originate from a 5 mm diameter through-hole at a 180° orientation for the 100 kHz, 3 cycle A_0 mode and a uniformly omnidirectional scatterer 90

36 DAS and MV images of the 5.1 mm through-hole at zero load and the 5.4 mm crack using 30–40% load-differential signals 91

37 Orientation curves generated using the scattering matrix of a 4 mm notch for the through-hole vs. the partially opened crack 94

38 Orientation curves generated using scattering matrices of a 4 mm notch and an 8 mm notch for the case of two cracks 94

39 Experimental setup for fatigue test #1: the simple plate with a bonded doubler and tightened bolts 95

40 Load-differential DAS images from data sets 14–24 of fatigue test #1 98

41 Load-differential DAS images from data sets 25–35 of fatigue test #1 99

42 Automated crack detection using the total energy feature for data sets 14–35 of fatigue test #1 101

43 Automated crack detection using the 2-D correlation coefficient feature for data sets 14–35 of fatigue test #1 101

44 Orientation curves for the cases of two large cracks with vs. without the glued-on doubler 104

45 Orientation curves for the cases of two large cracks after a center hole drilled through the doubler vs. with a tightened bolt through the center hole 104

46 Orientation curves for the cases of two large cracks with a loosened bolt through the center hole vs. with three tightened bolts 106

47 Orientation curves for the cases of two large cracks with tightened bolts in both two side holes vs. with loosened bolt in side hole 1 and tightened bolt in side hole 2 106

48 Orientation curves for the cases of two large cracks with tightened bolt only in the center hole vs. with no bolts in three holes 107

49 Experimental setup for fatigue test #2: plate with four through-holes 108

50 Load-differential DAS images from data sets 3–16 of fatigue test #2 . 111

51 Load-differential DAS images from data sets 16 and 18 through 24 of fatigue test #2 with temperature variations 112

52 Automated crack detection using the load-differential features for fatigue test #2 113

53 Orientation curves for the cases of four through-holes with multiple cracks 114

54 Orientation curves for two data sets of fatigue test #2 115

55 Experimental setup for fatigue test #3: plate with an initially bonded doubler 116

56 Load-differential DAS images from all data sets of fatigue test #3 . . 119

57 Automated crack detection using the load-differential features for fatigue test #3 120

58 Orientation curves for the cases of cracks vs. partially disbonding at plate edge 121

SUMMARY

The performance and safety of engineering structures used in aerospace, civil, and mechanical applications rely heavily on the early detection of defects. One tool that can be used for this purpose for plate-like structures is guided waves, called Lamb waves in plates, to a large degree because of the ability of such waves to travel relatively long distances while maintaining usable amplitudes. A widely used technique for guided wave structural health monitoring is baseline subtraction, where defect information is obtained by subtracting a baseline signal recorded when the structure is in a known state from the current signal of interest. In practice, engineering structures are usually subject to varying and uncontrolled stresses (i.e., loads). It is well-known that varying loads can adversely affect the performance of baseline subtraction methods and obscure the detection of damage. However, applied tensile loads open cracks and can enhance their detectability.

The objective of this thesis is to investigate a methodology that leverages effects of applied loads to enable the *in situ* detection, localization, and characterization of damage in metallic plate-like structures using Lamb waves. A baseline-free load-differential method using the delay-and-sum imaging algorithm is proposed for defect detection and localization. The term "load-differential" refers to the comparison of recorded ultrasonic signals at various levels of stress. Defect characterization is achieved by incorporating expected scattering information of guided waves interacting with defects into the minimum variance imaging algorithm, and a method for estimating such scattering patterns from the measurements of a sparse transducer array is developed. The estimation method includes signal preprocessing, extracting initial scattering values from baseline subtraction results, and obtaining the complete

scattering matrix by applying radial basis function interpolation. The factors that cause estimation errors, such as the shape parameter used to form the basis function and the filling distance used in the interpolation, are discussed.

To demonstrate the feasibility of the proposed methodology, three sets of experiments were performed on aluminum plate specimens. The first set was designed to demonstrate the efficacy of the scattering pattern estimation method, which was validated by wavefield measurements using laser vibrometry. The results show that estimation results agree reasonably well with the laser measurements, particularly considering the limited amount of data available from a sparse array. The second set of experiments was designed to demonstrate applications of the scattering pattern estimation method. One application is to aid in the design of sparse arrays, where the estimation method is applied to re-samples of a known scattering matrix based on assumed array configurations to evaluate their performance. The other application is to characterize defects by incorporating the estimated scattering patterns into adaptive imaging algorithms. It is shown that the scattering patterns of notches of different lengths at one orientation estimated from one plate can be used to obtain size and orientation information of similar notches at a different orientation in another plate. Such results serve as a stepping stone to the third set of experiments, which consists of a series of fatigue tests on specimens with different complex geometries that mimic real engineering structures. The results from fatigue tests show that the load-enhanced method is capable of detecting cracks, providing reasonable estimates of their localizations and orientations, and discriminating them from drilled holes, disbonds, and fastener tightness variations. At the end, future directions for research to make this methodology more robust and deployable in field applications are suggested.

CHAPTER I

INTRODUCTION

This chapter first provides a brief description of the background of ultrasonic nondestructive evaluation, especially *in situ* methods utilizing guided waves; these waves are called Lamb waves in plates. Motivated by the practical demands of field applications, research goals are proposed next that aim to address two problems. The first problem is that of efficiently obtaining Lamb wave scattering information from sparse transducer array measurements, and the second one is improving the performance of Lamb wave *in situ* methods under varying environmental conditions. The findings with regard to the first problem provide useful *a priori* information for the second. Lastly, research contributions are summarized and the organization of the remaining chapters is provided.

1.1 Background

Because of safety and environment concerns, the health status of engineering structures has become a major issue across a wide range of industries. In the aviation industry, the requirements to remain aging fleets in service even beyond their initial design service lives keep increasing [2]. For civil infrastructures, the need to improve the effectiveness of maintenance and inspection for large structures such as dams, buildings, and bridges continues to grow [3]. In the petrochemical and nuclear industries, concerns about severe environmental and economic impacts caused by structure failures have also drawn much attention [4]. Therefore, the demand for robust, sensitive, and inexpensive structural integrity assessment is growing rapidly and thus has promoted the continual development and improvement of nondestructive evaluation (NDE) methods; i.e., methods capable of assessing the state of structures without

affecting their function.

The development of NDE has gone through three stages: nondestructive testing (NDT) [5], quantitative NDE [6], and *in situ* NDE, also called structural health monitoring (SHM) [7, 8]. As the latest development, the subject of SHM has gained considerable attention over the past two decades. SHM refers to the process of the nondestructive, autonomous monitoring of structural conditions by means of permanently attached or embedded sensor systems. Compared to conventional NDT/NDE methods, which are usually performed off-line and by schedule, SHM offers the promise of real-time structural assessment and condition-based maintenance. In addition, diagnostic information about structures from sensor data can be used for prognosis of remaining service life and can facilitate decision processes about future usage and maintenance.

A variety of techniques, such as eddy current, ultrasound (sound waves vibrating at a frequency higher than 20 kHz), magnetic particle inspection, and X-ray, have been adopted for the purpose of SHM [5, 6, 7]. Among them, ultrasonic methods are considered to be highly flexible and robust because of their sensitivity to both surface and subsurface discontinuities [5]. Moreover, ultrasonic methods often offer both contacting and non-contacting testing approaches for most types of materials from bio to metallic to ceramic [6]. Although ultrasonic theory and techniques can be quite complex, the basic concept behind ultrasonic NDE/SHM is simple. During propagation, ultrasonic waves interact with solid structures, and such interactions can be used to detect and characterize defects that occur both internally and on the surface.

Based upon the excitation sources, ultrasonic SHM can be broadly classified into two categories: passive and active [7]. For passive SHM methods, excitations are "natural" sources such as impacts, ambient vibration, or acoustic emission results (e.g., those from crack generation and growth); passive SHM systems only need sensors

to "listen" to these sources. Active SHM methods, on the other hand, need both actuators and sensors to both send the excitation into structures and receive responses from the interactions between the excitation and the structure. Therefore, active methods are able to offer more flexibility than passive methods in terms of varying excitation signal characteristics, such as duration and frequency, for specific diagnosis purposes, and in terms of controlling how often measurements are performed. Active methods also have more freedom in terms of designing sensor array configurations and implementing array signal processing algorithms to obtain better detection.

One particularly attractive method for the active ultrasonic SHM is through the use of guided waves, which are mechanical stress waves that propagate along structures with well defined boundaries and are further guided by such boundaries during propagation. In plate-like structures, guided waves are called Lamb waves after the mathematician Horace Lamb [9], who first predicted analytically their existence in the 1910s. Later in 1967, Viktorov [10] started to investigate the use of Lamb waves for ultrasonic testing. The understanding of Lamb waves and their applications for NDE and SHM have advanced substantially since the 1990s. Various Lamb wave SHM methods based upon sensor arrays have been proposed, among which, the sparse, or spatially-distributed, array is considered to be the most suitable for practical deployment because of the small number of transducers it required compared to other array configurations. Sparse array imaging algorithms have demonstrated their success in defect detection, localization, and characterization [11, 12, 13, 14, 15].

1.2 Motivation and Research Goals

It has been shown that Lamb waves have reasonable sensitivity to defects of interest, but even in the laboratory there are unavoidable issues with signal complexity and environmental sensitivity. Therefore, significant research efforts have been made to better understand Lamb wave signals, facilitate data interpretation, and enhance

performance of Lamb wave SHM methods under varying environmental conditions.

One major complexity of Lamb wave signals results from their interaction with structural features. Engineering structures usually have multiple features including stiffeners, ribs, fastener holes, and cut-outs. As Lamb waves travel in these structures, scattering occurs when they encounter both structural discontinuities and damage. Such scattering information serves as the basis for many guided wave SHM methods and the knowledge about it can greatly contribute to the success of practical applications.

Prior work has employed finite element modeling or full wavefield scanning to obtain scattering information either numerically or experimentally. However, because of computational or experimental issues, these approaches may be impractical. One practical method is to use the measurements from sparse transducer arrays, which essentially interrogate the scatterers from specified incident and scattered angles. Therefore, the first goal of this thesis is to develop a methodology that uses measurements from sparse arrays to investigate scattering of Lamb waves from different types of scatterers.

The knowledge of Lamb wave scattering from typical scatterers provides the possibility to analyze more complicated Lamb wave signals obtained from real structures with complex geometries and under varying environmental conditions for damage detection and characterization. To facilitate signal interpretation, a common practice for Lamb wave SHM is to use baseline subtraction, where the signals recorded when the structure is in a known (usually undamaged) state are subtracted from the current signals of interest [16, 17, 18]. Any differences in the residual signals are assumed to arise from the interactions between incident Lamb waves and newly introduced damage. While baseline subtraction has met with success under controlled conditions to facilitate damage detection and localization, its performance is adversely affected by uncompensated environmental variations.

Temperature changes, even as small as ∼1°C, can significantly affect baseline subtraction results. Temperature compensation methods have enabled detection and localization of reasonably small artificial defects (∼5-10 mm) via baseline subtraction, but it is unrealistic to think that they will work for other types of changing conditions. Besides temperature, operational loads (i.e., stresses) are the environmental effect that is most likely to have a significant adverse effect on Lamb wave signals. In an undamaged structure, loads cause anisotropic dimensional and wave speed changes, and can also cause boundary conditions of built-up structures to change. In a damaged structure, load changes can cause cracks to open and close, poor bonds to make and break contact, and other less obvious effects that may occur prior to formation of macro-cracks.

The effects of load variations on Lamb waves have been extensively investigated by researchers across different disciplines. However, most work has focused on either examining the load effects on Lamb wave velocity, or vice versa; i.e., determining the applied load by measuring the change of wave velocity. Few studies have considered using load effects to improve the performance of Lamb wave SHM for defects of certain types. The second goal of the thesis is to develop algorithms or methods that are sensitive to damage but not load variations. The proposed method should be able to not only detect and localize defects, but also characterize them.

1.3 Contributions

The first and most important contribution of this research is a "baseline-free" *in situ* Lamb wave method that utilizes load effects for enhanced detection, localization, and characterization of damage. The research results demonstrate the feasibility of using load-enhanced methods for fatigue crack monitoring in structures with complex geometries.

The second contribution of this research is that it develops a methodology to obtain scattering patterns using limited measurements from an *in situ* sparse transducer array. This approach is efficient in terms of both measurement time and computational requirements.

The third contribution of this thesis is that it provides estimated scattering matrices for notches of different lengths emanating from a through-hole for the A_0 Lamb wave mode, and presents high angular resolution scattering patterns obtained from laser measurements for one notch length.

The fourth contribution of this thesis is that it proposes a metric to evaluate the performance of a transducer array configuration based on its ability to capture scattering information for a specific defect.

The fifth contribution of this thesis is that it examines the performance of adaptive (minimum variance) sparse array imaging algorithms for locating and characterizing defects on structures with complex geometries that mimic realistic engineering components.

1.4 Thesis Organization

The remainder of the thesis is organized as follows. Chapter II presents a review of the existing literature to provide a more profound background and foundation for the thesis. The literature survey focuses on prior research on Lamb wave SHM methods for defect monitoring, especially those based upon sparse array measurements and that address the effects of environmental changes. The objective and scope of the research presented in this thesis is placed in the context of the review work.

Chapter III introduces the methodology for estimating Lamb wave scattering patterns using measurements from a sparse transducer array. The methodology consists of signal preprocessing for Lamb wave propagation loss compensation, extracting initial scattering values, and applying interpolation algorithms to obtain the complete

scattering matrix. The estimation results for a notch originating from a through-hole in an aluminum plate is validated by laser vibrometry wavefield measurements. Factors influencing the estimation error are discussed. Large portions of this chapter can be found in Chen *et al.* [19], which is a culmination of the work reported in [20].

Chapter IV demonstrates two applications of the scattering pattern estimation methodology. The first one is to aid in the design of sparse arrays, where the estimation method is applied to re-samples of a known scattering matrix based on assumed array configurations to evaluate their performance. The second one is to characterize defects, where the estimated scattering patterns are incorporated into minimum variance imaging algorithms to obtain orientation and approximate size estimates of notches. The main content of this chapter has been reported in Chen *et al.* [21, 22].

Chapter V investigates the positive and negative effects of loads on Lamb wave sparse array imaging algorithms and proposes a load-enhanced method for fatigue crack detection, localization, and characterization. Both conventional and adaptive sparse array imaging algorithms are considered and the efficacy of the proposed load-enhanced method is demonstrated using data from a series of fatigue tests conducted on aluminum plate specimens with increasing geometric complexity. Large portions of the research discussed in this chapter can be found in Chen *et al.* [1, 23, 24, 25], which is an extension of the work reported in [26, 27].

Chapter VI concludes this thesis and gives recommendations for future research.

CHAPTER II

LITERATURE REVIEW

The purpose of this literature survey is to summarize prior research on Lamb wave SHM methods, especially those based upon sparse array measurements and that address the effects of environmental changes. Section 2.1 gives a brief review of Lamb waves. Section 2.2 introduces common techniques for Lamb wave generation and reception. Section 2.3 provides a thorough discussion on the scattering of Lamb waves from different scatterers in metallic plates. Section 2.4 reviews Lamb wave SHM methods based upon sparse array measurements, and Section 2.5 discusses the effects of environmental changes on Lamb wave signals and the corresponding compensation techniques. Section 2.6 defines the objective and scope of the research presented in this thesis, which is placed in the context of prior work.

2.1 Lamb Waves Background

In infinite, isotropic solids, two types of ultrasonic wave modes can exist, namely longitudinal waves (also known as pressure waves, or P-waves) and transverse waves(also known as shear waves, or S-waves); both are bulk elastic waves. Guided waves are elastic waves that travel along structures with boundaries. These boundaries, which are assumed to have infinite length, guide the wave propagation. Based upon the boundary conditions, guided waves can be classified into several different types. Rayleigh waves are surface waves that travel along the stress-free boundary of a solid body [28]. Lamb waves propagate in a solid thin plate or layer with stress-free boundaries [9]. Love waves exist and travel in a layer on a half space [29] while Stoneley waves propagate at the interface of two solid half-spaces [30]. Further analytical details of guided wave propagation can be found in the literature [10, 31].

Lamb waves have been a subject of extensive research because of the abundance of plate-like structural configurations in industry. Compared to bulk elastic waves, these waves can propagate relatively long distances with low attenuation, and thus maintain sensitivity to damage [17, 32]. The strict definition of Lamb waves given in [9] confined the components of particle motion to the direction of the plate normal (z-direction) and the direction of wave propagation (x-direction). A more general definition usually includes the shear-horizontal (SH) waves, which have the particle motion in the y-direction (horizontally-polarized). Here, the term "Lamb waves" is used only to refer to its strict definition; i.e., the SH waves are not considered.

In spite of their advantages over bulk waves, Lamb waves are notable for their multi-modal and highly dispersive nature. In linear, isotropic plates, an infinite number of Lamb wave modes can exist [10]. These infinite modes can be categorized into two classes, namely symmetric modes and antisymmetric modes, depending on their through-thickness displacement profile. Except for the zero-order modes, each mode exists only above certain "nascent frequencies", which are defined as:

$$f = \frac{nc}{2h}, \tag{1}$$

where n is a positive integer, h is the thickness of the plate, and c is the velocity of the longitudinal (c_l) or transverse (c_t) wave. The fundamental symmetrical (S_0) and antisymmetric (A_0) modes can be considered to have nascent frequencies of zero, and they exist over the entire spectrum. In practice, these two modes (S_0 and A_0) are most commonly used for Lamb NDE and SHM at lower frequencies, as higher frequencies generate multiple modes and make signals significantly more difficult to analyze. Moreover, it is often possible to select a specific frequency such that a transducer is "tuned" to generate a dominant one of the two fundamental modes, which can further ease data interpretation [32].

All Lamb wave propagation modes are dispersive, meaning that their propagation velocity depends on not only the properties of the medium (elastic constants and density), but also frequency (or wavelength). For the propagation of Lamb waves, the key effect of dispersion is to stretch the wave packets and thus determine the spatial resolution of the excitation, especially in long range Lamb wave SHM [33]. Therefore, a common practice is to use a narrow-band tone burst excitation with the desired center frequency and select a specific number of cycles to obtain the best spatial resolution [34, 35].

The relationship between wave velocity of each mode and frequency can be described by a dispersion curve. Among several different forms, the most practical curve expresses the wave velocity (the phase velocity c_p or the group velocity c_g) as a function of fh, the frequency-thickness product [36]. As an example, the phase velocity dispersion curves for a 6061-T6 aluminum plate is shown in Figure 1, where both the multi-modal and dispersive nature of Lamb waves can be clearly seen. These dispersion curves provide critical information, such as frequencies under which a specific mode is almost non-dispersive or most dispersive, that can further guide the design of excitation signals for Lamb wave SHM [32, 34].

As Lamb waves propagate in plate-like structures, there are four main factors that can contribute to the loss of amplitude of Lamb waves with distance [37]:

- Geometric spreading loss (GSL)
- Wave packet spreading loss (WPSL)
- Material damping
- Wave leakage into adjacent media

GSL refers to the amplitude decreasing inversely with the square root of the propagation distance due to conservation of energy, and WPSL refers to the wave packet

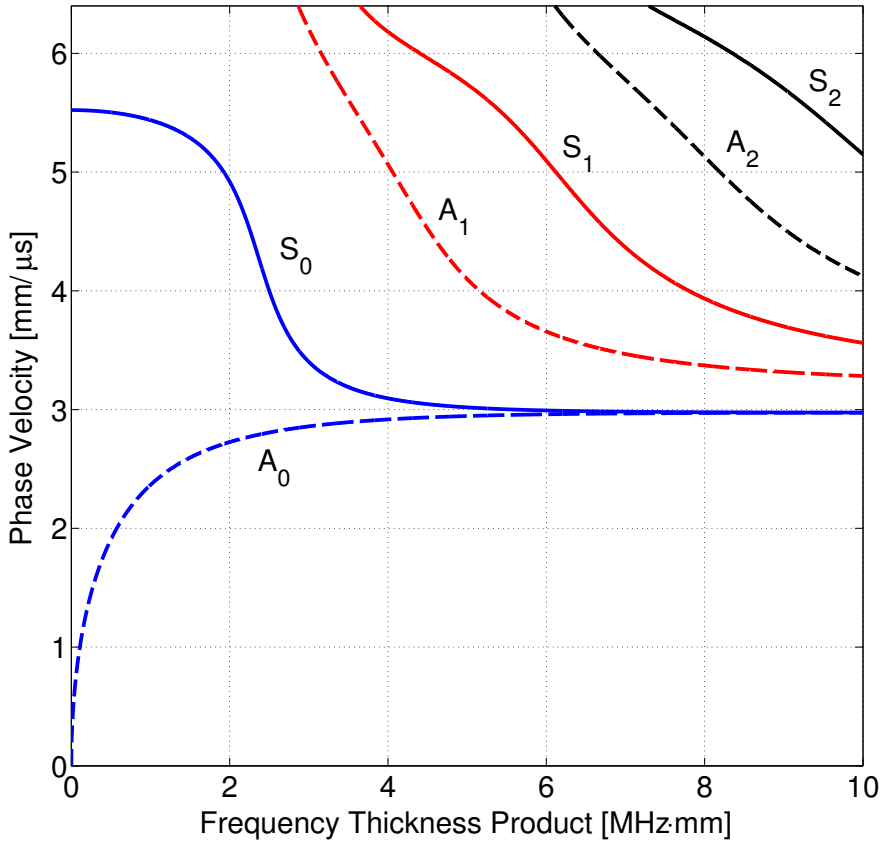

Figure 1: Phase velocity dispersion curves for a 6061-T6 aluminum plate.

spreading in time and thus decreasing in amplitude because of geometric dispersion. Material damping refers to wave energy absorption during propagation as a result of friction between material particles. This situation occurs when the medium is a viscoelastic material such as polymers and composites. For metals such as aluminum and steel, the material damping effect is negligible in the ultrasonic frequency range. The wave leakage factor can also be ignored when free boundary conditions are assumed.

2.2 Generation and Reception of Lamb Waves

Lamb waves can be transmitted and received by a variety of different transducers. These transducers are generally classified into two groups: contact and non-contact,

which are used in different measurement configurations. Depending on the configuration, transducers can either be used individually or in an array.

2.2.1 Contact Transducers

For the contact group, the most widely used transducers are those utilizing piezoelectric materials. Early development includes angle-beam transducers and comb-type transducers. Both of them function well for off-line maintenance checks but have limitations for SHM implementations. The angle-beam type is limited by its directionality and the comb-type by its narrow-band response; i.e., the wavelength is fixed by the transducer geometry. Piezoelectric disk transducers (PZT) [17, 32] and piezoelastic polymers (PVDF) [17, 38] are available in a very low profile ($\sim$0.1 mm for PZT and $\sim$9 μm for PVDF). Therefore, they can be readily embedded or surface-bonded to structures, and the relatively low cost makes them possible for widespread deployment. Another advantage of piezoelectric sensors for the purpose of SHM is the omni-directionality of excitation. Compared to the PZT disks, the PVDF films are more flexible and easy to handle, but less efficient in terms of generating Lamb waves.

Two active measurement configurations, namely pulse-echo and pitch-catch, are commonly used with Lamb wave transducers. The pulse-echo configuration uses only one transducer for both generating waves and receiving wave reflections from the structural discontinuities, while the pitch-catch configuration transmits Lamb waves by a transducer at one location and receives responses by a sensor at a different location.

Phased arrays [39, 40, 41] and sparse arrays [18, 42, 43] are the two major transducer array geometries for the pitch-catch configuration. A phased array contains a number of closely spaced transmitting elements that can be sequentially pulsed. By pulsing each element with specified time delays, the phased array can "steer" its beam in a particular direction so that constructive interference will maximize the

signal energy in that direction. The advantages of such arrays include beam shaping and compact installation; however, they can only receive back-scattered signals from structural features and usually need a fairly large number of transducers. An alternative configuration is to spatially distribute a small number of transducers over a large area, which is often referred to as a sparse array. For such an array geometry, both forward scattered and backscattered signals can thus be incorporated into signal processing algorithms to further enhance the performance of a Lamb wave SHM system, especially when the forward scattered waves are more sensitive to damage as compared to the backscattered ones [44]. Because the sparse array uses a limited number of sensors, the design of such an array is critical for its performance. The number of transducers and their configurations can be selected according to different criteria, such as to achieve high signal-to-noise ratio [45] and to improve imaging performance [46].

2.2.2 Non-Contact Transducers

The non-contact group includes electromagnetic acoustic transducers (EMAT), air-coupled transducers, and lasers. Unlike the contact transducers described previously, non-contact transducers do not need coupling media; therefore, they have the advantages of sensing waves without affecting their propagation and being able to work under extreme environmental conditions, e.g., very high temperatures.

EMAT transducers excite and detect Lamb waves based on the mechanisms of Lorentz force or magnetostriction [47]. As a result, their applications are limited to metallic or magnetic products. Air-coupled transducers can be used for generating and sensing Lamb waves in both metallic and composite materials [48]. However, they suffer from a relatively low efficiency as a result of a large impedance mismatch between the air and the object under testing. Laser-based ultrasonic technique also provides a noncontact method for Lamb wave generation and reception. Generation

is accomplished by illuminating a sample with a short laser pulse. The laser energy absorbed by the sample causes rapid localized temperature increase and results in thermal expansion. Reception is usually obtained by laser interferometers or vibrometers [49]. One important application using laser reception methods is to obtain high resolution wavefield data, which can be used to improve understanding of Lamb wave interactions with structural features and further aid damage detection [50, 51]. The disadvantages of laser ultrasonics include relatively low sensitivity, high initial cost, and the bulky size of the equipment. In fact, all the non-contact transducers are usually large in size and not amenable to permanent installation on a structure; therefore, they are more suitable for off-line Lamb wave NDT/NDE instead of being embedded for real-time SHM.

2.3 Interactions of Lamb Waves with Scatterers

Lamb wave signals received by sensors are complicated due to their dispersive and multi-modal nature; yet the complexity is even further increased by their interaction with structural features. As Lamb waves travel in a structure under test, scattering occurs when they encounter both structural discontinuities and damage. Knowledge of scattering behavior is thus very useful for the detection, localization, and characterization of damage.

Defect scattering behavior can be described by several approaches. The most common one is to use transmission and reflection coefficients, which are usually defined as the amplitude or energy ratio between the transmitted (or reflected) wave to the incident wave [52]. These coefficients essentially describe direct forward scattering and backscattering for a particular incident direction, but do not provide information about scattering at other angles. This limitation is addressed by the second method, which uses angular scattering patterns to describe the 360° dependence of the amplitude of the scattered wave for a given incident direction [53, 54]. As an extension of

angular scattering patterns, the third way describes the far-field scattering patterns of Lamb waves interacting with a scatterer by a scattering matrix, which is similar to the scattering coefficient matrix defined by Zhang *et al.* [55] for bulk waves. The scattering matrix contains amplitudes of scattered signals indexed by both incident and scattered angles, which are defined here as the angle between the direction of propagation and the x-axis as illustrated in Figure 2. Using these three approaches, the interactions of Lamb waves with several different types of scatterers have been investigated.

The simplest scatterer in a plate is a through-hole, and scattering of the S_0 and A_0 modes from a through-hole has been considered experimentally, analytically, and numerically. Fromme and Sayir [56] measured the scattering of the A_0 mode from a through-hole by a heterodyne laser interferometer, and found that the measurements agreed well with the results from both Kirchhoff and Mindlin plate theories. Diligent *et al.* [57] studied the interaction of the S_0 mode with a through-hole both analytically and using finite element (FE) analysis, both of which were validated by experiment, and confirmed that the reflection coefficient increased with the hole diameter and

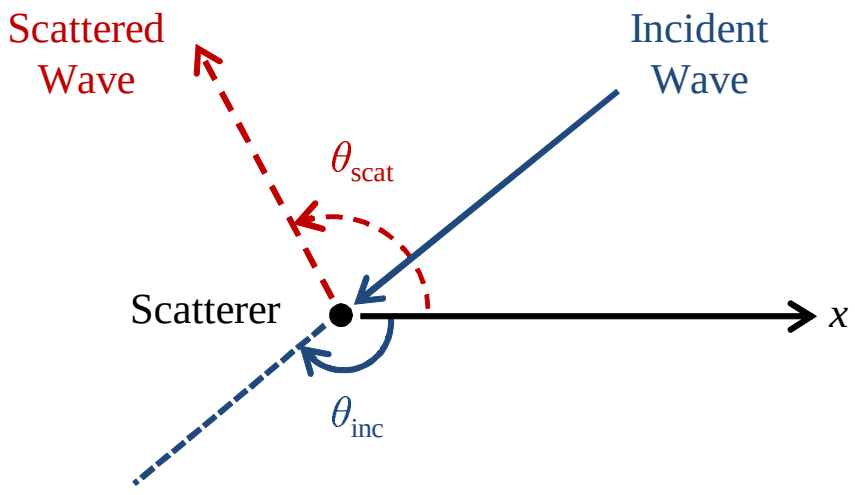

Figure 2: Illustration of scattering showing the incident and scattered angles.

decreased with the distance from the hole. McKeon and Hinders [58] modeled the scattering of the S_0 mode from a through-hole by adapting Mindlin higher order plate theory. Grahn [54] investigated the scattering of the S_0 mode from a part-through hole using both a 3D theory (based on mode expansions) and Kirchhoff plate theory, and presented angular scattering patterns for holes of various depths in a plate.

Another common type of scatterer is a notch, which is often used to simulate a fatigue crack. Alleyne and Cawley [59] studied the interaction of the A_0, S_0, and A_1 modes with a surface-breaking notch by FE simulation and verified the simulation with experiments, the emphasis being on establishing transmission coefficients. Lowe *et al.* [60, 61] examined the reflection, rather than the transmission, of both the S_0 and A_0 modes from rectangular notches of different widths and depths through FE time domain simulation together with experiments. Lu *et al.* [62] investigated the interaction of oblique-incident S_0 mode with through-thickness notches of different lengths in aluminum plates using FE method and validated the results with experiments. They concluded that the transmission coefficients decreased with notch length increment, while the reflection coefficients were a function of both notch length and ultrasonic wavelength. Fromme and Rogue [53] considered the scattering of the A_0 mode from part-through and through-thickness notches by laser measurements and FE simulation. They showed that the amplitude of scattered waves had a strong angular dependence, and recommended that such scattering directivity patterns be taken into account when developing guided wave arrays for SHM.

The scattering of Lamb waves from a notch or crack originating from a hole has also been investigated. Chang and Mal [63] used the global local FE method to analyze the guided waves interacting with a circular hole with two symmetrical cracks. They particularly examined the frequency spectra of the reflections for identifying the introduction of the cracks to a through-hole. Cho and Lissenden [64] examined the transmission coefficient of the S_0 mode with fatigue cracks generated from fastener

holes and showed a linear relationship between crack size and the transmission coefficient. Fromme and Sayir [65] considered Mindelin plate theory and finite difference methods to study the scattering of the A_0 mode from a rivet hole with a notch. They concluded the scattered field changed significantly even with the presence of a notch much smaller than the wavelength. Leong *et al.* [50] obtained the scattering field of the A_0 mode for a fatigue crack emanating from a spark-eroded notch using laser vibrometry, which demonstrated the potential of using laser measurements for crack detection.

Besides rivet holes and cracks, scatterers of more complexity, such as adhesive joints, weldments, and other irregular shaped defects, are common in real structures. Rokhlin [66] employed both analytical and experimental methods to study the interaction of Lamb waves with adhered metal lap joints. He examined the phase delay and transmission coefficients of different incident modes and frequencies for joint quality assessment. Lowe *et al.* [67] used FE analysis to investigate the transmission of the S_0, A_0, and A_1 modes across adhesively bonded lap joints. They showed that the transmission coefficients were influenced by both the bond length and bond thickness of the joint. Lanza di Scalea and Rizzo [68] experimentally studied the propagation of the A_0 mode in adhesively bonded joints and observed that the transmission increased with increasing overlap length and bond thickness.

Bendec *et al.* [69] investigated the scattering of Lamb waves with the weld region in steel sheets. They concluded the wave transmission coefficient is proportional to the cube of the weld diameter and showed scattering patterns of the S_0 mode for different mean diameters of the welded region with the same incident angle. Al-Nassar *et al.* [70] studied the scattering of Lamb waves from a normal rectangular strip weldment using a combined FE and analytical technique. They compared the reflection and transmission coefficients of different modes and concluded that the maximum sensitivity can be achieved by operating with specified modes and frequencies.

Cho *et al.* [71] used the boundary element method to study the scattering behavior of Lamb waves from defects of different shapes. They showed that classification and sizing of defects could be obtained by monitoring the reflection and transmission coefficients. Recently, Moreau *et al.* [72] considered the scattering of Lamb waves with irregular defects using the FE method. They measured the defect profile of a corroded area on a pipe (equivalent to a plate as its wall thickness was much smaller than its radius) and calculated the scattering matrices of the S_0 and A_0 modes when the S_0 mode was incident.

The interactions of Lamb waves with delaminations in composite plates have also been investigated using both transmission and reflection coefficients [73], and angular scattering patterns [74]. Because this thesis deals with defects in metallic structures, the scattering of Lamb waves from delaminations and other common types of scatterers in composite materials is not further reviewed.

2.4 Lamb Wave SHM Methods

The scattering of Lamb waves from defects and geometric features is manifested as echoes in signals recorded by the attached transducers. Ideally, the echoes associated with known structural features can be identified using a time delay law. Any echo that cannot be related to a known feature is generally assumed to be a defect. While such a scenario serves well for bulk wave NDE, it is not the case for Lamb wave SHM based upon omnidirectional transducers. Therefore, a common practice for Lamb wave SHM is using a baseline approach, where the "baseline" refers to signals recorded when the structure is in a known (usually undamaged) state. In theory, damage detection can be achieved by simply comparing baselines with current test signals. However, as the number of geometric features increases, their corresponding echoes may merge together masking the echoes from defects and thus making a direct comparison unrealistic. One feasible approach is to subtract the baselines from the

current test signals to obtain the residual signals. Then, a variety of signal processing algorithms can be applied to these residual signals for enhanced damage detection, localization, and characterization.

2.4.1 Lamb Wave Detection

The most straightforward method for damage detection is baseline comparison, where a coefficient, usually called a damage index (DI), is used to quantify signal differences. There are three primary types of such indices: DIs in the time domain, DIs in the frequency domain, and DIs in the joint time/frequency domain. Time domain DIs include normalized squared error, drop in correlation coefficients, energy decay rate, and local statistical features. These DIs have been applied for the detection of cracks and disbonds in both metallic and composite plates [18, 75, 76]. In the frequency domain, DIs computed based upon the spectra of the two signals have been shown to be able to identify various types of defects in both metallic and composite structural components with relatively complex geometries [77, 78]. In the joint time/frequency domain, both the short time Fourier transform [79] and wavelet transform [80] have been used to compute DIs to detect cracks in aluminum plates and delaminations in composite plates.

Various baseline-free algorithms have also been examined by researchers. Although these algorithms may not need previously stored baseline data, many of them still require to have some type of reference signals (sometimes referred as the instantaneous baseline) for signal comparison. Kim and Sohn [81] developed a baseline-free method for crack detection based on PZT polarization characteristics, where PZT transducers were strategically placed on both side of the plate such that Lamb wave mode conversion would occur in the presence of a crack. Anton *et al.* [82] proposed another damage detection method using instantaneous baseline measurements by placing transducers on a structure with equal distance from each other and using

pitch-catch Lamb wave propagation; features of the damaged sensor-actuator paths were compared with those of the undamaged paths for mass loading and corrosion detection. Time reversal acoustics has also been used for baseline-free damage detection [83, 84]. In a typical scenario of time reversal acoustics, two PZT traducers are used. The first one is excited with a known signal and the second one records the response. The recorded response is then reversed in time and retransmitted using the second transducer. This time, the response is recorded by the first transducer and compared to the original excitation signal. Any differences from the comparison could be indicative of nonlinearity caused by damage. The DIs introduced previously can also be used for these baseline-free methods for signal comparison. Note that baseline-free methods are usually applicable to structures with simple geometries or with some type of symmetry to avoid using prerecorded signals from a known state.

2.4.2 Lamb Wave Localization and Characterization

The idea of baseline comparison also plays a key role in many algorithms proposed for damage localization and characterization. Ideally, the first arrival of the residual signals obtained from baseline subtraction should correspond to a scattered echo from a damage site. If the propagation mode and group velocity are known, the distance from transducer to receiver through a damage site can be calculated from the time of the scattered arrival. However, to unambiguously locate the damage, it is necessary to triangulate using at least three transducer pairs. The amplitude of the residual signals, or equivalently the value of DIs, can also be used to quantify damage such as the size of cracks. But the information obtained from one transducer pair is insufficient to provide robust characterization. Therefore, transducer arrays are usually preferred for better performance.

Phased array beamforming is a well-developed technique for ultrasonic NDE and has been applied to Lamb waves for damage localization and characterization. Beam

forming refers to the process of adjusting the phasing of signals in a transducer array to provide desired directionality properties. Fromme *et al.* [40] used a 32-element PZT transducer array and applied the phased-addition algorithm with dispersion compensation to obtain the location and severity information of simulated corrosion damage in steel plates. Ostachowicz *et al.* [85] examined the performance of a 13-element PZT transducer phased array for locating multiple dents on an aluminum alloy specimen. Engholm and Stepinski [86] proposed an adaptive beamforming algorithm, namely minimum variance distortionless response (MVDR), for defect localization. They showed that multiple defects of different types in an aluminum plate can be located using a uniform rectangular array and a single transmitter using the MVDR. Other work related to the performance of phased arrays includes the investigations of element spacing, gain patterns, and higher resolution [87, 88].

Another commonly investigated technique for damage localization is Lamb wave tomography, which refers to imaging test structures by determining values of a spatially varying parameter of interest across their planar cross-sections. Popular selections of these parameters include time-of-flight, amplitude attenuation, and signal correlation coefficient [89]. The methods to determine the parameter values include filtered back-projection (FBP), fan beam FBP, and algebraic reconstruction techniques [89, 90, 91]. The efficacy of using Lamb wave tomography for defect localization and characterization has been demonstrated by imaging corrosion, impact damage, and notches in a variety of structures [13, 90].

As mentioned in Section 2.2.1, the sparse array offers a cost-effective solution for Lamb wave SHM. Research on sparse array signal processing for damage localization has been undertaken within recent years. In 2004, Wang *et al.* [42] proposed an imaging method that is applicable to sparse array Lamb wave measurements. The technique used the concept of synthetic time-reversal and is typically referred to as delay-and-sum (DAS) imaging; it is also called the ellipse algorithm since the locus

of a constant time curve is an ellipse. Michaels and Michaels [92] expanded this method to both raw and envelope-detected residual signals and applied a summation time window, rather than a single point in time, to generate detection images of artificial damage in aluminum plates. They further showed that images generated at multiple frequencies can be fused to obtain improved damage localization [11]. Michaels [18] also demonstrated that delay-and-sum imaging was able to provide sizing information of through-holes and notches in aluminum plates. Rather than using arrival time between two transducers for the ellipse algorithm, another sparse array imaging method considers the difference of time arrivals between two transducer pairs with the same transmitter [93, 94]. The image is constructed from the cross correlations of various signal pairs. This method is often referred to the hyperbola method since the locus of constant time differences between the same arrival at two receivers is a hyperbola.

Both the ellipse and hyperbola sparse array imaging methods are conceptually straightforward and computationally undemanding. However, their performance on defect characterization is limited and can be improved by incorporating certain *a priori* information of defects. One example is the minimum variance (MV) sparse array imaging introduced by Hall and Michaels [12]. Different from the MVDR phased array beamforming introduced in [86], the MV sparse array imaging is based on amplitude and incorporates scattering information of assumed defects. This method was shown to be able to characterize scatterers as to type (hole versus notch) and orientation (for the notches). Another example of using the *a priori* assumption that damage is sparse is the dictionary-based imaging method recently introduced by Ross and Michaels [14]. They showed this sparse reconstruction method outperformed DAS imaging in terms of image quality and defect localization.

In addition, methods based upon statistical approaches have been proposed. Flynn *et al.* [95] compared the performance of the Rayleigh maximum likelihood estimate

(RMLE) to that of seven previously reported localization methods. They showed the RMLE had the best performance, and is particularly effective using sparse arrays.

2.5 Environmental Effects on Lamb Wave SHM

The current state of the art clearly shows the promise of Lamb wave SHM; however, its performance on real structures and under realistic operating conditions has yet to be proven. One of the major challenges that limit Lamb wave SHM in practical applications is variations of environmental conditions. These variations can change measured signals, and thus affect the performance of the SHM system by masking defect indications or generating false alarms. Therefore, significant research efforts have been made to investigate the effects of environmental changes on Lamb waves and enhance the performance of Lamb wave SHM methods under varying environmental conditions.

2.5.1 Temperature Effects on Lamb Waves

The most common environmental condition is temperature. Temperature changes are unavoidable, even in laboratory, and they were shown to have a significant impact on Lamb wave signals [96, 97]. For single mode Lamb wave signals, the primary effect of a temperature change is a shift of the times of arrival (TOA) as a result of both the change in material properties and dimensions with temperature. Another effect is the amplitude change (particularly when the temperature change is large), which is caused by changes in the efficiency of the piezoelectric crystal. For Lamb SHM methods based upon baseline subtraction, the time shift is the most problematic. A temperature change as small as 2°C can significantly degrade the performance of baseline subtraction, and even a 1°C change can degrade imaging algorithms [18]. If Lamb waves propagate in a complex structure, multiple reflections, scattering, and reverberations usually occur, and the recorded signals become diffuse-like (very complex). For these signals, individual echoes are no longer identifiable, and the first

order effect of a temperature change is a time dilation or compression [98]. For many plate-like components the situation is somewhere in between the cases of simple, single modes and complex, diffuse-like signals, although signals are probably closer to the diffuse case for structures of realistic geometrical complexity.

Several methods have been proposed to address the temperature variation problem. Lu and Michaels [98] and Konstantinidis *et al.* [99] both used an optimal baseline selection (OBS) method, where a number of baselines were recorded at different temperatures and the optimal baseline that minimized the residual signal was selected. The baseline signal stretch (BSS) method, which was introduced in [98] and since used by others [100, 101], adjusted the optimal baselines to best match the current test signals. The third method combines the OBS and BSS methods and is shown to generally provide the best compensation for temperature variations [16, 98, 99]. However, these methods have limitations for application. It has been observed that the temperature range over which the stretching is effective decreases as signal complexity increases, although this has not been quantified. Signal complexity influences temperature compensation in two ways. The first is echo overlap. If two echoes are partially overlapping and temperature changes in the meantime, the later echo will shift in time more than the earlier echo, causing the interference between them to change. The second is similar but arises from the presence of multiple modes. If two echoes from different modes are wholly or partially overlapped, their coefficients of velocity change with temperature are different, and they will shift differently with temperature. The stretch method also has the undesired effect of slightly shifting the frequency.

2.5.2 Surface Wetting Effects on Lamb Waves

Another common environmental condition is surface wetting, which can occur on one or both sides of plate-like structures and thus affect the propagation of Lamb waves.

The first scenario of surface wetting is often referred to as "liquid loading", where a plate is fully or partially covered with or immersed in a liquid. One main effect of this scenario on Lamb waves is amplitude attenuation because of energy leakage into the liquid [102, 103]. Another effect is the change of dispersion of Lamb waves. Wu and Zhu [104] studied the propagation of Lamb waves in a plate bordered with inviscid liquid layers on both sides and found the velocity of Lamb waves change with the thickness of the water layer. They also investigated the propagation of Lamb waves in a plate bordered with a viscid liquid later and found that phase velocity change is primarily determined by mass or inertial loading [105].

The second scenario of surface wetting is random and distributed wetting (i.e. liquid droplets), which is perhaps the most realistic and problematic. However, this scenario has not been as fully investigated as the first one; the results to date indicate that even small amounts of surface wetting can adversely affect the performance of Lamb wave SHM systems [106, 107].

2.5.3 Load Effects on Lamb Waves

Aside from temperature and surface wetting, the most pervasive environmental change in the life of many structures is loads. For example, an aircraft or a bridge inherently bears varying loads resulting from pre-stress or bending stress during its normal operation. Even if there is no damage, such varying loads can change the sensor-structure interface, specimen dimensions, and wave speeds, all of which cause the ultrasonic signals to change in a complex manner that further affects baseline subtraction results.

Many investigations have focused on acoustoelasticity, which is a non-linear effect describing the stress dependence of acoustic wave velocity in elastic media. The acoustoelastic effects for Lamb waves propagating in plates with uniform and non-uniform stresses was studied by Husson using a perturbation theory [108]. He concluded that

Lamb wave modes were sensitive only to the symmetric part of the stress field in plate. Qu and Liu [109] generated dispersion curves of Lamb waves in a pre-stressed aluminum plate. Rizzo and Lanza di Scalea [110] examined the frequency-dependence of the acoustoelastic sensitivity of guided waves in the case of pre-stressed bars and showed that low values of frequency-diameter product result in larger acoustoelastic sensitivity. Chen and Wilcox [111] investigated the effects of loads on properties of guided waves in plates and rods using the semi-analytical finite element method. They found that the relationship between phase velocity and applied strain became approximately linear when the frequency-dimension was above 1 Hz-m. An and Sohn [112] tested Lamb waves excited by dual-PZT transducers under varying static loading conditions and similar conclusions as [111] were drawn. Song *et al.* [113] considered an analytical model to study Lamb wave propagation in pre-stressed plate structures and proposed a signal difference coefficient to quantify signal variations caused by different prestresses. Gandhi *et al.* [114] characterized the effects of a biaxial stress field on Lamb waves and compared experimental and analytical results for uniaxial loads. They showed that the phase velocity changed linearly with stress and sinusoidally with propagation directions.

The understanding of acoustoelasiticity on Lamb waves can also be used to measure both applied and residual stresses. Pilarski *et al.* [115] investigated using the non zero-order symmetric Lamb wave modes at the first critical angle for stress measurements. Lanza di Scalea *et al.* [116] proposed a method for stress monitoring in seven-wire strands based on guided stress waves. Recently, Fan *et al.* [117] considered the inverse problem of recovering homogenous biaxial applied stresses from measured Lamb wave signals. Their load estimation method was based on the assumption that the Lamb wave acoustoelastic response under a biaxial load can be decomposed into that of two orthogonal uniaxial loads.

2.5.4 Load Effects on Wave-Based Methods for Defect Detection

Besides changing the properties of Lamb waves such as velocity and amplitude, another critical effect of loads is changing the interaction of Lamb waves with defects. In metallic plate structures, fatigue cracks are one of the most common defect types. It is well known that closed cracks are hard to detect with conventional ultrasonic testing methods because ultrasound can propagate through a tightly closed crack [118, 119]. Applied loads can open such cracks and make them easier to detect. Research on load modulation of ultrasound with fatigue cracks can be traced back to the 1970s and has been the subject of a number of investigations. Frandsen *et al.* [118] used acoustic techniques to qualitatively measure the area over which crack closure occurred. Kim *et al.* [120] investigated closed fatigue cracks using surface acoustic waves and suggested that modulation of loading about a low mean static load was able to enhance the detection of small closed cracks. Mi *et al.* [121] used the bulk wave energy transmitted through the region of a fastener hole to dynamically monitor the initiation and growth of fatigue cracks. Connolly and Rokhlin [122] analyzed the backscattered ultrasonic response to fatigue cracking as a function of transit time, fatigue life, and applied load to visualize and identify specific echoes scattered from geometrical features of the specimen and crack. Ohara *et al.* [123] recently introduced a nonlinear ultrasonic imaging method whereby a phased array was used to create linear and subharmonic images. Images obtained at different applied loads were subtracted to better visualize fatigue cracks.

Fastener (bolt) holes with installed, tightened bolts are widely-used in engineering structures to provide a clamping load to enhance structural strength and stability. The mechanical load on the bolted joint; i.e. the applied torque to the bolt, can change the nature and extent of contact between the hole and fastener and also between the two plates. Bao and Giurgiutiu [124] experimentally investigated the effects of bolt load on Lamb wave propagation through a lap joint and found the received signals

changed significantly as the bolt was tightened. Park *et al.* [125] examined changes in Lamb waves propagating through bolted joints to discriminate between a missing bolt and a tightened bolt. Doyle *et al.* [126] measured the phase changes of the S_0 mode Lamb wave signals as a result of differing bolt torque to assess the condition of bolted joints in complex satellite structures.

Other than bolted joints, load can also change the state of other types of interfaces between components in structures. For example, in bonded surfaces, loads can open kissing bonds, or strains may become inhomogeneous if bond quality or thickness varies. In general, surfaces in kissing contact, which allow wave propagation through the interface, may become separated, and the opposite may also happen when separated surfaces come together. Such load-dependent effects on bulk waves have been investigated in [127, 128, 129]. In [127], the conventional pulse-echo P-wave inspection for kissing bonds was shown to be very sensitive to the pressure conditions such that the detection failed under a high pressure. In [128, 129], the degree of reflected and transmitted ultrasound from kissing bonds in aluminum-aluminum interfaces was shown to vary significantly as the loading condition changed. Studies addressing the changes of Lamb wave propagation at kissing bonds affected by load are still limited. In [127], the dispersion of the A_1 mode obtained from both theory and experiments was found to be sensitive to the change of stiffness at kissing bonds and was thus suggested for kissing bond detection. In [130], experimental results showed that the amplitude attenuations of the A_0 and S_0 modes propagating through a solid-solid contact have a strong dependence on the applied load.

2.6 Research Context

From the literature review on Lamb wave SHM, one can see that the *in situ* detection, localization and characterization of damage under environmental condition changes, especially applied load changes, is a subject that needs further investigation. The

sparse array configuration has been considered as a promising tool for *in situ* applications and the corresponding sparse array imaging algorithms have been shown to be able to monitor defects in laboratory environment. Therefore, the main context of this research is to investigate a methodology that leverages effects of applied loads to enable the *in situ* detection, localization, and characterization of damage in metallic plate-like structures using Lamb waves. Both the DAS and MV sparse array imaging methods are tested under varying loads and their performance is evaluated by conducting fatigue tests on aluminum plates with different complex geometries.

The scattering information of Lamb waves from scatterers plays an important role in the performance of MV imaging; as a result, it is beneficial to obtain such information efficiently. The second aspect of this research is to investigate a methodology for estimating scattering patterns using limited sparse array measurements. The estimation results are validated by laser wavefield measurements and the estimation performance are discussed.

CHAPTER III

SCATTERING PATTERN ESTIMATION AND VALIDATION

Knowledge of how guided waves scatter from defects is very useful for detection, localization, and characterization of damage. As described in Section 2.3, one way to describe scattering patterns is with a matrix indexed by incident angle and scattered angle. The scattering matrices of Lamb waves with scatterers, such as through-holes and notches, are typically obtained by either FE modeling [53, 72, 131] or recording wavefield data from multiple interrogation directions [50, 53]. Both approaches present challenges, the first in terms of model validation and computational requirements, and the second in terms of experimental issues in properly acquiring and comparing data obtained before and after introduction of a defect. If a sparse transducer array is used to measure guided wave signals, it essentially samples the corresponding scattering matrix at a finite number of incident and scattered angles. These samples can be further used to estimate the scattering matrix by appropriate interpolation methods. This chapter provides a comprehensive description of the estimation methodology, validates the estimation results by laser wavefield measurements, and discusses estimation performance.

3.1 Estimation Methodology

The proposed method for estimating a scattering matrix from sparse array data includes pre-processing the array data, computing the initial scattering values through baseline subtraction, and performing radial basis function (RBF) interpolation to obtain the complete scattering matrix.

3.1.1 Signal Preprocessing

When Lamb waves propagate in a homogeneous, isotropic plate, material attenuation and wave leakage become insignificant in terms of amplitude reduction, as compared to the other two factors: geometric spreading loss (GSL) and wave packet spreading loss (WPSL). Although narrow-band excitations are frequently used for guided wave SHM to minimize dispersion, WPSL should not be overlooked, especially when the transmitting pulse is short in time and the propagation distance is long. Several compensation algorithms have been proposed to address the dispersion issue in either the frequency or wavenumber domain [132, 133]. Because the purpose of WPSL compensation here is to recover the amplitude of a wave packet rather than its shape, a more straightforward method is applied. First, an accurate dispersion curve for the guided wave mode of interest is calculated from the nominal thickness and material properties. Then, a relation between the packet amplitude and time is obtained by simulating propagation of the excitation pulse using the computed dispersion curve. Finally, this relation (actually, its inverse) is applied to measured signals to scale their amplitudes to "non-dispersive" values.

In addition to the distance-dependent amplitude loss, transducer and bonding variations also affect amplitudes of the received signals. The last step of signal preprocessing is to scale each received signal based upon the amplitude of its direct arrival. Considering all the steps above, the received signal for transducer pair ij is scaled as

$$\tilde{w}_{ij}(t) = \frac{w_{ij}(t)}{A_{ij}} \sqrt{\frac{D_{\text{ref}}}{D_{ij}}} \frac{1}{\text{WPSL}(t)}. \tag{2}$$

Here $w_{ij}(t)$ is the received signal, $\tilde{w}_{ij}(t)$ is the scaled signal, A_{ij} is the amplitude of the direct arrival of the baseline signal, D_{ij} is the distance between transducers i and j, D_{ref} is a reference distance set to 1 m, and $\text{WPSL}(t)$ is the computed wave packet spreading loss function. Note that the same A_{ij} is used to scale both the current

signal of interest and the baseline signal so that they are scaled exactly the same.

3.1.2 Initial Scattering Values

After scaling the received signals, residual signals are calculated by baseline subtraction. Let $u_{ij}(t)$ refer to the residual signal between the current signal of interest, $\tilde{w}_{ij}(t)$, and the baseline, $\tilde{w}_{ij}^{b}(t)$, after scaling,

$$u_{ij}(t) = \tilde{w}_{ij}(t) - \tilde{w}_{ij}^{b}(t). \tag{3}$$

The envelope-detected residual signal, $r_{ij}(t)$, is the magnitude of the complex analytic signal of $u_{ij}(t)$, which is computed as:

$$r_{ij}(t) = \left| u_{ij}(t) + \mathrm{i}\mathcal{H}\left[u_{ij}(t)\right] \right|, \tag{4}$$

where $\mathcal{H}[\cdot]$ denotes the Hilbert transform and $\mathrm{i} = \sqrt{-1}$. The amplitude of the directly scattered wave packet of the envelope-detected signal $r_{ij}(t_{\mathrm{scat}})$ is the scattering amplitude R_{ij} of transducer pair ij, where t_{scat} is the calculated arrival time of the scattered signal based upon the group velocity. To compensate for the different propagation distances of the scattering paths, R_{ij} is then scaled by the product of the square root of the transmitter-scatterer path length, D_{is} , and the scatterer-receiver path length, D_{sj}, to obtain the final scattering values $\alpha(\boldsymbol{\theta})$,

$$\alpha(\boldsymbol{\theta}) = R_{ij}\sqrt{D_{is}D_{sj}}. \tag{5}$$

The angular dependence of the final scattering values $\alpha(\boldsymbol{\theta})$ is determined by the relative locations of the transmitter, scatterer, and receiver.

For an N-element transducer array, the $N_p = N(N-1)/2$ unique transducer pairs result in N_p corresponding scattering values. Since the signal transmitted from transducer i and received by transducer j is essentially identical to that transmitted from transducer j and received by transducer i, another set of N_p scattering values are obtained using signal reciprocity. Additional data points can be obtained if the

scatterer has known geometric symmetry. For example, a straight crack is symmetric about its long axis so that scattering from one side is the same as that from the other side; i.e., there is mirror-image symmetry of the incident and scattered angles.

3.1.3 Radial Basis Function Interpolation

The initial scattering data computed from the sparse array measurements need to be interpolated to form the complete scattering matrix. In general, these data are unstructured, meaning that their angular locations are not on a regular grid. Among available unstructured data interpolation algorithms, the most appropriate choice for the application here is RBF interpolation because the only restriction is that the data must be defined at distinct locations [134]. A RBF is a function that depends only on the radial distance from the origin $f = \phi(r)$, where r is the Euclidean distance. Here, the RBF is translated from the origin to a set of M distinct pairs of incident and scattered angles $\boldsymbol{\theta}_i = [\theta^i_{\text{inc}}, \theta^i_{\text{scat}}]$, $i = 1, 2, \ldots, M$, such that $f_i = \phi(r_i)$, where $r_i = (||\boldsymbol{\theta} - \boldsymbol{\theta}_i||)$ is the L_2 norm of the angle differences. Each angle pair $\boldsymbol{\theta}_i$ has an associated initial scattering value α_i. The complete scattering matrix $S(\boldsymbol{\theta})$ can be interpolated by a weighted sum of these translated radial basis functions,

$$S(\boldsymbol{\theta}) = \sum_{i=1}^{M} \lambda_i \phi(r_i), \tag{6}$$

where λ_i are expansion coefficients determined by ensuring that interpolated values match the given values α_i, $i = 1, 2, \ldots, M$, at the given incident and scattered angles $\boldsymbol{\theta}_i$, $i = 1, 2, \ldots, M$. This requirement leads to the following matrix form:

$$\mathbf{A}\boldsymbol{\lambda} = \boldsymbol{\alpha}, \tag{7}$$

where $\mathbf{A}$ is the interpolation matrix with entries $A_{ij} = \phi(r_{ij} = ||\boldsymbol{\theta}_j - \boldsymbol{\theta}_i||)$, $i = 1, 2, \ldots, M$, $\boldsymbol{\lambda} = [\lambda_1, \lambda_2, \ldots, \lambda_M]^T$ is the expansion coefficient vector, $\boldsymbol{\alpha} = [\alpha_1, \alpha_2, \ldots, \alpha_M]^T$ is the vector containing all initial scattering values, and $[\cdot]^T$ denotes the transpose.

The entries λ_i of the vector $\boldsymbol{\lambda}$ are found by pre-multiplying the vector $\boldsymbol{\alpha}$ by $\mathbf{A}^{-1}$. To obtain a unique solution, the interpolation matrix $\mathbf{A}$ needs to be nonsingular, or invertible, and its singularity is determined by the choice of basis function $\phi(r)$. The sufficient condition for $\phi(r)$ to guarantee a nonsingular $\mathbf{A}$ is that $\phi(r)$ must be completely monotonic; the complete proof can be found in [135]. Basis functions that meet this requirement include Gaussian, multiquadric (MQ), and inverse multiquadric. To explore the efficacy of scattered data interpolation, Franke [136] compared 29 interpolation algorithms on a set of six functions and concluded that the MQ method most often provided the best results of all tested methods. The previous investigation conducted by the authors also suggests that the MQ basis function has satisfactory fitting ability and visual smoothness; hence, this basis function is used here.

The MQ function is of the form $\phi(r) = \sqrt{r^2 + c^2}$ where the parameter c controls the shape of the function. A small c corresponds to a "steep" function while a large c corresponds to a "flat" function. This parameter plays an important role in the accuracy of MQ-RBF interpolation. Prior research has shown that the interpolation tends to become more accurate as c increases [137, 138]. On the other hand, the condition number of the interpolation matrix $\mathbf{A}$ grows if a larger c is selected, which can lead to an unstable matrix inversion [139]. In practice, the shape parameter c is often either picked by application-specific trial-and-error approaches or other (non-optimal) ad-hoc methods [136, 140, 141]. Unfortunately, there is no explicit way to choose an "optimal" c that works universally. Here, an ad-hoc method is used to select the largest possible c that yields a non-negative scattering matrix.

Since the actual scattering matrix is a function of the incident and scattered angles, which are periodic about 360°, the estimated scattering matrix must also be periodic with respect to both angles (i.e., it must be continuous at ±180° in both directions). However, direct RBF interpolation of the initial scattering values does not enforce this periodicity. To prevent this problem, the data points are augmented

prior to interpolation by replicating the initial scattering values by $\pm 360^\circ$ in both directions, resulting in data points in the range of $[-540^\circ, +540^\circ]$. Interpolation is performed on these augmented values, and the final scattering matrix is obtained from the interpolated data in the range of $[-180^\circ, +180^\circ]$ for both angles.

3.2 Experimental Setup

Separate experiments were conducted on two identical 6061-T6 aluminum plates with dimensions of 1219 mm $\times$ 1219 mm $\times$ 3.18 mm. The edges of both plates were covered with duct sealing compound to damp the edge reflections. The first experiment recorded sparse transducer array signals for scattering matrix estimation. The second experiment measured the scattered wave field from a nominally identical scatterer with a laser vibrometer, which provided a much higher angular resolution of measurements than those from the sparse array.

3.2.1 Sparse Array Measurements

As shown in Figure 3, the first plate was instrumented with a circular array of ten lead zirconate titanate (PZT) discs, which are 7 mm in diameter, radially polarized, and have a resonance frequency of 300 kHz. The array radius was 203 mm to ensure that no edge reflections would overlap with direct arrivals; however, small amplitude edge reflections were present even though the edges of the plate were damped. The actual transducer array used to record experimental data consisted of eight transducers as highlighted in the figure, where transducers #1, #3, #5, and #7 were 90° apart from each other and the rest were 30° from their nearest neighbor. This array geometry was designed to capture not only the high amplitude regions of the scattering matrix but also the low amplitude regions.

An NI PXI-5412 waveform generator was programmed to apply a 50-to-500 kHz linear chirp excitation to the transducers, and an NI PXI-2593 multiplexer was used

to switch between the 28 unique transmit-receive pairs. Received signals were digitized by an NI PXI-5122 14-bit digitizer at a sampling frequency of 20 MHz, and 50 waveforms were averaged for each acquisition. These signals were digitally filtered to obtain the equivalent response to a 5-cycle, 100 kHz excitation [35]. The A_0 mode was dominant at this frequency with a wavelength λ of about 16 mm.

An initial set of baseline signals was recorded from the pristine plate. A 5 mm diameter through-hole was then drilled in the center of the plate. Next, a 0.8 mm wide through-thickness notch at an orientation of $-90°$ was hand-cut from the hole with increasing lengths of 1.6 mm ($\lambda/10$), 4 mm ($\lambda/4$), 5.4 mm ($\lambda/3$), 8 mm ($\lambda/2$), 10 mm ($2\lambda/3$), and 14 mm ($\approx \lambda$). The 10 mm notch is shown in the inset of Figure 3. Array data were recorded after the hole was drilled and again after each length increment of the notch.

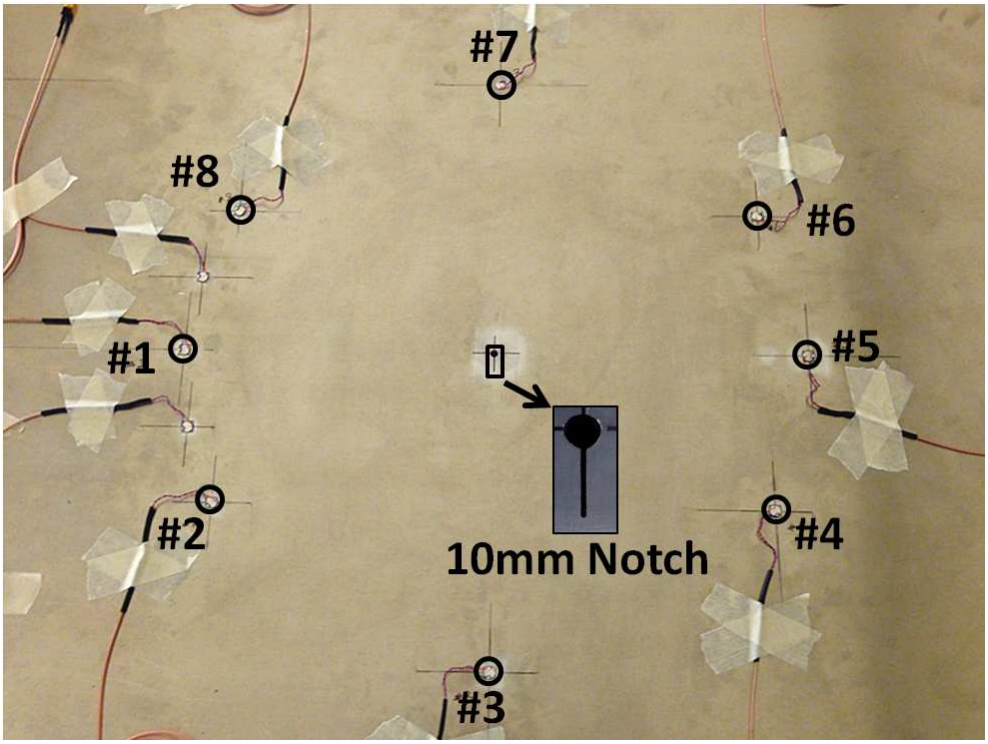

Figure 3: Aluminum plate instrumented with a sparse array of eight PZT transducers for scattering matrix estimation.

3.2.2 Laser Vibrometer Measurements

The laser vibrometer experiment used an identical plate as the sparse array experiment and the same type of piezoelectric transducers for signal excitation. As shown in Figure 4, 13 transducers, which were numbered in counter-clockwise order with the bottom transducer being number one, were glued onto the plate in a semi-circular configuration with a separation of 15°. The radius of the transducer array was 300 mm, which was designed to provide enough space for the laser measurements to be in the far field of the scatterer while minimizing the effect of edge reflections.

The transducers were excited in turn with the same 50-to-500 kHz chirp signal using an Agilent 33250A waveform generator fed through an E&I RF power amplifier. The velocity of the out-of-plane displacement was measured using a Polytec OFC-551 laser fiber vibrometer, which was controlled by a Polytec OFV-5000 vibrometer controller and mounted on an XYZ scanning stage that was programmed via LabVIEW to move in a point-to-point scanning mode. The time traces of measured signals were sampled at 20 MHz, and 64 averages were applied for each acquisition. As done for the sparse array data, a 5-cycle, 100 kHz, tone burst response was obtained through digital filtering.

A nominally identical 5 mm diameter through-hole was drilled in the center of the plate followed by a 0.8 mm wide hand-cut notch at $-90°$ as per the same procedure as the sparse array experiment. The plate remained clamped in the testing position during the hole drilling and notch cutting to minimize re-positioning errors. Full-circle laser scans were performed at a radius of 150 mm and an angular increment of 1° for the cases of no defect, a through-hole, and three different notch lengths, which are 1.6 mm, 5.4 mm, and 10 mm. The 10 mm notch is shown in the inset in Figure 4. The laser measurements from the 10 mm notch are used to validate the scattering matrix estimation results because these data have the best signal-to-noise ratio (SNR).

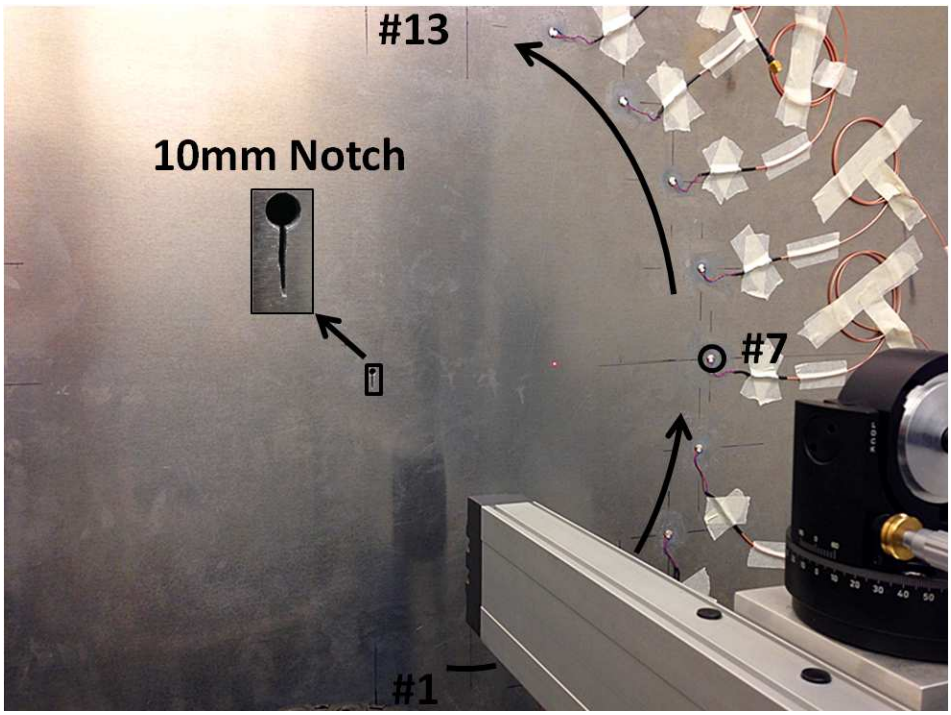

Figure 4: Aluminum plate instrumented with 13 PZT transducers for laser vibrometry measurements to validate estimation results.

3.3 Estimation Results

3.3.1 Signal Preprocessing

Figure 5 shows amplitude vs. propagation distance curves for the 5-cycle, 100 kHz A_0 mode guided wave signals obtained from both laser measurements and simulation. Note that all of the curves are normalized so that the amplitude at a distance of 150 mm is 100%. The gray curve shows the amplitudes of the direct arrivals of the laser measurements from the pristine plate with transducer #7 transmitting. The smaller amplitude outliers are likely caused by the inconsistent surface condition of the plate. The black dashed line is the GSL curve calculated by taking the inverse of the square root of the propagation distance. Clearly it overestimates the measured amplitudes, which indicates the need to also include WPSL. As shown by the black dotted line, the fitting is improved by multiplying the GSL curve by a 5-cycle WPSL curve, which is computed through wave propagation simulation as described in Section 3.1. As shown

by the black solid curve, further improvement in fitting is achieved by multiplying a 4.7-cycle WPSL curve with the GSL curve. Given that the simulation is only approximate, the agreement with the measurements is quite good.

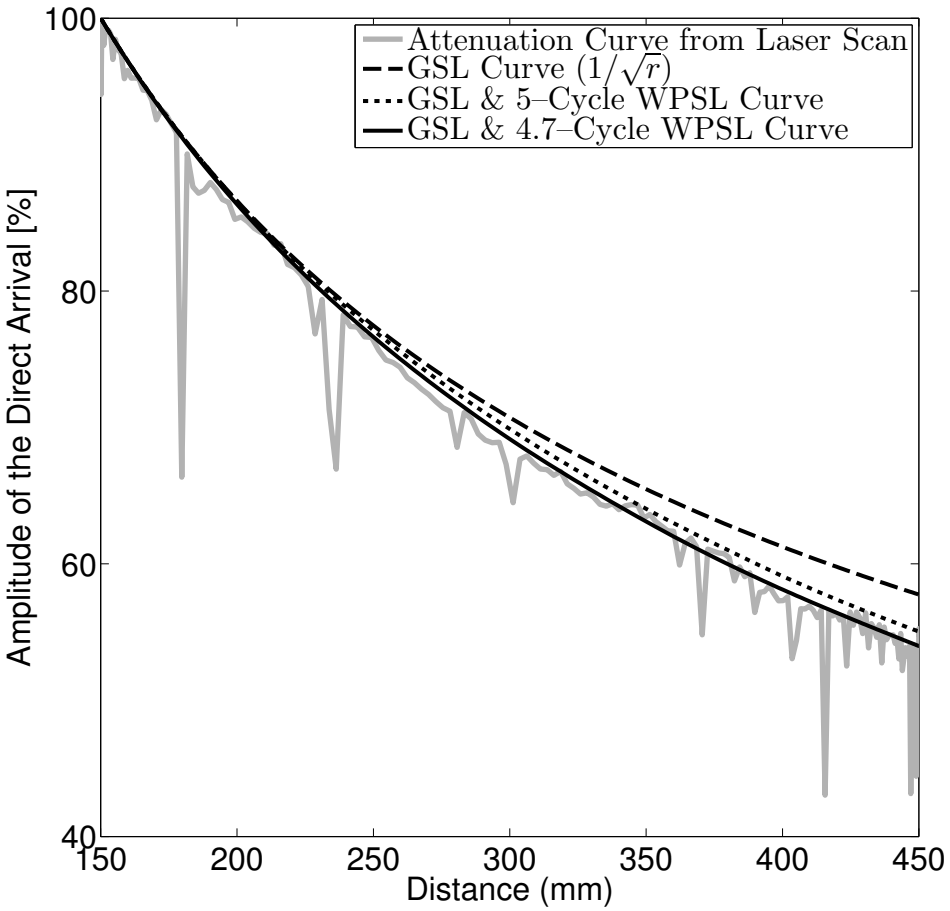

Figure 5: The amplitude versus distance curve for the 5-cycle, 100 kHz, A_0 mode guided wave signals obtained from laser measurements and simulation. The amplitudes at 150 mm were set to 100% for all curves.

The 4.7-cycle WPSL curve was used to preprocess the sparse array signals from the pristine plate (baseline), the plate with a through-hole, and the plate with the hole-plus-notch (all four notch lengths). The A_{ij} values in Eq. (2) were obtained from the baseline data and used to scale all three sets of data. Figure 6(a) shows signals from two transducer pairs after the hole was drilled and before preprocessing; both signals are normalized by the amplitude of the direct arrival of the larger one. Because these two pairs have the same distance between transducers, the normalized amplitudes should be the same; the small differences observed in Figure 6(a) are likely due to transducer and bonding variations. Figure 6(b) shows the same signals after preprocessing, which now have the same direct arrival amplitudes. Also note the amplitudes of later wave packets are larger compared to those in Figure 6(a) as a result of the GSL/WPSL compensation.

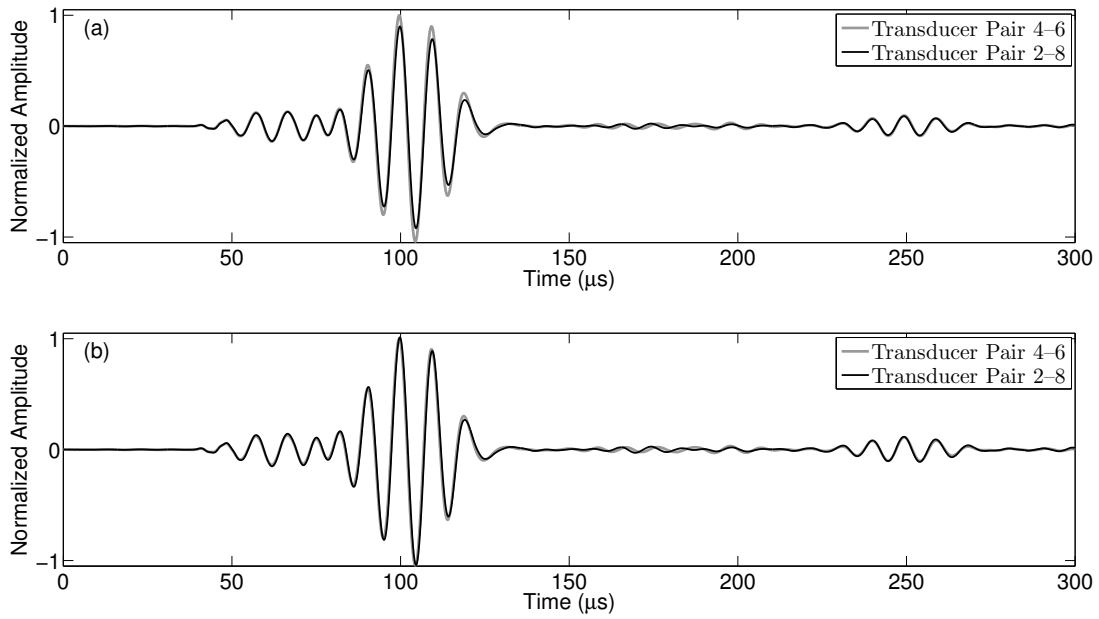

Figure 6: Received signals from two transducer pairs that have the same pair-wise distance. (a) Before preprocessing, and (b) after preprocessing.

3.3.2 Initial Scattering Values

The signals after preprocessing were used to obtain initial scattering values by baseline subtraction. Figure 7(a) shows the hole and the hole-plus-notch signals for the 10 mm notch and transducer pair 1-5; this pair corresponds to the forward-scattering broadside path. Although the first scattered wave arrival overlaps with the direct arrival, the amplitude differences of the wave packet between 150 and 200 μs clearly indicate forward scattering from the notch. The scattering amplitude was extracted from the envelope of the residual signal, which is shown as the black solid line in Figure 7(b). The gray line is the envelope signal of transducer pair 3-7, which corresponds to the forward-scattering end-on path, and the black dashed line is the envelope signal of transducer pair 1-2, which corresponds to the backscattering broadside path. The amplitude differences of the three envelope signals clearly demonstrate the directionality of the scattering from the 10 mm notch.

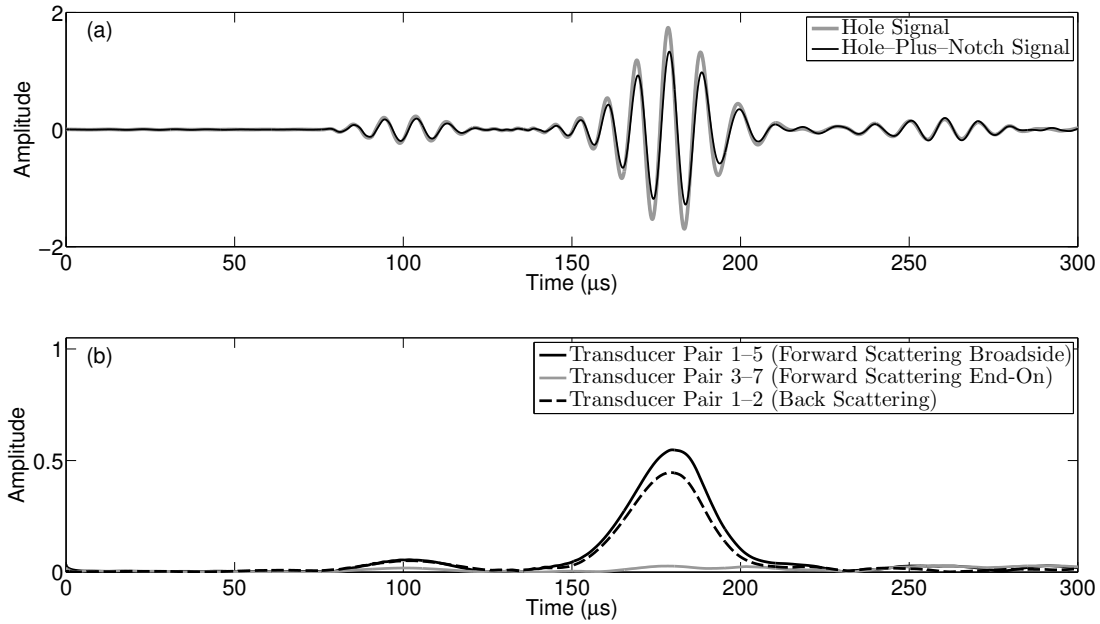

Figure 7: (a) Received signals for transducer pair 1-5 (forward scattering broadside path) from the hole and the hole-plus-notch (10 mm) measurements. (b) The envelope of residual signals for three transducer pairs that show the different scattering amplitudes from the notch.

The initial scattering values from the sparse array measurements were obtained from Eq. (5) and the associated incident and scattered angles were calculated using the mid-point of the notch as the location of the scatterer. Additional scattering values were obtained from transducer reciprocity and the known geometric symmetry of the scatterer; i.e., the combined shape of the hole and the notch. Here, the scatterer is nominally symmetric about the long axis of the notch, meaning that mirror-images of the incident and scattered angles about this axis should have the same scattering values. Because of the symmetry of the sparse array, scattering values obtained from the symmetry of the scatterer are overlapped with those from both the measurements and transducer reciprocity. These overlapped initial scattering values are averaged prior to subsequent analysis.

3.3.3 Estimated Scattering Matrix

The averaged initial scattering values were replicated as described in Section 3.1.3, and MQ-RBF interpolation was applied using a shape parameter of $c = 7$. The final interpolated scattering matrix of the 10 mm notch is shown in Figure 8. This estimated scattering matrix describes the overall scattering behavior in a reasonable manner in which points corresponding to transducer broadside paths have large scattering values while those corresponding to the end-on paths have significantly smaller values. Also, the matrix is clearly continuous on its boundaries (i.e., at $\pm 180^\circ$ in both directions) as a result of using the augmented data for interpolation. The squares in Figure 8 indicate the initial scattering points whose incident and scattered angles are obtained directly from the transducer and notch locations, while the "+" symbols indicate the points obtained from transducer reciprocity. It can be observed that the sparse array samples both high and low amplitude regions of the matrix.

Figure 9 shows the scattering matrices obtained for the three other notch lengths. It can be observed as the notch length increases, the scattering amplitude increases

and the patterns become more directional, which is the expected behavior. When the notch length is small compared to the wavelength (i.e., the 1.6 mm notch case shown in Figure 9(a)), the backscattering is much weaker than the forward scattering. As the notch becomes larger, the backscattering amplitude increases until it is almost equal to the forward scattering amplitude, which can be seen in Figures 9(b), 9(c), and 9(d).

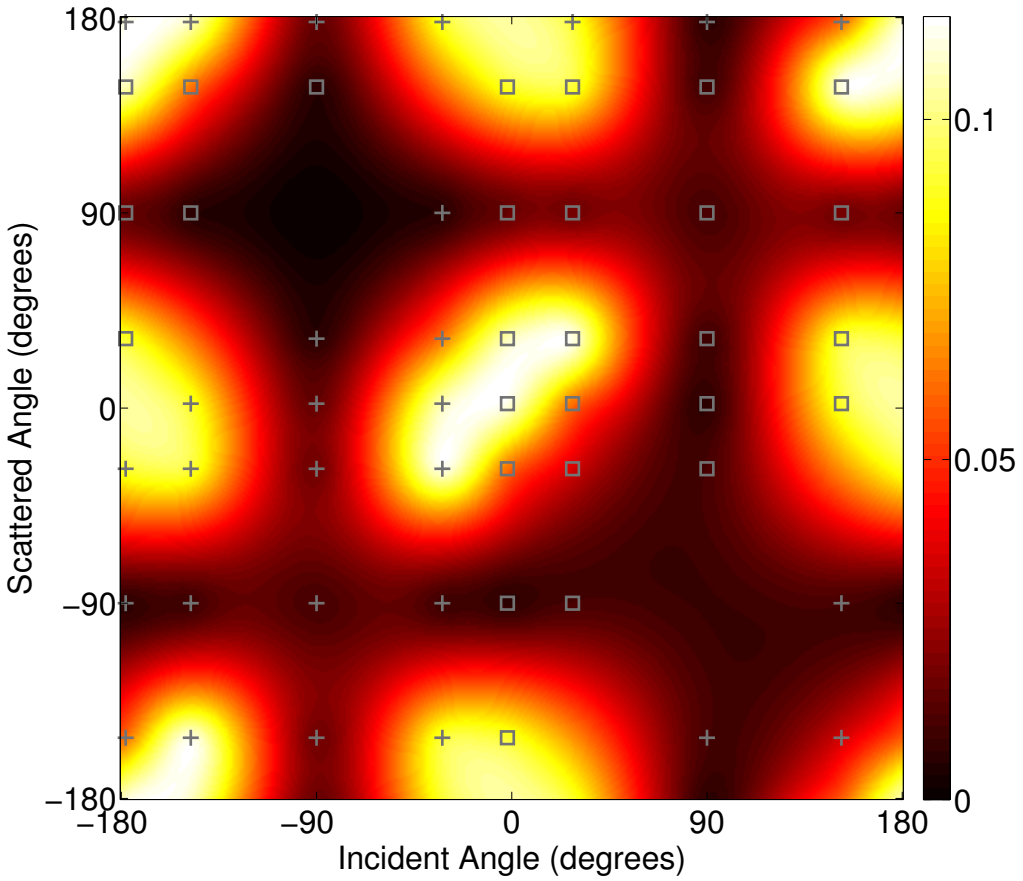

Figure 8: The estimated scattering matrix of a 10 mm notch originating from a 5 mm diameter through-hole at an orientation of $-90°$ for the 100 kHz, 5 cycle A_0 mode obtained from multiquadric RBF interpolation with a shape parameter $c = 7$. The squares highlight the initial scattering values calculated directly using the transducer and notch locations, while the "+" symbols highlight those obtained from transducer reciprocity.

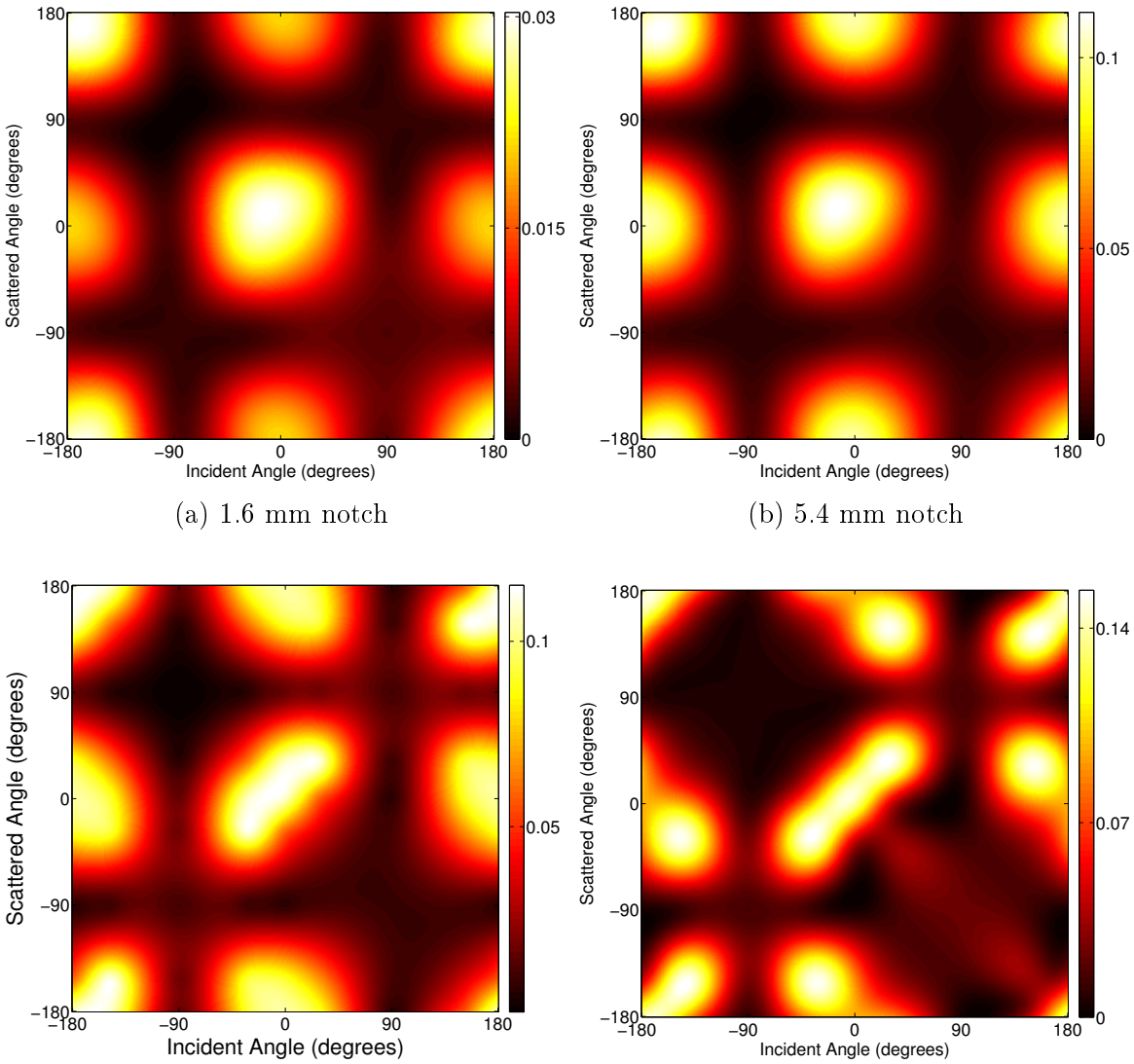

(a) 1.6 mm notch

(b) 5.4 mm notch

(c) 10 mm notch

(d) 14 mm notch

Figure 9: The estimated scattering matrices of a notch of different lengths originating from a 5 mm diameter through-hole at an orientation of $-90°$ for the 100 kHz, 5 cycle A_0 mode. (a) 1.6 mm with $c = 35$. (b) 5.4 mm with $c = 27$. (c) 10 mm with $c = 7$. (d) 14 mm with $c = 39$.

3.4 Validation by Laser Measurements

As described in Section 3.2.2, the laser vibrometer recorded guided wave signals scattered from the hole and the hole-plus-notch (10 mm). As was the case for the sparse array data, transducer and bonding variations can also cause amplitude variations in the laser measurements. Figure 10 shows the amplitudes of the direct arrivals for all 13 laser measurements of the hole, where all curves are rotated such that 0° corresponds to the direction of propagation from the transmitting transducer to the hole; the mean of all the curves is plotted as the thick black line. The middle part of each curve corresponds to the forward scattering path, where the direct arrival interferes with the scattered signal from the hole, causing amplitude fluctuations. All of the measurements demonstrate the same basic scattering pattern but with outliers and overall amplitude variations. To compensate for the overall amplitude variations, laser measurements from each transmitter were scaled to the mean via least-squares minimization. The same scaling coefficients were also used to compensate the hole-plus-notch signals.

The procedures described in Sections 3.1.1 and 3.1.2 were then applied to the laser measurements, which included using the same 4.7-cycle WPSL compensation, obtaining scattering values from the envelope of residual signals, and applying the scattering distance compensation. To compare the estimated scattering matrix with the laser-measured scattered patterns, additional normalizations were applied to scale both sets of data to the range [0, 1], which was necessary because of differences in excitation voltages and receiver responses. As was shown in Figures 5 and 10, inconsistent surface conditions can generate variations in the laser measurements that lead to obvious outliers in the scattering values. These outliers were identified, and the laser-measured scattering values were normalized to their non-outlier maximum value. For the array measurements, the corresponding scattering values, which are indexed by the same 13 incident angles as the laser measurements, were extracted as

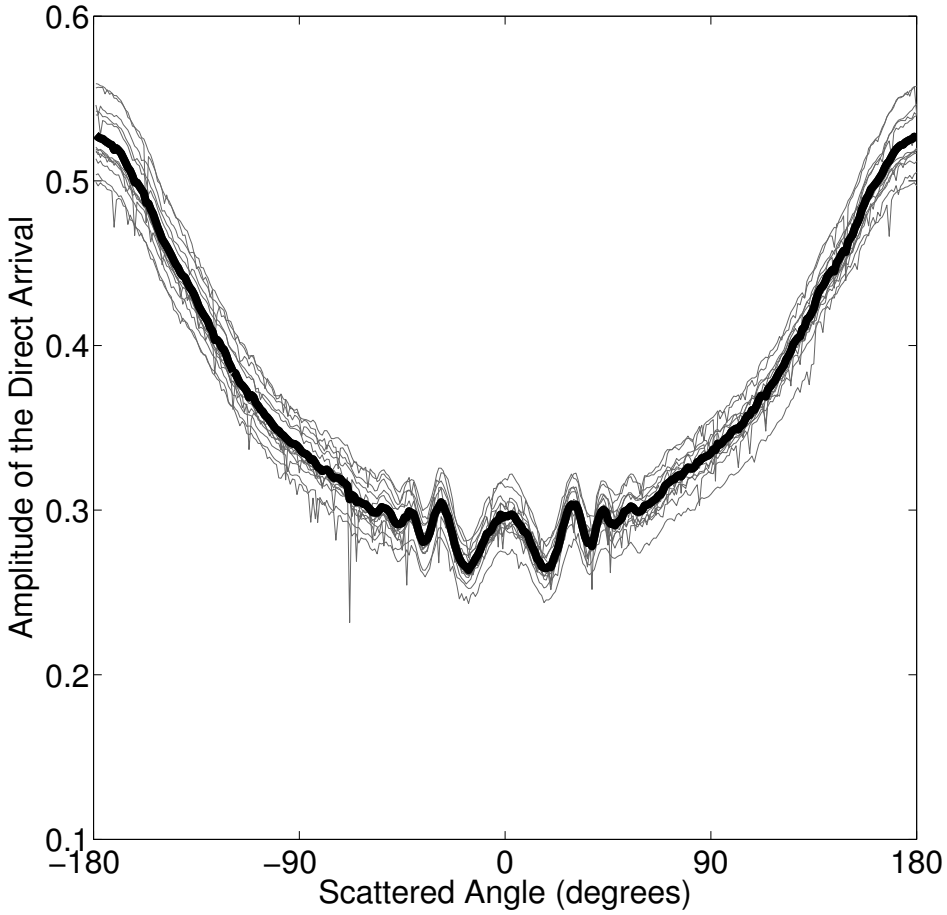

Figure 10: Direct arrival amplitude versus scattered angle from all 13 laser measurements of the through-hole. All curves are rotated such that 0° is the direction of propagation of the incident wave, and their mean is plotted as the thick black line.

columns of the estimated scattering matrix and normalized by the maximum of these exacted values.

Figure 11 shows nine of the thirteen normalized scattering patterns of the 10 mm notch as polar plots, where the directions of the incident waves are indicated by black arrows. The laser-measured scattering patterns are shown by the "+" symbols, and those obtained from the sparse array by solid lines. Not surprisingly, the laser-measured patterns show more structure and detail than the ones generated from the sparse array data. For Figures 11(d), 11(e) and 11(f), where the incident waves are broadside or near broadside to the notch, the scattering patterns are relatively simple

and those from the sparse array data agree well with the laser-measured patterns. When the incident angles are $\pm 90°$, as shown in Figures 11(a) and 11(i), the overall scattering amplitudes are small and the forward scattering laser measurements are very noisy because of the overlap of the scattered signals with the much stronger direct arrivals. The patterns generated from sparse array data still provide a reasonable approximation to the laser-measured ones. The marked difference in scattering patterns between Figures 11(a) and 11(i) for both methods clearly indicates that the scattering is not symmetric as it would be for a notch alone. The worst agreement between the sparse array and laser-measured scattering patterns is exhibited in Figures 11(b), 11(c), 11(g), and 11(h). At these incident angles, which are not present in the sparse array, the lobe structure shown in the laser measred patterns is not accurately captured by the sparse array. Although not shown here, the scattering patterns of waves incident at $\pm 165°$ (close to broadside) are very similar to that of the broadside direction (180°) but somewhat reduced in amplitude. The scattering patterns of waves incident at $\pm 105°$ (close to the end-on direction) are similar to those of waves incident at $\pm 120°$, but with about half the amplitude. All-in-all, the scattering patterns generated from the sparse array data are a reasonable representation of the laser-measured ones, particularly considering the limited number of raw data points (28 for the 8-transducer array) used to construct the patterns.

3.5 Discussion on Estimation Errors

Measurement of scattering is in general challenging, but presents an even greater challenge when the scattering is incremental; that is, when the scatterer of interest is an addition to an existing geometrical feature rather than being a standalone scatterer. Such a situation is the case here for the addition of a notch to an existing hole, which is motivated by the initiation of a crack from a fastener hole. For every measurement point, there is an existing scattered signal from the hole, and baseline subtraction

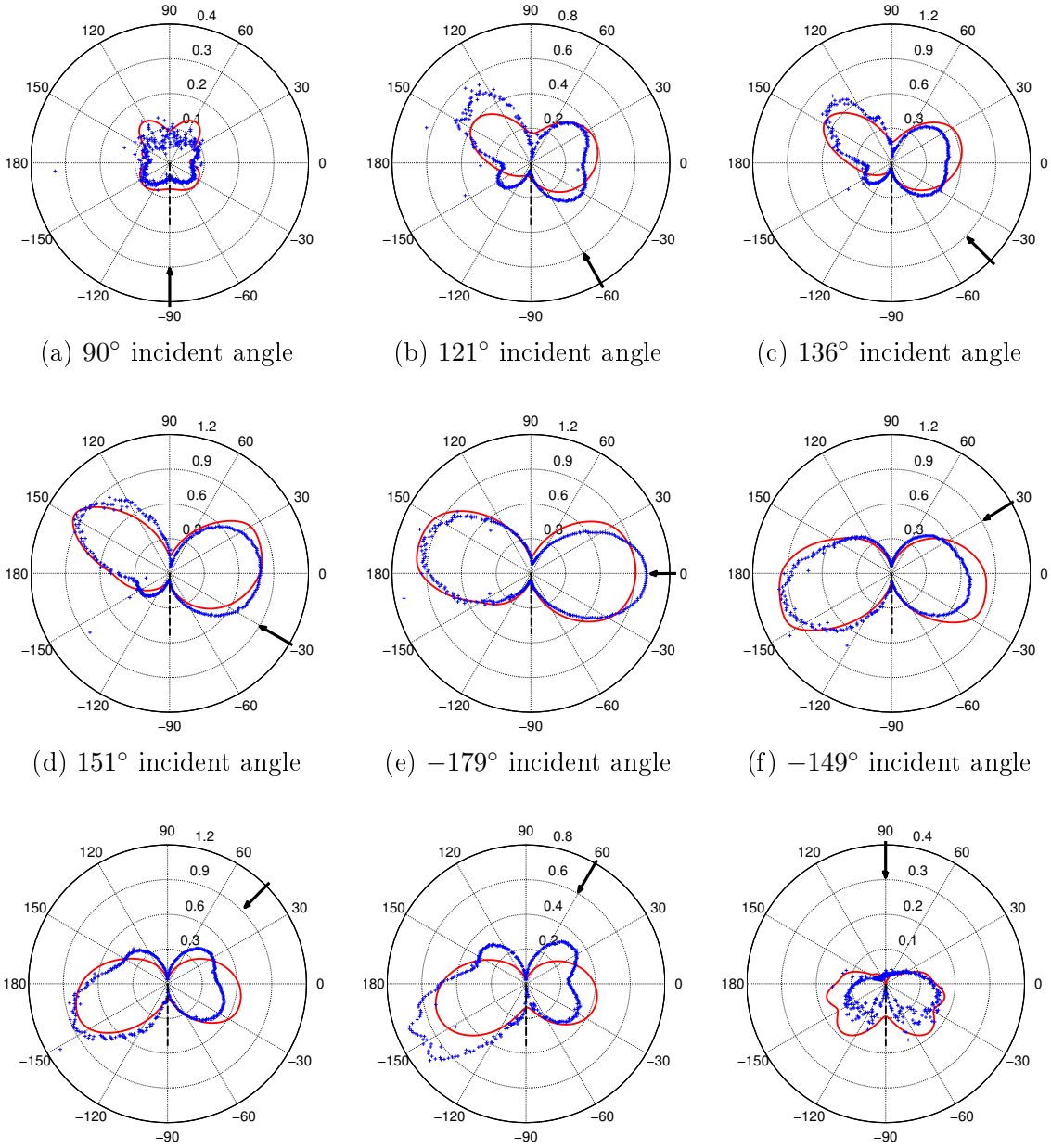

(a) 90° incident angle (b) 121° incident angle (c) 136° incident angle

(d) 151° incident angle (e) −179° incident angle (f) −149° incident angle

(g) −134° incident angle (h) −119° incident angle (i) −90° incident angle

Figure 11: Polar plots for a 5-cycle, 100 kHz, A_0 mode wave scattered from a 10 mm notch originating from a 5 mm diameter through-hole at an orientation of −90°. Incident directions are shown with a black arrow and are (a) 90°, (b) 121°, (c) 136°, (d) 151°, (e) −179°, (f) −149°, (g) −134°, (h) −119°, and (i) −90°. Laser measurements are shown by the "+" symbols, and the solid lines correspond to curves extracted from the estimated scattering matrix.

yields the incremental scattering from the notch. At angular positions corresponding to forward scattering, there is the additional complication of the presence of the interfering direct arrival, which is also problematic for a standalone scatterer.

Although not investigated here, interference patterns between the original and incremental scatterers are expected to give rise to a more complicated dependence on frequency than a simple standalone scatterer, as was also noted in [63]. Differenced signals at all locations are thus very sensitive to any unexpected phase shifts between the signals prior to subtraction such as may be caused by temperature or spatial misalignment (for the laser data). The measurements here were based upon a 5-cycle tone burst excitation, which is an additional source of estimation error due to the frequency dependence of the scattering. More cycles would result in a narrower bandwidth, which is desirable for frequency purity as well as for causing less dispersion; in fact, WPSL can be neglected for the array geometry considered here if more than seven cycles are used. However, because of the relatively short propagation distances for both experiments, five cycles were selected to maintain separation in time of the desired scattered signals.

The primary factor affecting estimation of the scattering matrix from the sparse array data is due to the paucity of points, which is unavoidable with a sparse array. The performance of RBF interpolation, which mainly depends upon the filling distance and shape parameter, is also a factor. The filling distance h, which indicates how well the initial data points fill out the interpolation domain, is usually defined as the maximum nearest-neighbor distance for all of the points. It has been shown that the error convergence rate for MQ-RBF interpolation is $O(h^k)$ as $h \to 0$ and with k being arbitrary large; i.e., a smaller h tends to generate a more accurate result [142, 143]. For this application, h is controlled by the design of the sparse array and the scatterer locations. Although a symmetric array geometry was used here, the performance of the estimation methodology is not likely to be severely affected by a

non-symmetric array based on the author's work.

The lack of pulse-echo data, which corresponds to the directly backscatterered signals, not only increases the filling distance but can cause regions of the scattering matrix to be poorly estimated. This lack of data is particularly important for broadside incidence where the backscattering is large. In this research, by placing transducers 30° away from the broadside path, fairly good estimates of backscattering were obtained, but results would undoubtedly be improved if pulse-echo data were available.

As mentioned in Section 3.1.3, the shape parameter affects interpolation accuracy. Similar to the findings in [137, 138], a larger c was observed to improve the interpolation accuracy. As an example, polar plots of the scattered field from the 10 mm notch for two incident angles are shown in Figure 12. The dotted, solid, and dashed lines are the results extracted from estimated scattering matrices using shape parameters of 1, 7, and 40, respectively. In terms of the overall profile, the dashed line matches the best with the laser measured results shown by the "+" symbols, particularly for the forward scattering lobes; however, there are negative values near 90° for the dashed pattern ($c = 40$) of Figure 12(b), which is physically impossible. Therefore, the criterion used here is to choose the maximum possible c under the constraint that all the scattering values be positive. The upper bound of c is the value that forces the inverse of the condition number of the matrix to be smaller than the machine precision, which is not a factor here. Based on this criterion and restricting c to integer values, it was selected as 35, 27, 7, and 39 for notch lengths of 1.6 mm, 5.4 mm, 10 mm, and 14 mm, respectively.

Other factors that may also affect the estimation results include possible small differences in notch orientation between the two separate experiments, and determining the exact location along the notch to calculate incident and scattered angles for each transducer pair. However, they are minor compared to the other issues discussed.

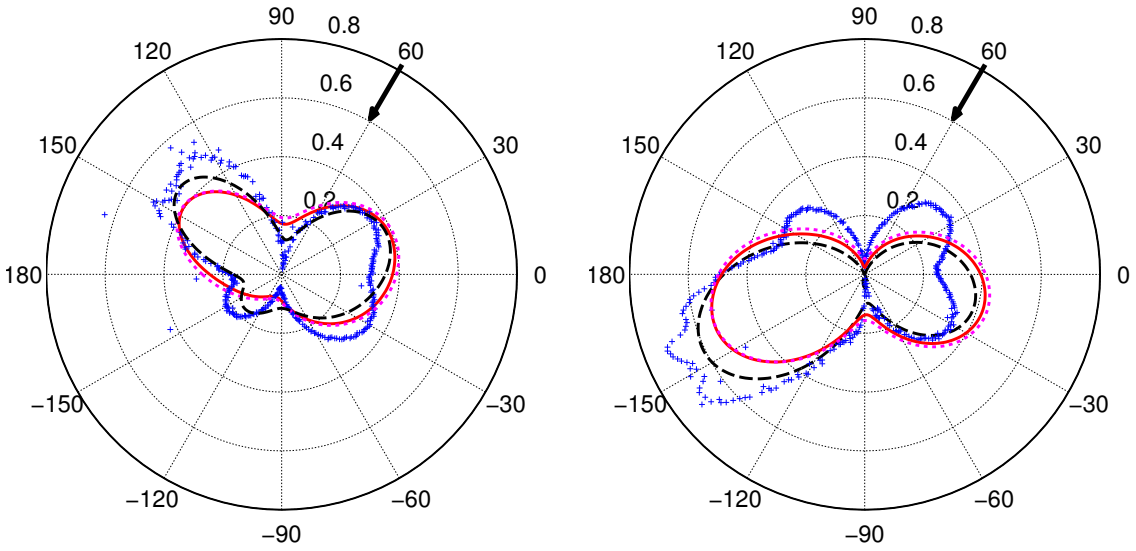

(a) 121° incident angle

(b) −119° incident angle

Figure 12: Polar plots of scattering patterns showing the effect of varying the RBF shape parameter on interpolation performance. Laser measurements are shown by the "+" symbols, and curves extracted from the estimated scattering matrices are shown as the dotted lines ($c = 1$), the solid lines ($c = 7$), and the dashed lines ($c = 40$). Waves are incident from (a) 121° and (b) −119°.

3.6 Summary

This chapter has presented an effective approach for estimating Lamb wave scattering patterns using measurements from a sparse transducer array. The array signals were preprocessed to compensate for the geometric spreading loss, dispersion loss and transducer and bonding variations. The initial scattering values were then extracted from the amplitudes of scattered wave packets and the MQ-RBF interpolation method was performed to obtain the complete scattering matrix. The estimation results for a notch originating from a through-hole were compared to laser measurements by generating multiple polar plots for a range of incident angles. It was observed that the estimation results agreed reasonably well with the laser measurements, particularly considering the limited amount of data available from the sparse array. Factors influencing the estimation error such as the bandwidth of the excitation signal, parameters

used in the MQ-RBF interpolation, and the array design were discussed.

The main contributions of this chapter include proposing and validating a methodology to obtain scattering patterns from an in situ sparse array, providing estimated scattering matrices for notches of different lengths emanating from a through-hole for the A_0 Lamb wave mode, and presenting high angular resolution scattering patterns for one notch as obtained from laser measurements. The demonstrated scattering matrix estimation methodology has the potential to be used as part of a variety of SHM methods based upon sparse arrays where the inherent lack of detail resulting from the small number of measurements can be well-tolerated.

CHAPTER IV

APPLICATIONS OF THE SCATTERING PATTERN ESTIMATION METHODOLOGY

The estimation method introduced previously provides a reasonable quantification of Lamb wave scattering. One of its applications to SHM is to characterize a defect by directly evaluating the estimated scattering patterns. In [55], an experimentally measured bulk wave scattering matrix was used to determine the shape, orientation, and length of a 2-D crack-like defect. Similarly, the approximate length and orientation of an unknown notch emanating from a hole could be obtained by comparing the amplitude and directionality of its estimated scattering matrix to the calibrated ones, such as those shown in Figure 9. In addition to the straightforward application, the scattering pattern estimation method can also be used for a variety of other SHM techniques based upon sparse arrays. This chapter describes two applications: the first uses estimated scattering patterns to aid in the design of sparse array geometries and the second incorporates estimated scattering patterns with sparse array imaging algorithms for improved defect characterization.

4.1 Sparse Array Design Based upon Scattering Pattern Estimation

The sparse or spatially distributed transducer array offers a cost-effective solution for rapid interrogation; therefore it is promising for widespread deployment. Because the spatially distributed array uses a limited number of sensors, the design of such an array is critical for its performance. Croxford *et al.* [45] used the scattering matrices of holes and notches to calculate the worst-case SNR of different array configurations. The worst SNR resulted from the geometry for which multiple transducer pair paths

were at or near nulls in the scattering matrix. Fromme [44] studied the scattering of the A_0 Lamb wave mode by directional defects through wavefield scanning and finite element simulations and recommended that scattering information should be taken into account when designing transducer arrays.

In this section, the scattering estimation methodology is used to evaluate the performance of a specific guided wave transducer array in terms of its ability to capture scattering information for a specific defect and incident wave type. Simulation results of the performance of different array designs are presented.

4.1.1 Scattering Pattern Approach to Array Design and Analysis

Scattering pattern estimation consists of two steps: (1) obtaining initial scattering values, and (2) interpolating them to estimate the scattering matrix. The initial scattering values can be obtained by two approaches. The first approach uses experimental measurements from a specific transducer array as per the description in Chapter 3. Another approach, which is introduced here, re-samples a known scattering matrix of a specific defect based upon an assumed transducer array configuration. For each transducer pair of the assumed transducer array, a scattering value is sampled from the known scattering matrix indexed by its computed incident and scattered angles. Figure 13(a) shows an example of the incident and scattered angles associate with one transducer pair; i.e., transducer pair 1-2 . The corresponding sampled scattering amplitude is indicated by the "+" sign in Figure 13(b), which shows the scattering matrix of the A_0 mode for a 10 mm horizontal notch obtained from FEM[1]. For an N-element array, the $N(N-1)$ transducer pairs result in $N(N-1)$ corresponding scattering amplitudes. By varying the assumed array configuration, this approach can be used to evaluate the ability of such an array to capture the scattering information of a specific defect and furthermore provide guidance for array design.

[1]FEM data provided by Prof. Paul Fromme of University College London.

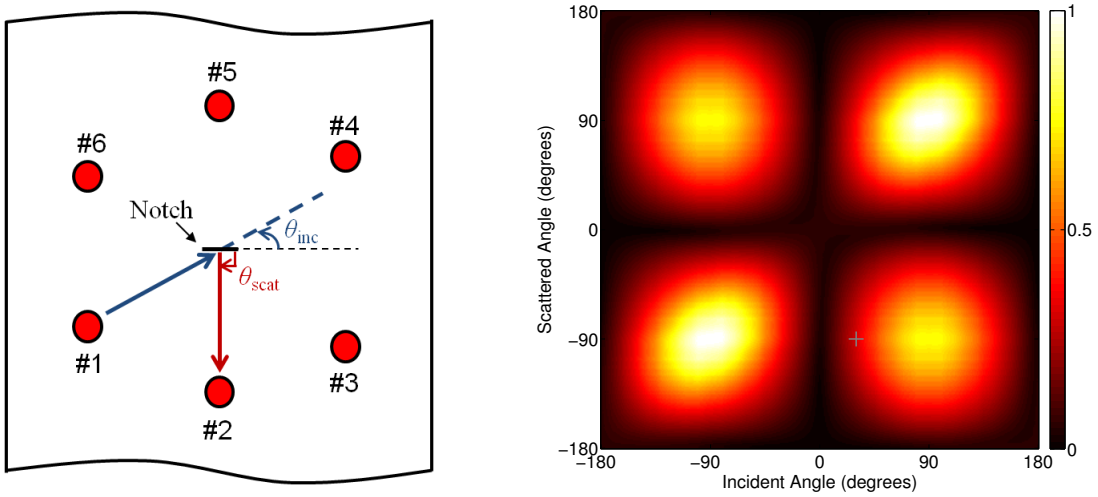

(a) Incident and scattered angles associated with a transducer pair

(b) FEM results of the scattering matrix of the A_0 mode for a 10 mm horizontal notch

Figure 13: (a) Example showing the incident and scattered angles associated with transducer pair 1-2. (b) The scattering matrix of the 100kHz, A_0 mode for a 10mm horizontal notch obtained from FEM. The "+" sign shows the sampled scattering amplitude associate with the transducer pair.

After the initial scattering values are obtained from an assumed array configuration, MQRBF interpolation is used to estimate the full 2D scattering matrix. The estimation result is compared to the known matrix by computing the root mean square (RMS) error defined as:

$$\sqrt{\frac{1}{P}\sum_{j=1}^{P}\left[\tilde{S}\left(\boldsymbol{\theta}_j\right)-S\left(\boldsymbol{\theta}_j\right)\right]^2}, \tag{8}$$

where P is the number of points being used to the compute error and $\boldsymbol{\theta}_j, j = 1, \ldots, P$ are those points. In this case, the RMS error was computed using all points in the scattering matrix, i.e., $P = 130,321$ (calculated for 361×361). $\tilde{S}\left(\boldsymbol{\theta}_j\right)$ is the interpolated scattering matrix based upon samples using one specific array configuration and $S\left(\boldsymbol{\theta}_j\right)$ is the known matrix obtained from FEM. As discussed in Chapter 3, the shape parameter c plays a critical role on RBF interpolation accuracy. An exhaustive search of the c ranging from 0 to the value decided by the ad-hoc criterion proposed in Chapter 3 is used here to obtain the minimum RMS error for each array configuration.

4.1.2 Analysis of Typical Array Configurations

Three six-transducer arrays with typical configurations are analyzed and their estimated scattering matrices are compared to the known matrix by the RMS error of Eq. 8. All of the arrays are assumed to work with the pitch-catch method as they commonly do in the majority of sparse array SHM systems.

As Figure 14(a) shows, the first array has evenly distributed transducers in angle and one transducer pair placed broadside to the defect orientation. The initial scattering data shown in Figure 14(b) indicate that such an array samples the scattering matrix evenly except for the back-scattering regions due to the lack of pulse-echo data. It also shows that this array captures the strong forward scattering well by having a transducer pair at the broadside of the notch but does poorly at capturing the weak scattering in line with the notch orientation. These observations are further confirmed by its corresponding estimated scattering matrix shown in Figure 14(d). The matrix was obtained using the optimal shape parameter c of 160 that generates the minimum RMS error of 0.0514. Figure 14(c) shows that the RMS error as a functon of c ranging within [0,360], where 360 is the maximum angualr span of a scattering matrix. For the range of c considered here, all values generate a non-negative scattering matrix.

The second array, which is shown in Figure 15(a), has evenly distributed transducers in angle as well but one transducer pair placed in line with the defect orientation. The initial scattering data shown in Figure 15(b) indicates that this array captures the weak scattering well but does poorly with the strong scattering. Its RMS error curve is shown in Figure 15(c), where the minimum error (0.0628) occurs when using a shape parameter c of 90. However, any $c > 4$ generates negative scattering matrices; therefore, the practical c for this array configuration is selected to be 4. The corresponding estimated scattering matrix is shown in Figure 15(e) with a RMS error of 0.1081.

The last array shown in Figure 16(a) has more broadside transducer pairs. Intuitively, it might be considered to be a better design given that the orientation of the defect is known. However, as shown in Figure 16(c), the overall level of the RMS error is large with the minimum value being 0.1155, which is the largest of all three arrays. As Figures 16(b) and 16(d) indicate, this array mostly captured the stronger amplitude part of the scattering pattern, but it failed to capture any weak scattering.

4.1.3 Monte Carlo Simulation Results

A Monte Carlo simulation was performed to randomly vary the array configuration in terms of the angular locations of the transducers relative to the scatterer with the goal of obtaining some general insights about array design. The simulation was performed using a six-element circular array with a radius of 100 mm interrogating a 10 mm horizontal notch. The angles between the six transducers and the scatterer were drawn from a uniform distribution in the interval of $[180°, +180°)$; configurations with transducers too close together were discarded. The known scattering matrix was resampled as per the array configuration; the samples were interpolated and the estimated scattering matrix was compared to the known matrix using the RMS error. The total number of trials performed was 10,000.

Figure 17 shows three good array configurations obtained from simulation. The value of RMS error is 0.0456 for array #4, 0.0450 for array #5, and 0.0424 for array #6. From the analysis of the three typical array configurations and the results of the Monte Carlo simulation, a good array design is shown to capture both strong and weak scattering information. For a transducer array working in strictly pitch-catch mode, it is not possible to obtain the directly backscattered information from the array measurements (i.e., the pulse-echo data). However, capturing both of the forward and backscattered regions is still possible by placing transducer pairs relatively close together, which is another factor that was observed from the good array design.

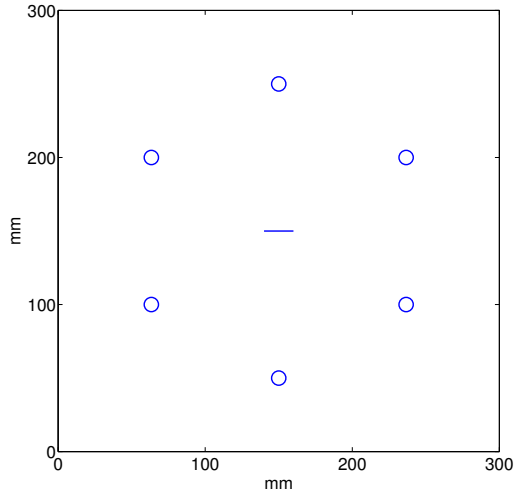

(a) Array configuration #1

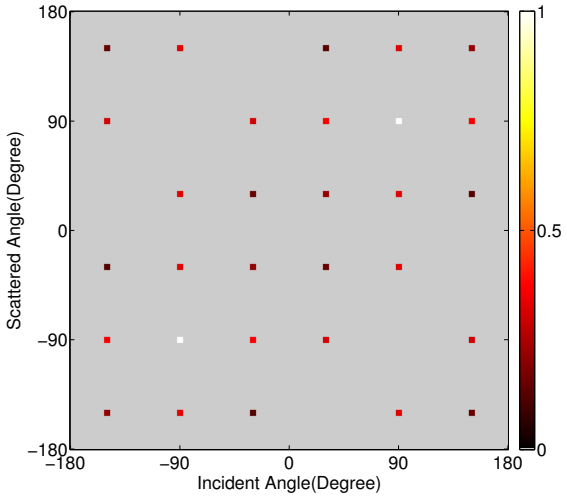

(b) Initial scattering data samples

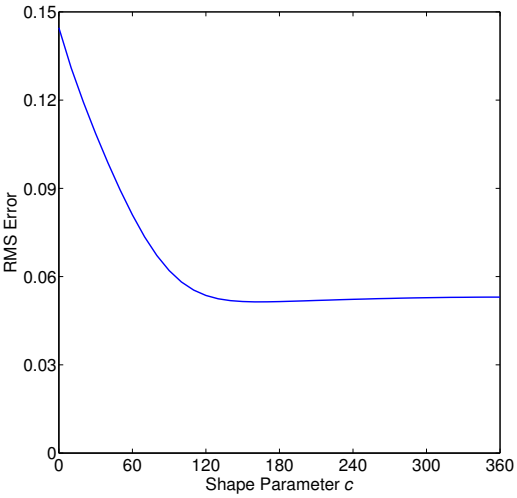

(c) RMS error

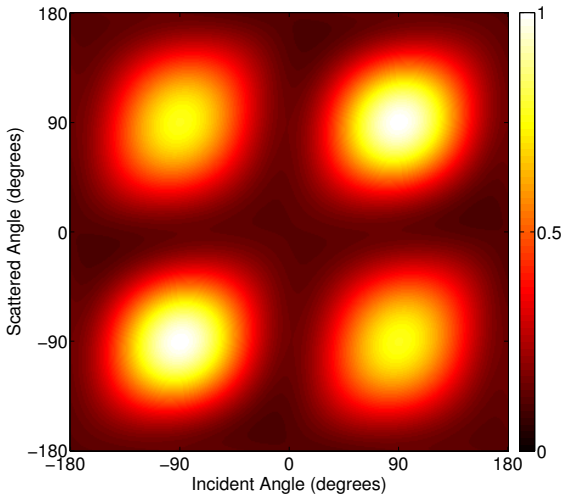

(d) Estimated scattering matrix ($c = 160$)

Figure 14: Analysis of the typical array configuration #1. (a) Array configuration. (b) Initial scattering data samples. (c) RMS error of the estimation as a function of the shape parameter. (d) The final estimated scattering matrix with $c = 160$.

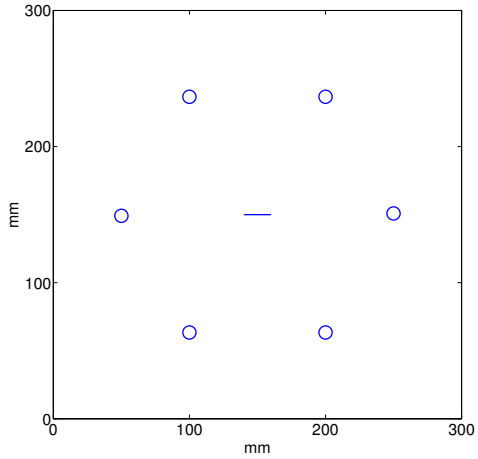

(a) Array configuration #2

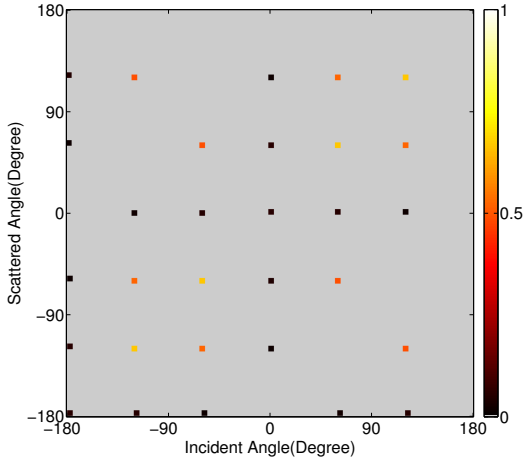

(b) Initial scattering data samples

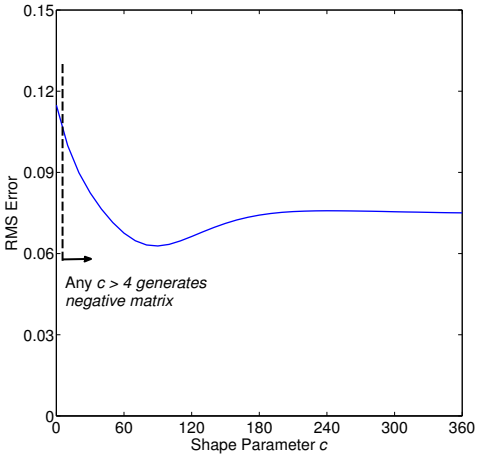

(c) RMS error

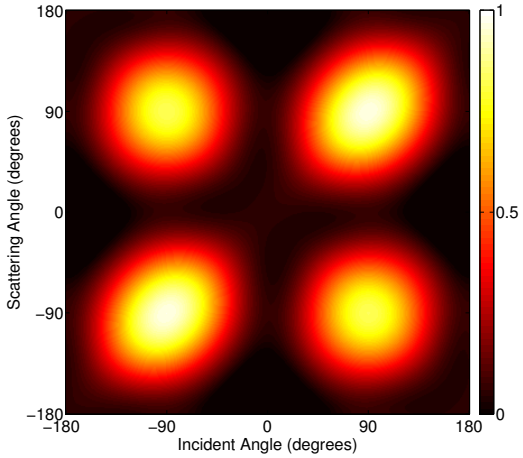

(d) Estimated scattering matrix ($c = 90$)

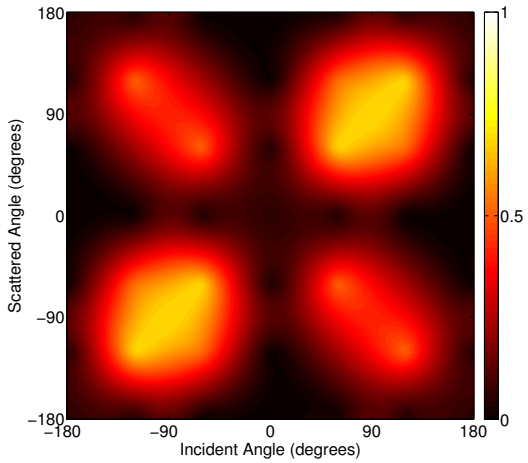

(e) Estimated scattering matrix ($c = 4$)

Figure 15: Analysis of the typical array configuration #2. (a) Array configuration. (b) Initial scattering data samples. (c) RMS error of the estimation as a function of the shape parameter. (d) The final estimated scattering matrix with $c = 90$. (e) The final estimated scattering matrix with $c = 4$.

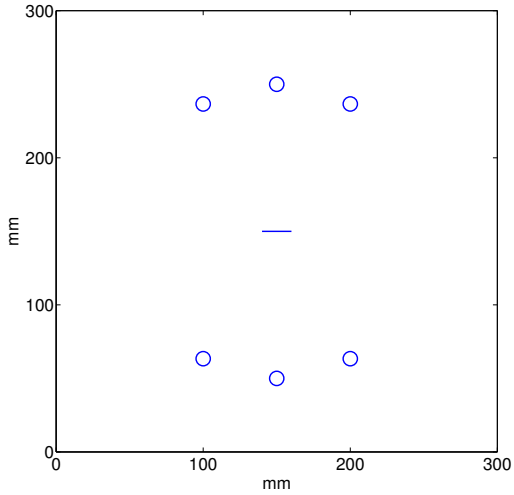

(a) Array configuration #3

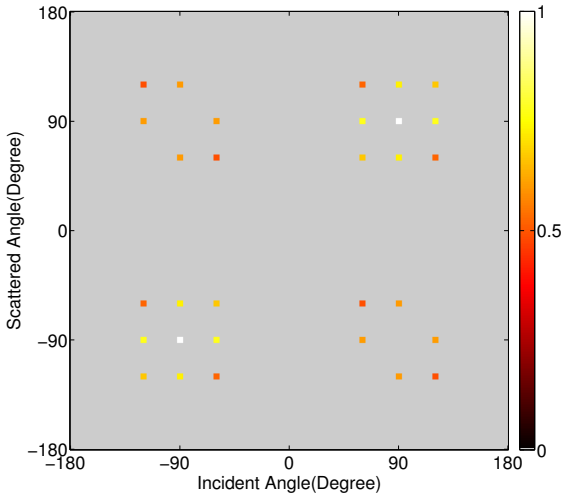

(b) Initial scattering data samples

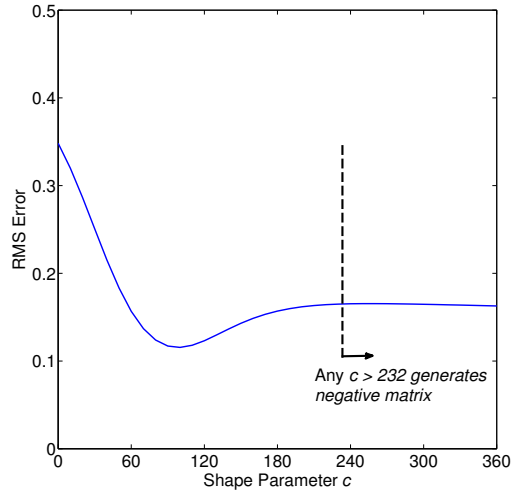

(c) RMS error

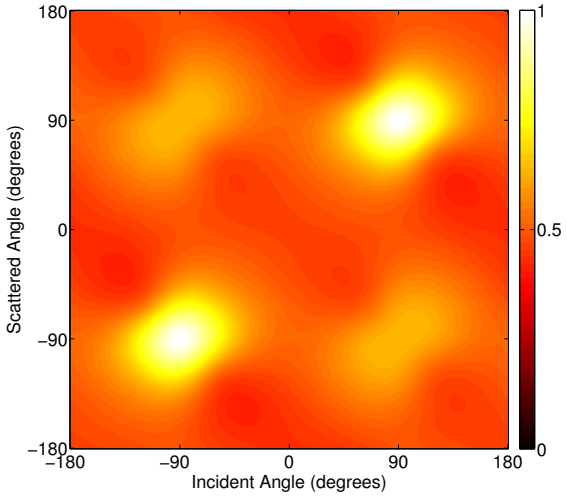

(d) Estimated scattering matrix ($c = 100$)

Figure 16: Analysis of the typical array configuration #3. (a) Array configuration. (b) Initial scattering data samples. (c) RMS error of the estimation as a function of the shape parameter. (d) The final estimated scattering matrix with $c = 100$.

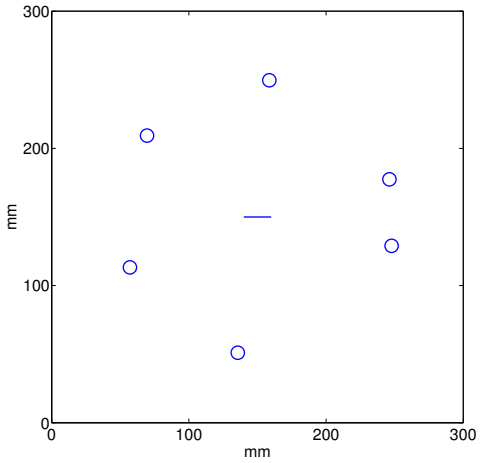

(a) Array configuration #4

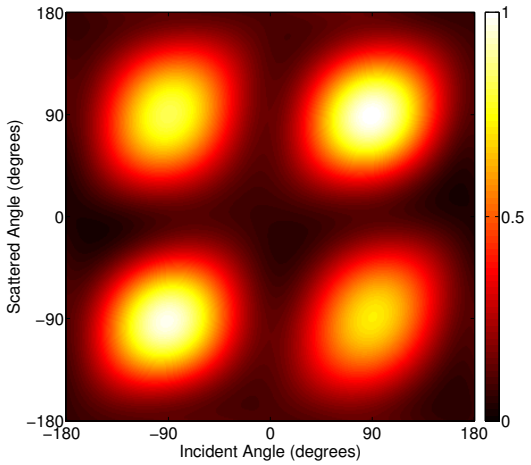

(b) Estimated scattering matrix #4

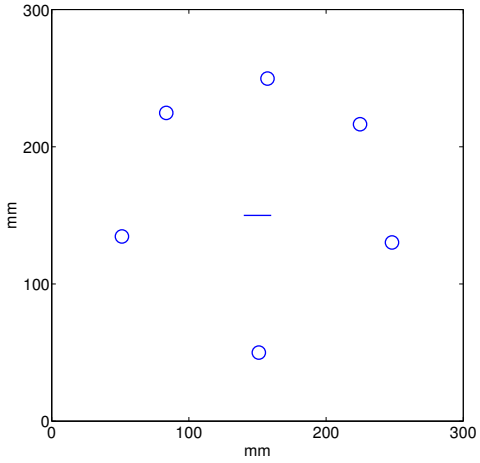

(c) Array configuration #5

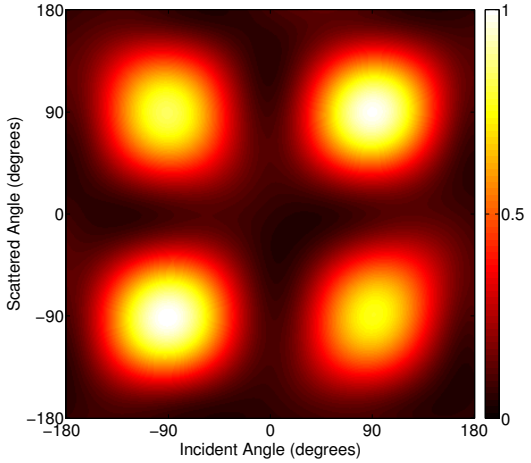

(d) Estimated scattering matrix #5

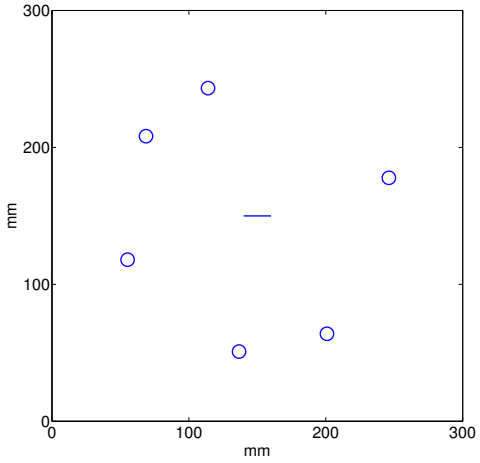

(e) Array configuration #6

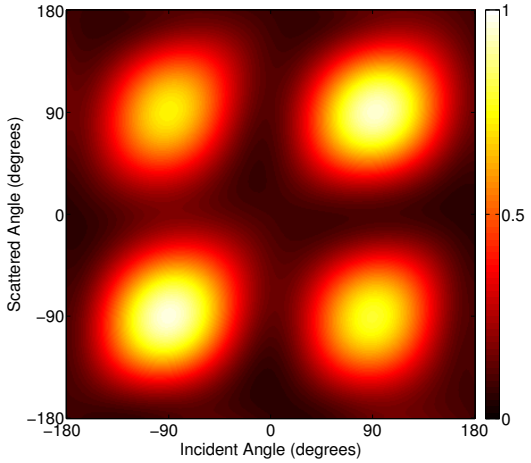

(f) Estimated scattering matrix #6

Figure 17: Array configurations from the results of the Monte Carlo simulation. The left column shows array designs and the right shows estimated scattering matrices. The RMS error is 0.0456 for array #4, 0.0450 for array #5, and 0.0424 for array #6.

4.2 Sparse Array Imaging with Estimated Scattering Patterns

Scattering matrices can also be incorporated into different guided wave SHM algorithms to improve detection and characterization performance. One example is to include them as part of an overall propagation model to enhance detection using a maximum likelihood-based approach [144]. Another promising approach is to incorporate scattering matrices with sparse array imaging algorithms to improve the performance of SHM systems for defect characterization [15]. The following section reviews two Lamb wave sparse array imaging algorithms and demonstrates the efficacy of using the previously estimated scattering patterns with the MV imaging method for damage characterization.

4.2.1 Experimental Setup

An aluminum plate specimen with dimensions of 292 mm $\times$ 610 mm $\times$ 3.18 mm was used to mimic an actual part in realistic engineering structures. As shown in Figure 18, the plate was instrumented with an array of six piezoelectric transducers attached using two-component epoxy. The transducers were fabricated from 7 mm diameter, 300 kHz, radial mode PZT discs. An NI PXI-5412 waveform generator was programmed to apply a 50-to-500 kHz linear chirp excitation to the transducers, and an NI PXI-2593 multiplexer was used to switch the 15 unique transmit-receive pairs. The signals were digitized with an NI PXI-5122 14-bit digitizer at a sampling frequency of 20 MHz. Fifty waveforms were averaged for each acquisition and the final output was filtered to obtain the equivalent response to a 3-cycle, 100 kHz, tone burst [35] for which the A_0 mode was dominant. A 5.1 mm diameter through-thickness hole was drilled to simulate a fastener hole and a set of reference data was recorded. A notch was then cut from the hole at an orientation of -50° and two more sets of data were recorded for different notch sizes as summarized in Table 1.

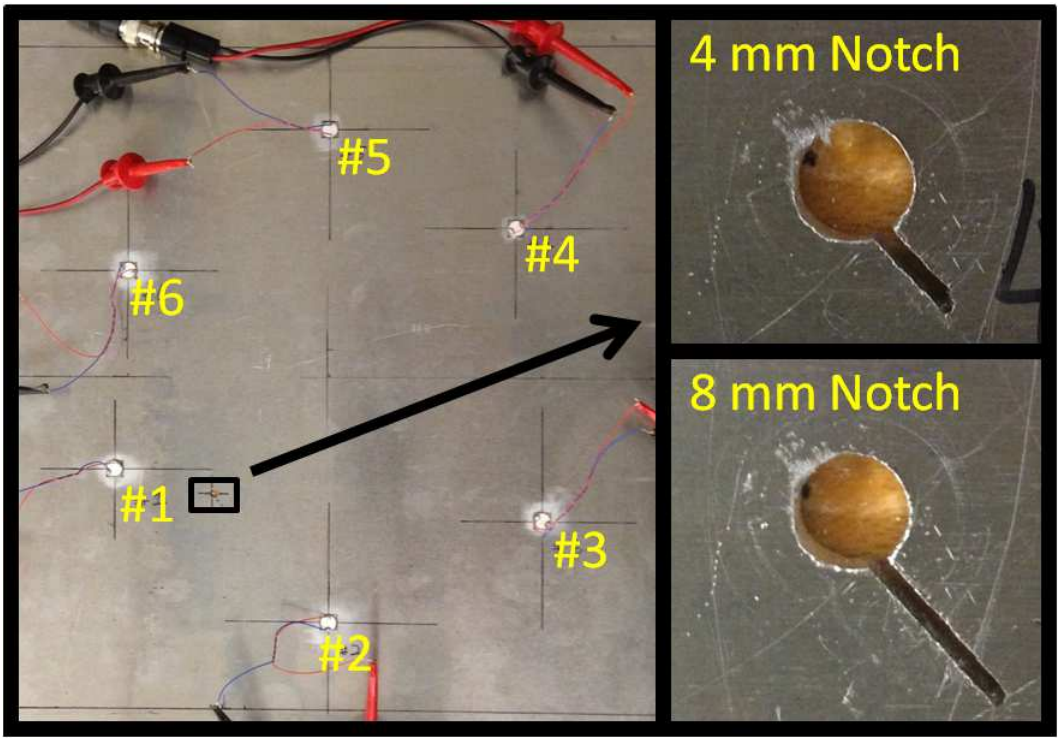

Figure 18: Small aluminum plate specimen instrumented with an array of six transducers. Close-up images are shown of the 4 mm and 8 mm notches.

Table 1: Summary of data sets acquired

Data Set	Description
1	5.1 mm diameter through-thickness hole
2	4 mm notch
3	8 mm notch

4.2.2 Analysis Methodology

4.2.2.1 Sparse Array Imaging Methods

The two sparse array imaging methods described here are conventional delay-and-sum (DAS) imaging and minimum variance (MV) imaging. Both algorithms use differenced signals after baseline subtraction, and readers are referred to the literature for detailed descriptions of these imaging methods [12, 18, 42, 145]. Both DAS and MV images generated using a sparse array should be interpreted as detection and localization maps since the small number of spatially distributed elements are not able to "image" the details of a scatterer in the same manner as a true phased array.

The DAS method requires little *a priori* information, and, as its name suggests, shifts the array signals in time and sums them. For transducer pair i, if a scatterer is introduced at location (x, y), the delay time is computed as :

$$t_{ixy} = \frac{d_{ixy}}{c_g}, \tag{9}$$

where d_{ixy} is the total distance of Lamb wave propagation from the transmitter to the receiver by way of the scatterer, and c_g is the group velocity. The image value at pixel (x, y) is calculated as:

$$P_{xy} = \left| \sum_{i}^{M} w_{ixy} r_i \left(t - t_{ixy}\right) \right|^2, \tag{10}$$

where $r_i\left(t\right)$ is the differenced (or residual) signal for transducer pair i and w_{ixy} is a weighting coefficient that is specific to both the transducer pair and the pixel location. Eq. (10) can be rewritten in matrix format as:

$$P_{xy} = \mathbf{w}_{xy}^{\mathrm{H}} \mathbf{R}_{xy} \mathbf{w}_{xy}, \tag{11}$$

where "H" denotes the Hermitian transpose operation, $\mathbf{w}_{xy}$ is a vector of weighting coefficients, and $\mathbf{R}_{xy}$ is a singular autocorrelation matrix defined as $\mathbf{R}_{xy} = \mathbf{r}_{xy}\mathbf{r}_{xy}^{H}$. $\mathbf{r}_{xy}$ is a vector containing all $r_i\left(t - t_{xy}\right)$ values for pixel location (x, y). Because the

DAS method as used here does not use any *a priori* information about potential scatterers, each element of the weighting coefficient vector $\mathbf{w}_{xy}$ is assigned a constant value, typically one or $1/M$.

While DAS imaging is capable of performing reasonably well for damage detection and localization, the resulting images frequently contain large artifacts and provide little or no information about damage characteristics. Adaptive imaging methods, on the other hand, are able to achieve better performance than DAS imaging and also have the potential to characterize damage if *a priori* knowledge is incorporated. One example is the MV sparse array imaging method [12]. Rather than using constant values, the weighting coefficients in MV imaging are determined by satisfying the following condition:

$$P_{xy} = \min_{x} \mathbf{w}_{xy}^{\mathrm{H}} \mathbf{R}_{xy} \mathbf{w}_{xy}, \quad \text{such that } \mathbf{w}_{xy}^{\mathrm{H}} \mathbf{e}_{xy} = 1, \tag{12}$$

where $\mathbf{e}_{xy}$ is a unit norm vector called the "steering vector" and has elements proportional to expected scattered amplitudes. By incorporating S_{ixy}, the scattering coefficient for transducer pair i from damage at pixel location (x, y), $\mathbf{e}_{xy}$ is of the form:

$$\mathbf{e}_{xy} \propto \left[\frac{S_{1xy}}{\sqrt{d_{1xy}^{\times}}} \cdots \frac{S_{Mxy}}{\sqrt{d_{Mxy}^{\times}}} \right]^{T} \tag{13}$$

where $d_{ixy}^{\times}$ is the product of the propagation distance from transmitter to pixel location (x, y) and the propagation distance from pixel location (x, y) to receiver for transducer pair i. With such a steering vector, Eq. (12) can be interpreted as minimizing each pixel value while preserving the pixel values that correspond to expected scattering behavior.

The weighting coefficient vector $\mathbf{w}_{xy}$ can be solved using Lagrange multipliers as

$$\mathbf{w}_{xy}^{\mathrm{MV}} = \frac{\mathbf{R}_{xy}^{-1} \mathbf{e}_{xy}}{\mathbf{e}_{xy}^{\mathrm{H}} \mathbf{R}_{xy}^{-1} \mathbf{e}_{xy}}, \tag{14}$$

where the "-1" denotes the matrix inverse. Because $\mathbf{R}_{xy}$ is a singular matrix, its inversion is regularized through diagonal loading. Another advantage of applying diagonal loading is that it can increase the robustness of the MV imaging method to errors in the steering vector.

4.2.2.2 Scattering Matrix Estimation and Rotation

Using appropriate scattering information is critical to the performance of MV imaging. The estimation method described in Chapter 3 provides a feasible way to obtain reasonable far field scattering behavior of Lamb waves. Scattering matrices for two notches of different lengths at an orientation of $-50°$ emanating from a 5 mm diameter through-hole are presented here and subsequently used for imaging. These scattering matrices are for the 100 kHz, 3-cycle A_0 Lamb wave mode and both of them were generated by rotating the scattering matrices obtained from a separate experiment using the estimation methodology described in Chapter 3. The matrix rotation allows a new scattering matrix to be obtained for the same scatterer but at a different orientation from that of a known one and is

$$S_{\text{new}}(\boldsymbol{\theta}) = S_{\text{known}}(\boldsymbol{\theta} + [\Delta\psi, \Delta\psi]), \tag{15}$$

where $\Delta\psi = \psi_{\text{new}} - \psi_{\text{known}}$ is the angular difference between scatterer orientations. As shown in Figures 19(a) and 19(b), both matrices demonstrate the expected highly directional scattering behavior of the notches. The two high-value regions along the main diagonal quantifies forward scattering behavior to the notch, i.e., a scattered wave propagating in the same direction as the incident wave. Direct backscattering, which are the other two high-value regions , corresponds to the incident and scattered angles differing by 180°. As the length of notch increases from 4 mm to 8 mm, the extents of both the forward and back scattering lobes increase, and the backscattered amplitudes increase relative to the larger forward scattered amplitudes.

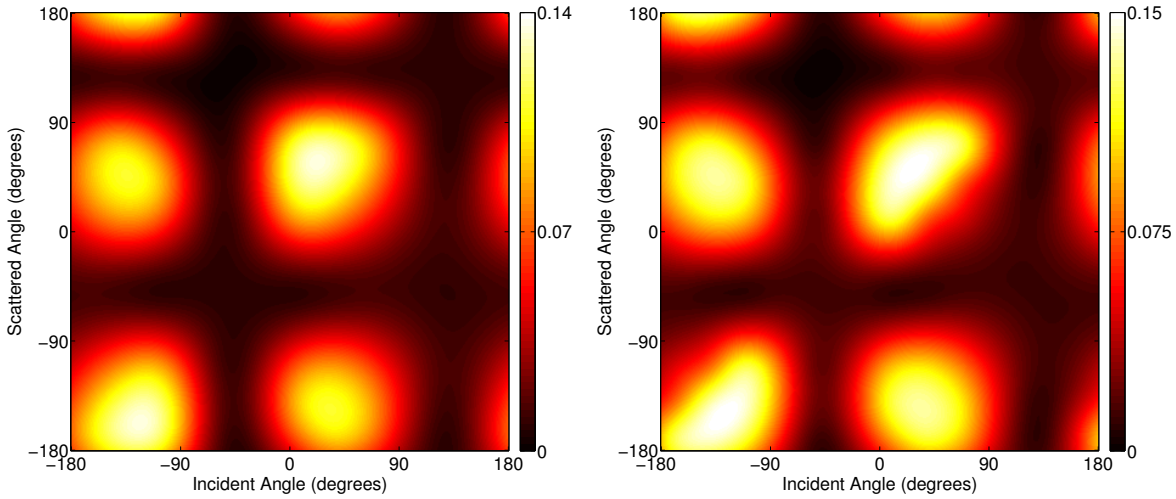

(a) 4 mm notch (b) 8 mm notch

Figure 19: Scattering matrices for the 100 kHz, 3 cycle A_0 mode describing the far-field scattering from: (a) a 4 mm through-thickness notch; and (b) a 8 mm through-thickness notch. Both matrices are estimated results obtained from a separate experiment, where both notches originate from a 5 mm diameter through-hole at a $-50°$ orientation.

4.2.3 Results

4.2.3.1 Sparse array imaging results

Both the DAS and MV images of the two notches are shown in Figure 20. These images clearly demonstrate that the MV imaging algorithm significantly reduces artifacts and improves detection and localization performance as compared to the simpler DAS method. Figures 20(c) and 20(e) are both the MV images of the 4 mm notch but using scattering matrices of two different notch lengths. Although both of them indicate the defect correctly, the peak amplitude of Figure 20(c), which uses the scattering matrix of a 4 mm notch that matches the real defect size, is larger than that of Figure 20(e), which uses the scattering matrix of an 8 mm notch. The same results can also be observed by comparing the two MV images of the 8 mm notch shown in Figures 20(d) and 20(f). Such peak amplitude differences indicate that the scattering behavior of a defect has the potential to be used to obtain at least a rough estimate of its size.

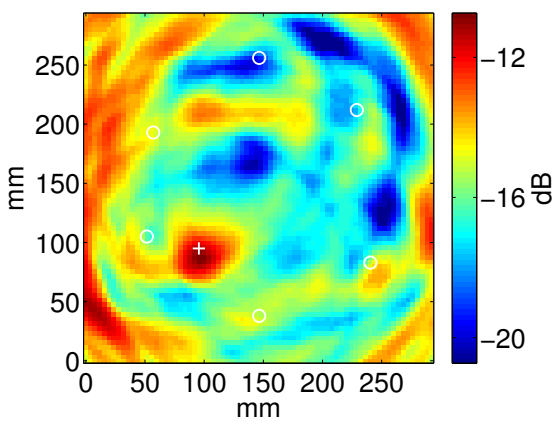

(a) DAS image of the 4 mm notch

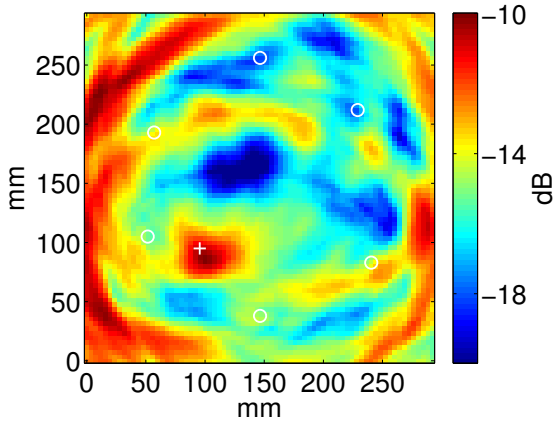

(b) DAS image of the 8 mm notch

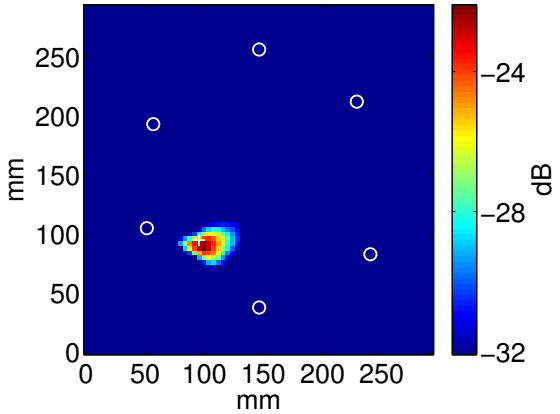

(c) MV image of the 4 mm notch using the scattering matrix of a 4 mm notch

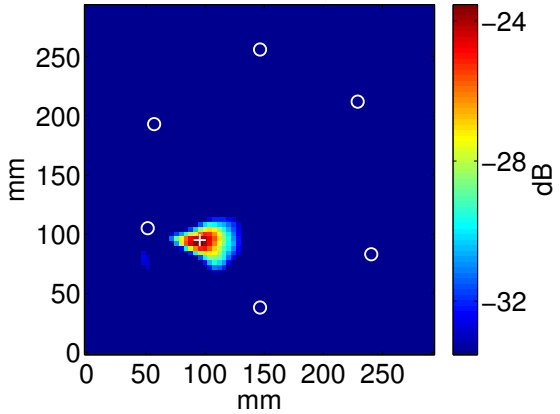

(d) MV image of the 8 mm notch using the scattering matrix of a 4 mm notch

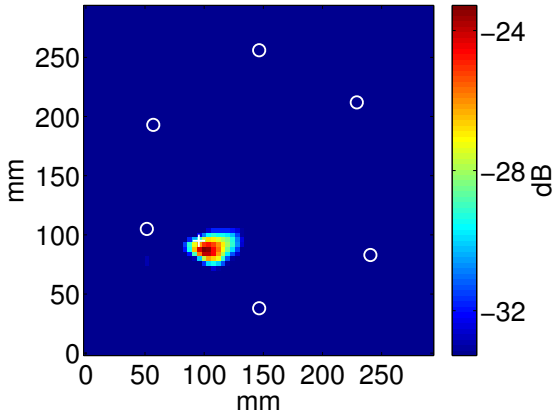

(e) MV image of the 4 mm notch using the scattering matrix of an 8 mm notch

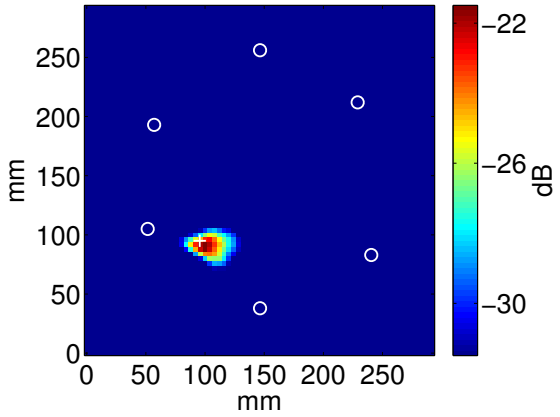

(f) MV image of the 8 mm notch using the scattering matrix of an 8 mm notch

Figure 20: DAS and MV images for the two notches originating from a through-hole. DAS results are shown in the top row (a and b). MV images using the scattering matrix of a 4 mm notch are shown in the middle row (c and d). MV images using the scattering matrix of an 8 mm notch are shown in the middle row (e and f). Each image is shown on a 10 dB color scale normalized to its maximum amplitude.

4.2.3.2 Orientation curves

The images of Figure 20 confirm the potential of incorporating proper scattering information for improved crack detection if the crack orientation is known. If the orientation information is not known, an extended method is to generate multiple MV images with scattering matrices corresponding to assumed scatterer orientations ranging from $-180°$ to $+180°$ (here with a $1°$ increment) and then plot the maximum amplitude of each image as a function of orientation [15]. This plot of amplitude versus assumed defect orientation is referred to here as an orientation curve. It is more efficient to generate this curve using a small region around the scatterer location, which could be determined to encompass a known high-stress "hot spot." Alternatively, a reduced monitoring area could be defined after preliminary detection with either DAS imaging or MV imaging with a uniform scattering matrix.

Figure 21(a) shows the orientation curve for the 4 mm notch generated using the scattering matrix of a 4 mm notch and an 80 mm $\times$ 80 mm monitoring area centered on the hole. The two peaks in the figure clearly indicate that the notch is highly directional, and the largest peak is located at $-55°$, which is a reasonable estimate of the true orientation of $-50°$. There is a second, smaller peak at about $128°$, which is approximately $180°$ from the main peak and is present because the scattering matrices for a notch on one side of the hole versus the other are very similar. The result for the 8 mm notch is shown in Figure 21(b), where its orientation curve was generated using the scattering matrix of an 8 mm notch and an 80 mm $\times$ 80 mm monitoring area centered on the hole. Similar to Figure 21(a), the two peaks are about $180°$ apart, where the larger one is at $-53°$ and the smaller one is at $129°$. Orientation curves with double peaks separated by about $180°$ are characteristic signatures of notch (or any linear scatterer).

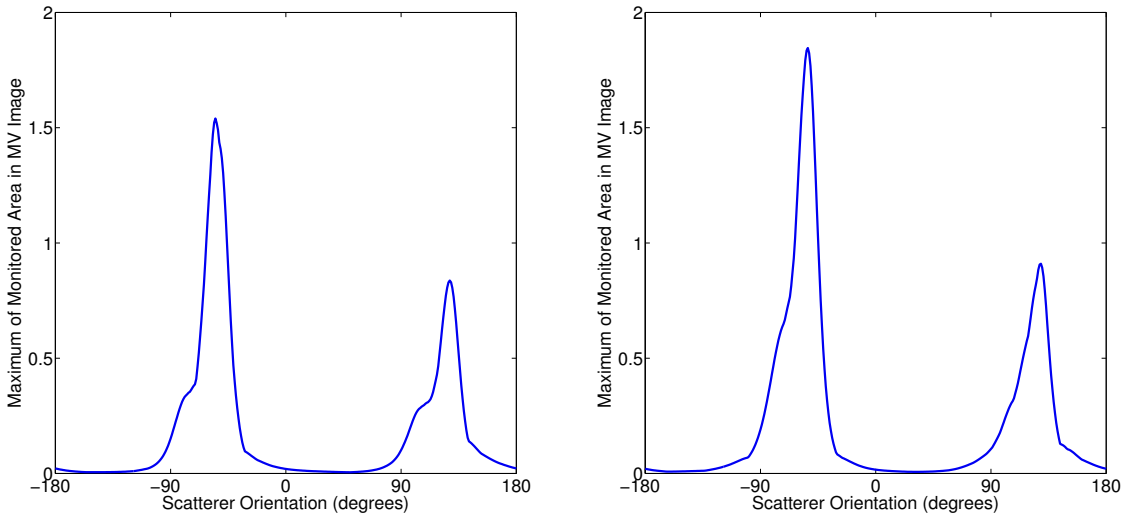

(a) 4 mm notch (b) 8 mm notch

Figure 21: Orientation curves for two notches of different lengths: (a) the 4 mm notch using the scattering matrix of a 4 mm notch; and (b) the 8 mm notch using the scattering matrix of an 8 mm notch.

4.3 Summary

This chapter has described two applications of the scattering pattern estimation methodology. This first one uses it to evaluate the ability of a transducer array configuration to capture scattering information for a specific defect. Three typical array configurations were analyzed and a Monte Carlo simulation was performed to provide some guidance for the design of sparse transducer array configurations. One finding is that it is critical for an array to obtain information for both strong and weak parts of the scattering pattern for directional scatterers, such as cracks, to be able to estimate the total scattering matrices. Another observation from a sparse transducer array working in pitch-catch mode is that a trade-off exists between placing transducers close together to obtain direct backscattering versus further part to obtain a wider range of interrogation angles.

The second application is to incorporate the scattering matrices obtained from estimation with Lamb wave sparse array imaging methods for defect monitoring. Scattering matrices of notches of different lengths at one orientation estimated from

one plate are shown to be useful for the detection, localization, and characterization of similar notches at a different orientation in another plate. The orientation information of notches was obtained from orientation curves generated using the MV imaging with rotated scattering matrices. A characteristic signature of the orientation curves of notches (or any linear scatterer) is having two peaks separated by 180°, which can be used to discriminate them from other scatterers.

CHAPTER V

LOAD-ENHANCED METHODS FOR THE *IN SITU* DETECTION, LOCALIZATION, AND CHARACTERIZATION OF SCATTERERS

The sparse array imaging methods introduced previously are extended in this chapter to structures with complex geometries for the detection, localization, and characterization of fatigue cracks. A series of fatigue tests were conducted on aluminum plate specimens with increasing geometric complexity and Lamb wave signals were recorded at different loads and at various number of cycles throughout fatiguing. A "baseline-free" load-differential DAS imaging method is used first for fatigue crack detection and localization. Then, load differential features are extracted from these images that capture the effects of loading as cracks are opened. Damage detection thresholds are adaptively set based upon the load-differential behavior of two features, which further enables implementation of an automated fatigue crack detection process. Based on the detection from the load differential DAS images as well as the features, corresponding load-differential MV images are generated by incorporating assumed scattering patterns obtained from estimation results described in Chapter 3. Discrimination of cracks from several types of benign scatterers is accomplished by identifying characteristic patterns in the orientation curves. Large portions of this chapter have been reported in [1, 23, 25].

5.1 Analysis Methodology

The methodology applied here for data analysis is almost the same as that of Chapter 4.2 except for calculating the residual signals used in Eq. 10. Instead of subtracting

baseline signals (recorded when the plate is assumed to have no damage) from current signals of interests (which were recorded after damage is introduced), the residual signals here are obtained from subtracting signals at the same damage state but a different load, i.e., the residuals are load-differential signals. The DAS and MV imaging algorithms using these load-differential signals are referred to as "load-differential DAS imaging" and "load-differential MV imaging", respectively.

5.2 Fatigue Test #1: Simple Plate

5.2.1 Experimental Setup

Fatigue cracks were initiated and grown in a 6061-T6 aluminum alloy plate of dimensions 305 mm × 610 mm × 3.18 mm. As can be seen in Figure 22, an array of six piezoelectric transducers was affixed to one side of the plate using two-component epoxy, and each transducer was further backed with a bubble-filled epoxy protection layer. The surface-mounted transducers were fabricated from 300 kHz, radial mode PZT discs (7 mm in diameter and 0.5 mm thick).

The aluminum specimen was then mounted in a servo-hydraulic test machine running in load control mode. A NI PXI-5412 waveform generator was used to generate a linear chirp excitation sweeping from 50 to 500 kHz with a duration of 0.2 ms. A Panametrics 5072PR pulser-receiver was used to amplify the received signals, and a custom multiplexer switched between the 15 unique transmit-receive pairs. The received signals were then digitized by a NI PXIe-5122 14-bit digitizer at a sampling frequency of 20 MHz. For each acquisition, 20 waveforms were averaged to improve the signal-to-noise ratio.

The broadband chirp excitation resulted in multiple Lamb wave modes propagating in the plate. Received signals were filtered to yield the equivalent narrow-band tone burst response as described in [35]. A 3-cycle Hanning windowed tone burst response centered at 100 kHz was selected because of the purity of the A_0 mode and

its sensitivity to through-thickness cracks.

Prior to fatiguing the specimen, a set of reference signals was recorded from the pristine sample. A through-hole measuring 5.1 mm in diameter was then drilled in the center of the plate, and a small starter notch was introduced on the left side of the hole as a site for crack initiation. The plate was fatigued with a 3 Hz sinusoidal tension-tension load profile ranging from 16.5 to 165 MPa. Fatiguing was periodically paused and ultrasonic data were recorded as a function of applied static tensile load from 0 to 115 MPa in steps of 11.5 MPa, which corresponds to 0% to 100% load with a 10% load step (11 loading conditions for each data set). Fatiguing was continued until the largest crack was about 25 mm in length, and a total of 14 data sets were recorded. Fatigue cycles and observations of the cracks, which were measured using a caliper, are summarized in Table 2 for each data set, and photographs of the cracks after data sets 7, 10 and 14 are shown in Figure 22.

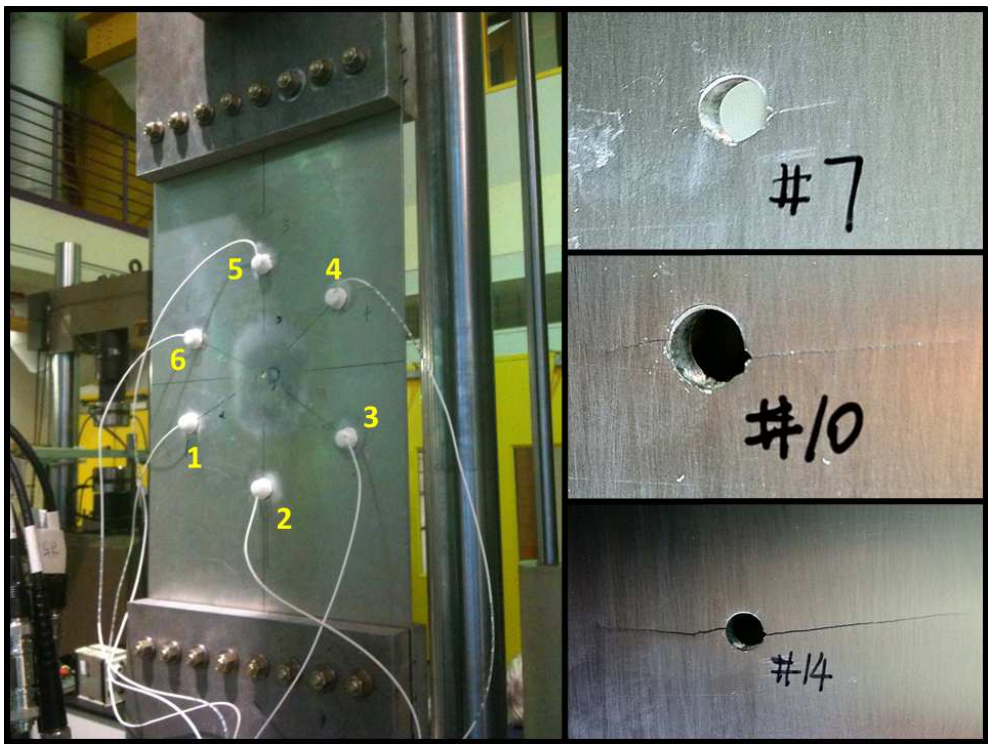

Figure 22: Aluminum plate specimen with attached transducers (numbered 1 through 6) of fatigue test #1 mounted in the MTS machine prior to fatiguing (left), and photographs of fatigue cracks corresponding to data sets 7, 10 and 14 (right).

Table 2: Summary of data sets acquired from fatigue test #1 : simple plate

Data Set	Fatigue Cycles	Notes/Crack Length at Surface (mm)	
		Left	Right
1	0	Baseline, no hole, no notch	
2	0	5.1 mm diameter hole drilled	
3	0	Starter notch cut (left, front of hole)	
4	5,000	No visible cracks	
5	8,000	1.6	----
6	10,000	3.6	----
7	12,500	5.4	----
8	15,500	7.7	----
9	17,000	9.9	----
10	18,500	13.4	4.7
11	19,500	16.8	8.4
12	20,000	19.5	11.5
13	20,400	22.7	15.6
14	20,600	25.2	18.8

(Orientation relative to side with transducers)

5.2.2 DAS Imaging with Damage-Free Reference Signals

The previously-described DAS imaging algorithm was first applied to residual signals computed from damage-free reference signals. Consider images constructed from data set 2 (current signals) and data set 1 (damage-free reference signals), between which the only difference is the drilling of a center through-hole. Figure 23 shows three images that were generated from current signals and reference signals recorded under identical loads. These and subsequent figures were created with a pixel resolution of 4 mm. Under the matched loads of 0%, 50% and 100%, the three images are almost identical because the static load has minimal effects on the through-hole.

The results are much different when the imaging algorithm was applied to the same data sets but under mismatched loads. Figure 24 shows three images also constructed

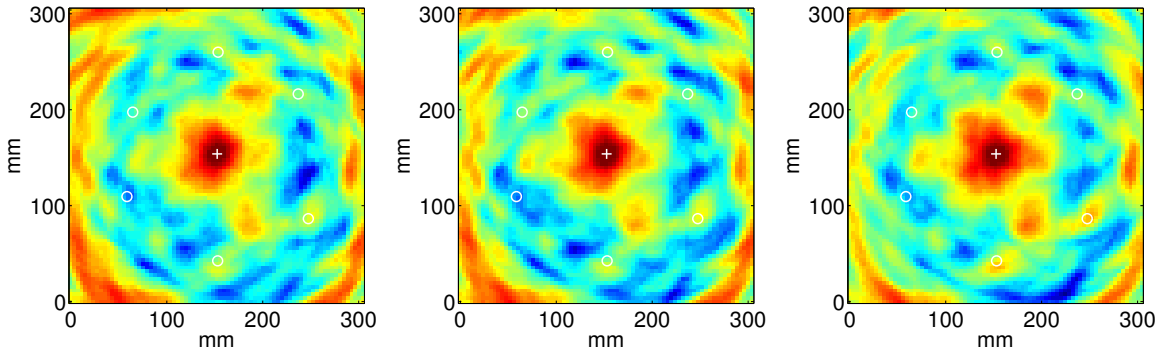

(a) DAS image of the hole at 0%/0% load

(b) DAS image of the hole at 50%/50% load

(c) DAS image of the hole at 100%/100% load

Figure 23: DAS images generated between data set 1 (baseline signals) and data set 2 (current signals, after hole drilled) of fatigue test #1 under matched loads. (a) 0 MPa (0% load), (b) 57.5 MPa (50% load), and (c) 115 MPa (100% load). All three images are shown on the same 10 dB color scale (−24 dB to −14 dB).

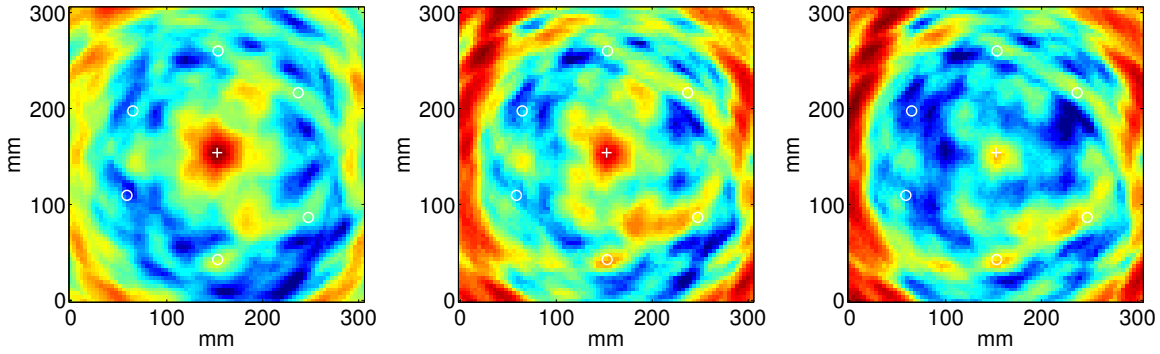

(a) DAS image of the hole at 0%/20% load

(b) DAS image of the hole at 0%/60% load

(c) DAS image of the hole at 0%/100% load

Figure 24: DAS images generated between data set 1 (baseline signals) and data set 2 (current signals, after hole drilled) of fatigue test #1 under mismatched loads. All three images are shown on a 10 dB color scale normalized to their maximum amplitudes. (a) 0/23 MPa (0/20% load), max amplitude of −13 dB. (b) 0/69 MPa (0/60% load), max amplitude of −12 dB. (c) 0/115 MPa (0/100% load), max amplitude of −8 dB.

between data sets 1 and 2, where the reference signals were recorded under zero load and the current signals were recorded under 20%, 60% and 100% loads. Although a 20% load mismatch exists for Figure 24(a), the image is not significantly degraded from those of Figure 23, and the center hole is clearly observed. However, the image with a 60% load mismatch is obviously degraded as Figure 24(b) shows with the largest amplitude features in the image being artifacts near the plate edges. The image of Figure 24(c) with a 100% load mismatch is degraded to a degree that the hole is no longer detectable.

Image degradation under mismatched loads can be explained by the effects of applied loads on Lamb wave propagation. Two primary effects are wave speed changes as a result of the acoustoelastic effect and specimen dimension changes [114]. Both of these changes perturb the TOA of individual echoes, and thus result in significant residual signals from baseline subtractions regardless of whether damage has also been introduced.

Now consider images obtained from data set 7 (current signals) and data set 3 (reference signals), where the primary difference between the two data sets is a 5.4 mm long single crack. Unlike Figure 23, which illustrates that matched applied loads have only very small effects on the through-hole, Figure 25 shows much more significant effects that applied loads can have on a fatigue crack. As shown in Figure 25(a), the crack is not detectable under zero load because it is still tightly closed. By increasing the applied load, clear crack detection is obtained as the crack opens. Figure 25(b) is generated under 50% load and Figure 25(c) is generated under 100% load, and it is obvious that higher loads open the crack more completely and thus the images are improved.

Figure 26 shows images from data set 3 and data set 7 under mismatched loads where current signals were all recorded under 0% load but reference signals were recorded under 20%, 60% and 100% loads. The crack is closed under zero load and

thus the Lamb waves propagate through it with almost no measurable effect. This situation produces images that are equivalent to those that would be obtained if there were no damage and thus illustrate the effects of applied loads only. These images show that the mismatched loads generate stronger artifacts around the image edges; however, the maximum residual signal energy from these artifacts, as shown in Figure 26(c) for the greatest load mismatch, is about 2 dB less than that from the opened crack shown in Figure 25(c).

Figure 27 shows the images of data set 3 and date set 7 under mismatched loads where current signals were recorded under 100% load and reference signals were recorded under 0%, 40% and 80% loads. As shown in Figures 27(a) and 27(b), the crack is not clearly detected when the loads are significantly mismatched even though it is fully opened. The image of Figure 27(c), which has only a 20% load mismatch, clearly shows the crack and is not significantly degraded from Figure 25(c). These results, along with the image of Figure 24(a) for the hole, indicate that load mismatches of up to 20% (23 MPa) can be tolerated.

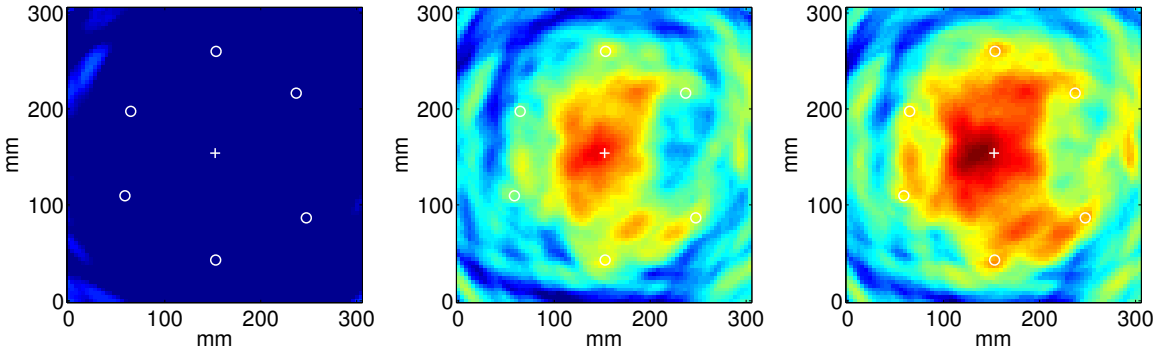

(a) DAS image of the crack at 0%/0% load

(b) DAS image of the crack at 50%/50% load

(c) DAS image of the crack at 100%/100% load

Figure 25: DAS images generated between data set 3 (baseline signals) and data set 7 (current signals, 5.4 mm long fatigue crack) of fatigue test #1 under matched loads. (a) 0 MPa (0% load), (b) 57.5 MPa (50% load), and (c) 115 MPa (100% load). All three images are shown on the same 10 dB color scale (−16 dB to −6 dB).

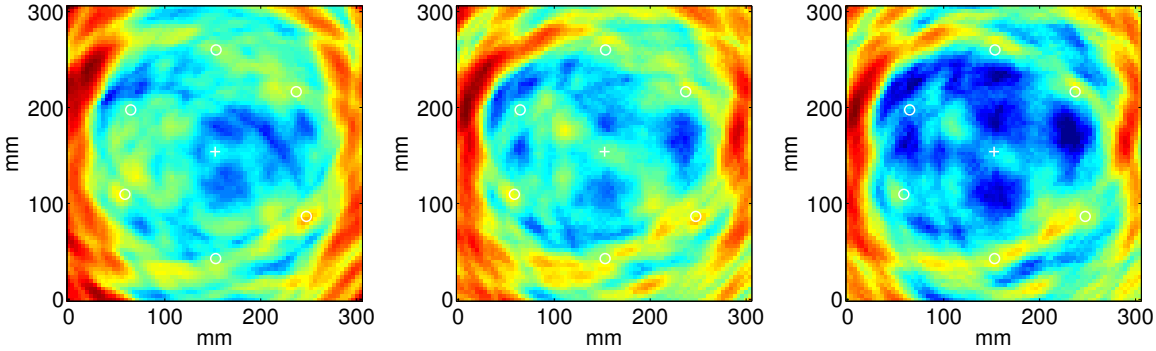

(a) DAS image of the crack at 20%/0% load

(b) DAS image of the crack at 60%/0% load

(c) DAS image of the crack at 100%/0% load

Figure 26: DAS images generated between data set 3 (baseline signals) and data set 7 (current signals, 5.4 mm long fatigue crack) of fatigue test #1 under mismatched loads. All three images are shown on a 10 dB color scale normalized to their maximum amplitudes. (a) 23/0 MPa (20/0% load), max amplitude of −14 dB. (b) 69/0 MPa (60/0% load), max amplitude of −12 dB. (c) 115/0 MPa (100/0% load), max amplitude of −8 dB.

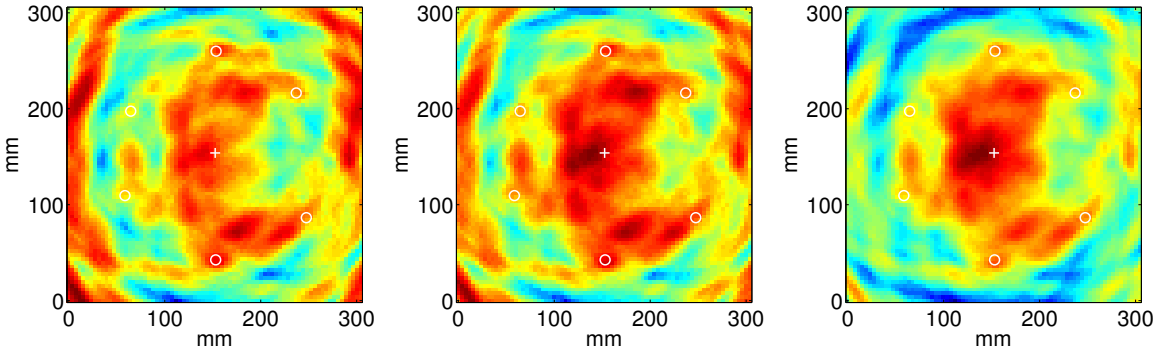

(a) DAS image of the crack at 0%/100% load

(b) DAS image of the crack at 40%/100% load

(c) DAS image of the crack at 80%/100% load

Figure 27: DAS images generated between data set 3 (baseline signals) and data set 7 (current signals, 5.4 mm long fatigue crack) of fatigue test #1 under mismatched loads. All three images are shown on a 10 dB color scale normalized to the maximum amplitude of each image. (a) 0/115 MPa (0/100% load), max amplitude of −5 dB. (b) 46/115 MPa (40/100% load), max amplitude of −6 dB. (c) 92/115 MPa (80/100% load), max amplitude of −6 dB.

5.2.3 Crack Detection Using Load-Differential DAS Imaging

The results of Section 5.2.2 motivate an alternative approach for fatigue crack detection and localization — load-differential imaging. For this method, signals recorded under one load are referred to the "reference signals" and the signals recorded at the same damage state but under a slightly increased tensile load are called the "current signals". Differences between the signals are thus caused by a combination of crack opening effects and load effects. Figures 24(a) and 27(c) indicate that a 20% load difference (or less) will not adversely affect imaging of damage. To minimize artifacts resulting from loads while maintaining detection, a 10% load difference is considered. The reference signal loads start from 0% and end at 90% with a increment of 10%, and the current signal loads range from 10% to 100% accordingly; a total of 10 differential-load pairs are thus considered for each data set.

5.2.3.1 Pair-wise load-differential signals

Figure 28 shows received signals at 11 loads from two transducer pairs of data set 10, where two cracks are present. Signals for each transducer pair are normalized by the peak amplitude of the first arrival at 0% load, where cracks are assumed to be less opened or possibly even closed. Figure 28(a) shows signals from transducer pair 2–5 (i.e., transmitting on 2 and receiving on 5), where the incident wave is broadside to the cracks and the received signals are thus strongly affected by opening of the cracks with load. An abrupt amplitude drop occurs between 0% and 10% load within the time window of the first arrival (between 80 and 110 ms). The signals amplitude continues to decrease as loads increase and further open the cracks. Figure 28(b) shows signals from the transducer pair 1–3, where the direct path does not go through the cracked area and thus received signals are less affected by the cracks. The signal amplitude and shape change with load between 90 and 120 ms, which corresponds to the propagation path from the transmitter to the cracks to the receiver.

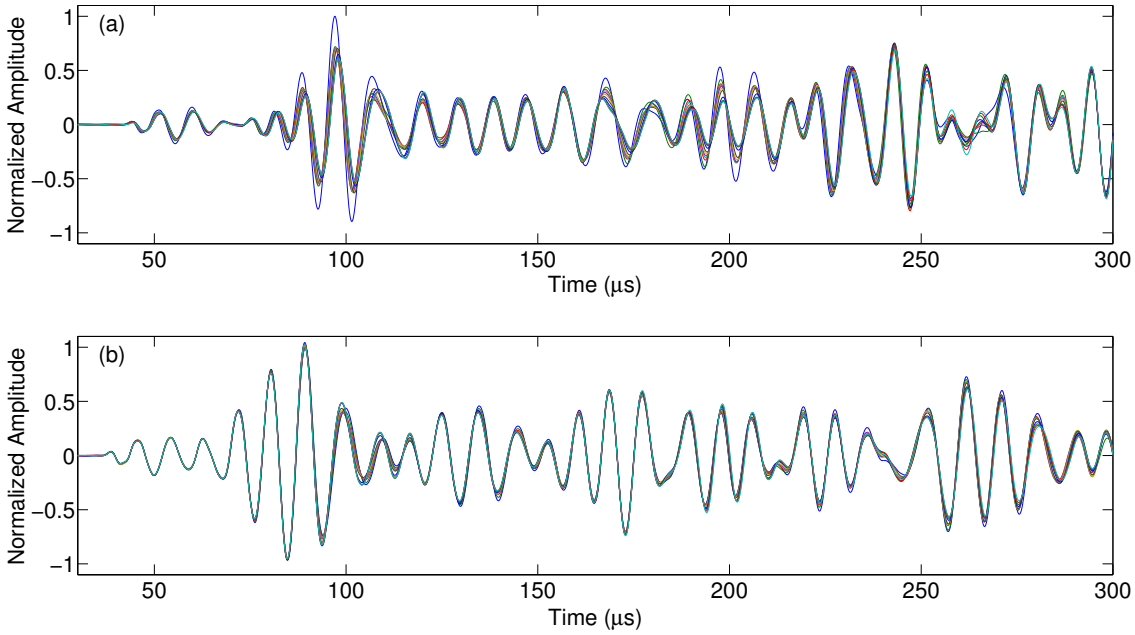

Figure 28: Signals recorded from data set 10 of fatigue test #1 at 11 loads ranging from 0 to 115 MPa (0 to 100%). (a) Transducer pair 2–5, and (b) transducer pair 1–3.

Figure 29 shows waterfall plots of the ten load-differential signals for transducer pairs 2–5 and 1–3, where signals are normalized as previously described prior to subtraction. Figure 29(a) shows more clearly that the larger crack on one side of the hole opens up at 10% load and blocks the transmitting guided wave, resulting in the large amplitude change of the first arrival. At about 70% load the smaller crack on the other side opens up and decreases the signal amplitude further. For Figure 29(b), the residual signals correspond to guided waves reflected from the crack site. Similar effects can be observed as one crack opens at lower load and another crack opens at higher load.

5.2.3.2 Crack detection using load-differential DAS images

Load-differential signals such as shown in Figure 29 can be used as the differenced signals in Eq. 10 to generate ten load-differential images for each data set, which correspond to differential loads ranging from 0–10% to 90–100%. Figure 30 is the image collage constructed from all 14 data sets recorded from the fatigue test where

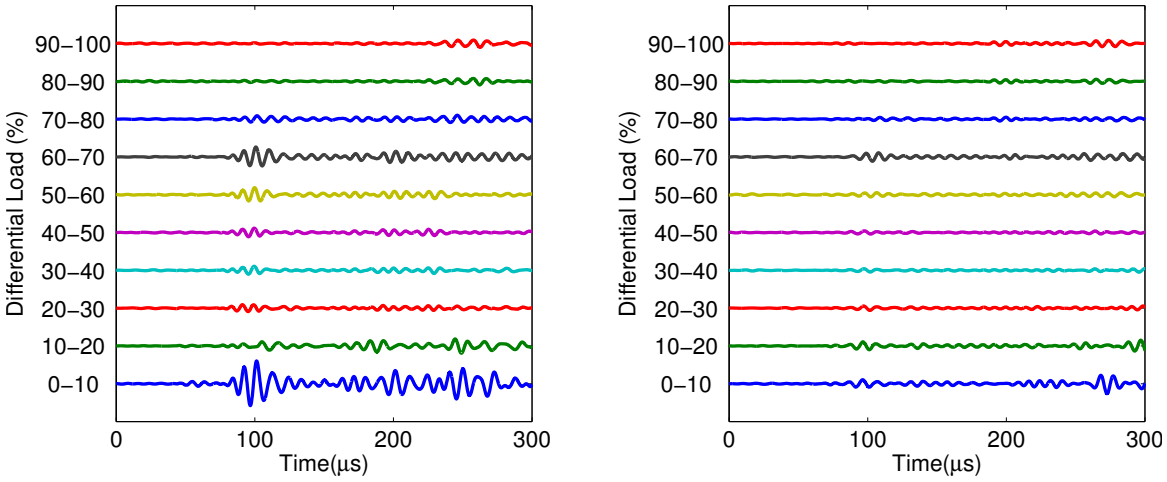

(a) Transducer pair 2–5

(b) Transducer pair 1–3

Figure 29: Differential signals from data set 10 of fatigue test #1 at ten differential loads (0–10%, 10–20%, ... , 90–100%). (a) Transducer pair 2–5, and (b) transducer pair 1–3.

all images are shown on the same 30 dB color scale. The 40 images from the first four data sets are very similar because there are no cracks even though there are significant changes to the specimen (i.e., introduction of the drilled hole and starter notch). The first crack is barely seen at 40% load from the images of data set 6, and is clearly visible by data set 7. From data set 7 to 9, images that show the crack appear at progressively lower loads, which is consistent with the crack growing as fatiguing continues and thus becoming easier to open at lower loads. For data set 10, the crack on one side of the hole starts to open at very low loads (0–10% load), whereas the crack on the other side of the hole opens up at higher loads (50–60% load); both cracks are completely opened at 90% load. Images from data sets 11 through 14 continue to show that the cracks become easier to open at low loads as both cracks keep growing. By data set 14 both cracks are very large, but there is still some evidence that they are not opening simultaneously.

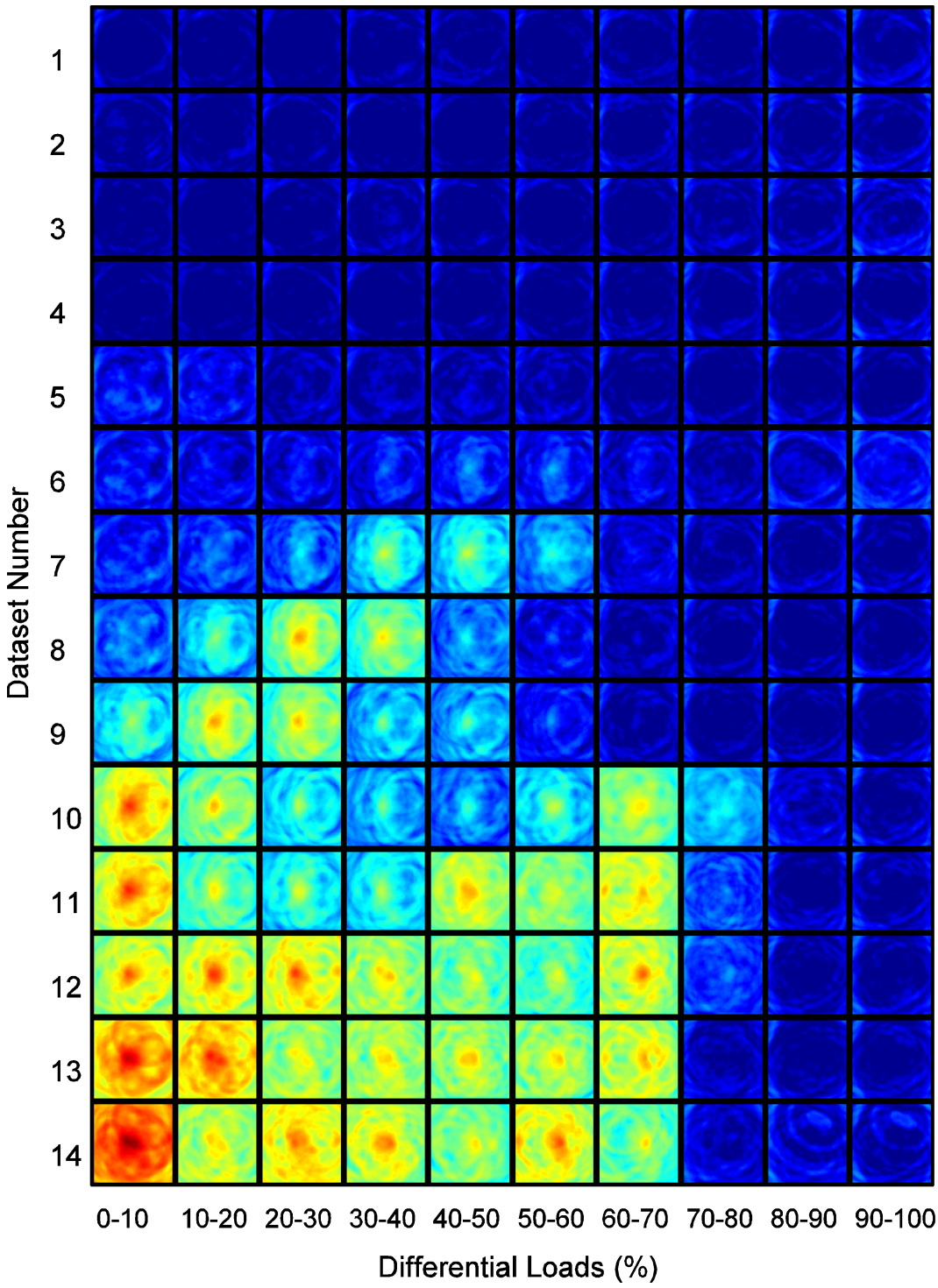

Figure 30: Load-differential DAS images from data sets 1–14 of fatigue test #1 plotted on a fixed 30 dB scale (−20 dB to 10 dB).

5.2.4 Crack Localization Using Load-Differential DAS Imaging

The load-differential images also suggest that it may be possible to discriminate between the two cracks on either side of the hole. For example, Figure 31 shows three images from data set 12 under differential loads of 20-30%, 30-40%, and 60-70%. For this data set, the crack on the left side of the hole is 19.5 mm in length, whereas the one on the right side is 11.5 mm. At lower loads, the larger crack opens first, and Figure 31(a) shows the indication on the left side of the hole as the load changes from 20% to 30%. When the load further increases from 30% to 40%, there are indications in the image on both sides of the hole as can be seen in Figure 31(b), presumably corresponding to the left crack becoming fully opened and the right crack starting to open. Finally, as can be seen in Figure 31(c), the indication in the image is completely on the right side of the hole as the load increases from 60% to 70% and the right crack becomes fully opened. Given the generally low resolution of delay-and-sum images generated from a sparse array, it is not a realistic expectation to track the spatial location of an opening crack tip. However, as shown here for the situation where specific cracks are opening individually, the resolution is adequate to obtain some information on the location of each crack.

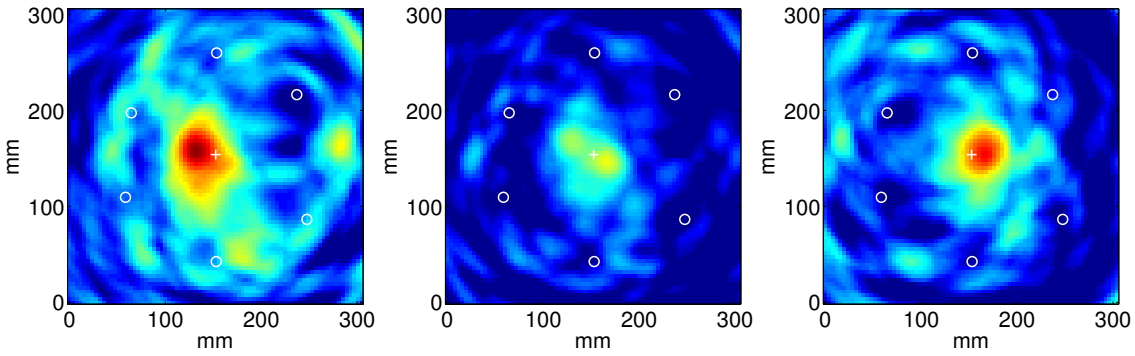

(a) 20–30% load (b) 30–40% load (c) 60–70% load

Figure 31: Load-differentia DAS images generated from data set 12. (a) 23–34.5 MPa (20–30% load), (b) 34.5–46 MPa (30–40% load), and (c) 69–80.5 MPa (60–70% load). All three images are shown on the same 10 dB color scale (−17 dB to −7 dB).

5.2.5 Features Extracted from Load-Differential Images for Automated Crack Detection

5.2.5.1 Loading effects at maximum load level

After generating the load-differential images, several features are examined for automated detection of cracks. It is assumed that as the load increases above a certain level, all fatigue cracks are fully opened. Under this assumption, the load-differential signals at the maximum load level (90% to 100%) reflect only the loading effects, not any crack opening effects. Figure 32(a) shows the load-differential signals at maximum load level for all of the 14 data sets from transducer pair 1-2 (i.e., transmitting on 1 and receiving on 2), where the direct path does not go through the cracked area and thus the signals are less affected by the cracks. Figure 32(b) shows the load-differential signals from transducer pair 2-5, where the direct path does go through the cracks and thus the signals are most affected by the cracks. It is clear in both cases that the load-differential signals at maximum load level are similar in both amplitude and shape for all data sets, and are thus likely to be minimally affected by cracks.

Evaluation of load-differential images instead of individual load-differential signals is advantageous because information from all transducer pairs is automatically incorporated. Similar to the situation for load-differential signals, it is assumed that the load-differential images generated at the maximum differential load levels are also minimally affected by cracks. The small amplitude artifacts in the images (right-most column of Figure 30) are thus assumed to be caused by load effects, which can be further confirmed by comparison to all of the images from data set 4 (fourth row of Figure 30), which correspond to the damage-free plate. The last load-differential image is used as a reference for the other images from the same data set (i.e., the same damage state) to detect fatigue crack(s).

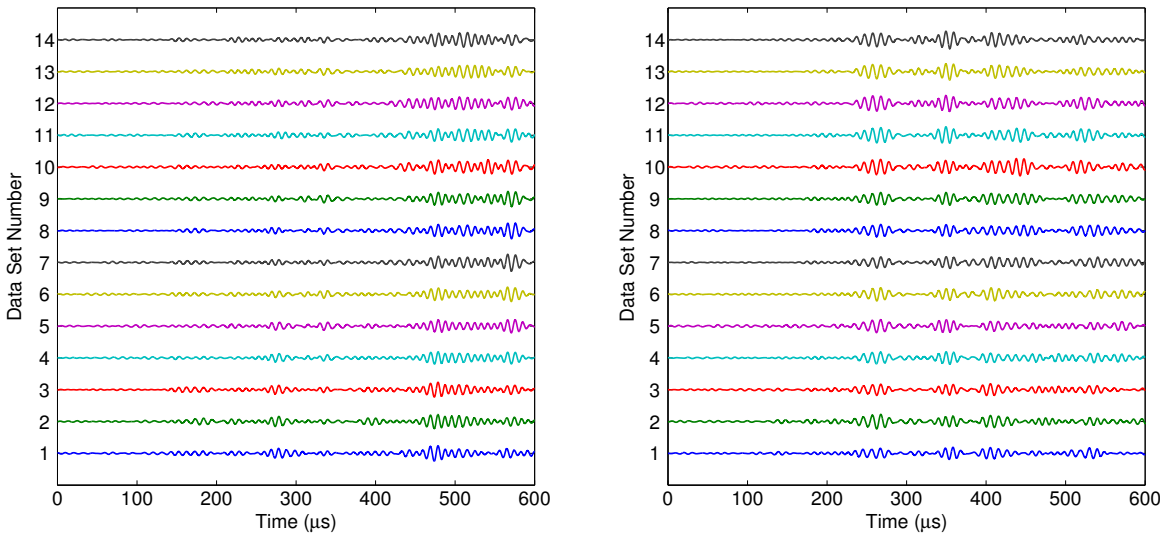

(a) Transducer pair 1–2

(b) Transducer pair 2–5

Figure 32: Load-differential signals at the maximum differential load levels (90% to 100%) for data sets 1–14 of fatigue test #1. (a) Transducer pair 1-2, and (b) transducer pair 2-5.

5.2.5.2 Total energy feature

The first feature used in this study tracks the energy of the load-differential images as cracks are opened with load. The total energy over the imaged plate area is calculated as:

$$E^k = \sum_i e_{k_i}, \tag{16}$$

where k is the kth load-differential image of each data set ($k = 1, \ldots, K$) and K is the number of differential loading cases; in our case $K = 10$. The variable e_{k_i} is the energy of the ith pixel of the kth image.

The total energy from each differential image is then normalized to that of the last load-differential image (i.e., the one at maximum differential loads):

$$E^k_{\text{norm}} = 10 \log_{10} \left(\frac{E^k}{E^K} \right), \tag{17}$$

A single value is calculated as the mean of normalized total energy for each data set:

$$\overline{E}_{\text{norm}} = \frac{\sum_k E^k_{\text{norm}}}{K}, \tag{18}$$

This feature is used to decide if fatigue cracks are present for the data set of interest.

Figure 33(a) is the plot of normalized total energy vs. differential loading for data sets 4, 8 and 12. As expected, it clearly shows that load-differential images with crack opening effects have much higher energy values than those with only loading effects. As suggested by Figure 30, if the total energy from the last-differential image of each data set is used as a threshold, all images with the crack opening effects should be detected as damaged. To further simplify the auto-detection process, the mean of the normalized total energy for each data set is plotted in a bar chart as shown in Figure 33(b). Values above 0 dB indicate existence of fatigue crack(s), and correlate well to a visual analysis.

5.2.5.3 2-D correlation coefficient feature

The next feature considered compares the pattern of each image to that of the last one, which is based upon the maximum loads. The 2-D correlation coefficient is used

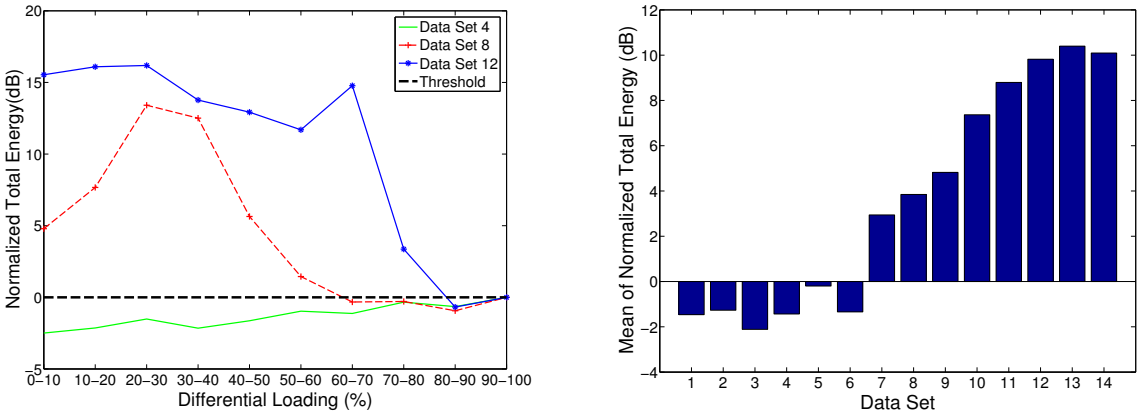

(a) Normalized total energy (b) Automated crack detection

Figure 33: Results of crack detection from the total energy feature. (a) Normalized total energy vs. differential loading for data sets 4, 8 and 12. (b) Automated crack detection from the mean of the normalized total energy.

to determine the similarity of the images [146]. In contrast to the energy feature, this method is not dependent upon the overall image intensity but tracks the changes in the pattern of the load-differential images. As Figure 30 shows, the pattern differences are obvious between the set of images that include crack opening effects and those that reflect only loading effects. Thus, the correlation coefficient between an image and the last image in the sequence for each data set is evaluated as a damage-sensitive feature. The 2-D correlation coefficient between the two images is calculated as:

$$r_k = \frac{\sum_i \left(e_{k_i} - \overline{e}_k\right)\left(e_{K_i} - \overline{e}_K\right)}{\sqrt{\sum_i \left(e_{k_i} - \overline{e}_k\right)^2}\sqrt{\sum_i \left(e_{K_i} - \overline{e}_K\right)^2}} \tag{19}$$

$$\text{where} \quad \overline{e}_k = \frac{1}{N}\sum_i e_{k_i}, \quad \overline{e}_K = \frac{1}{N}\sum_i e_{K_i}$$

and N is the number of pixels in the image.

The 2-D correlation coefficients from data sets 4, 8 and 12 are plotted in Figure 34(a). Negative coefficients indicate significant differences between image patterns, which are further evidences that these images may indicate the presence of fatigue cracks. The minimum correlation coefficient is selected for each data set and plotted in a bar chart as shown in Figure 34(b). Negative values indicate the possible existence of fatigue cracks and are in excellent agreement with visual interpretation of all images (such as are shown in Figure 30).

As shown in Figures 33(b) and 34(b), both features are shown to successfully indicate the presence of fatigue crack(s). While the energy feature shows a near-monotonic increasing trend with the number of cracks and their lengths, the 2-D correlation coefficient feature provides a more pronounced and somewhat earlier indication of the onset of cracking. Additional data from more samples is needed to further validate the efficacy of both features.

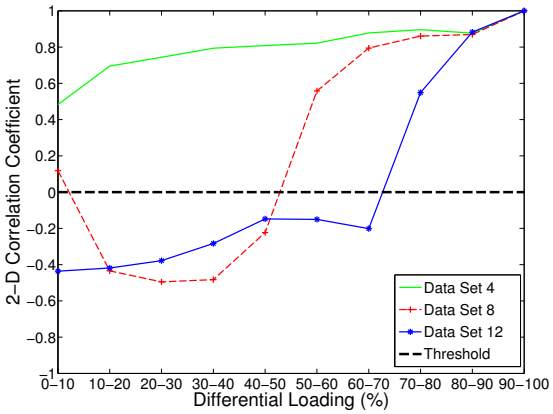

(a) 2-D correlation coefficients

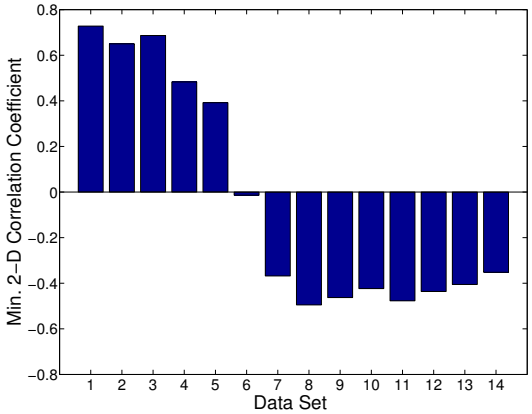

(b) Automated crack detection

Figure 34: Results of crack detection from the 2-D correlation coefficient feature. (a) 2-D correlation coefficient vs. differential loads for data sets 4, 8 and 12. (b) Automated crack detection from the minimum 2-D correlation coefficients.

5.2.6 Crack Characterization Using Load-Differential MV Imaging

The results in Section 4.2 demonstrate that using appropriate scattering information is critical to the performance of MV imaging and that the orientation curves generated from MV images for notches are shown to have characteristic signatures, which could be further used for defect discrimination. This idea is extended to the load-differential signals for the characterization of fatigue cracks in this section.

Figure 35(a) shows the scattering matrix of a 4 mm notch at an orientation of 180° emanating from a 5 mm diameter through-hole for the 3-cycle, 100 kHz A_0 mode. This matrix is actually a rotated version of Figure 19(a), which was obtained from the scattering matrix estimation method. Clearly, it demonstrates the expected highly directional scattering behavior of the notch. In contrast, Figure 35(b) shows a completely uniform scattering matrix, which describes the scattering behavior of an ideal omnidirectional scatterer.

The sparse array imaging algorithms described previously were applied to the 5.1 mm diameter through-hole data. The differenced signals used in Eq. 10 were obtained by subtracting dataset 1 (baseline) from dataset 2 (drilled hole). Figure 36(a) shows

the DAS image of the hole under zero load. The image clearly indicates the existence of the hole and its location. Figure 36(c) shows the MV image of the hole under zero load using the uniform scattering matrix. Because of its geometric symmetry, the hole is similar to an omnidirectional scatterer for the 100 kHz A_0 mode, and incorporating the assumed uniform scattering information is shown to provide an improvement in image quality. Figure 36(e) shows the MV image of the hole under zero load using the scattering matrix of a 4 mm notch at a 180° orientation (horizontal, left side of the hole). Compared to Figure 36(c), the image quality of Figure 36(e) is significantly deteriorated; not only is the amplitude at the hole location much smaller but the amplitudes of artifacts around the edges surpass that of the center hole. This comparison confirms that the hole is better detected and localized by using the uniform scattering matrix that approximately matches its actual scattering than the mismatched notch scattering matrix. Although these results are shown at zero load, they are not significantly different if other (matched) loads are used since the hole does not change significantly under load.

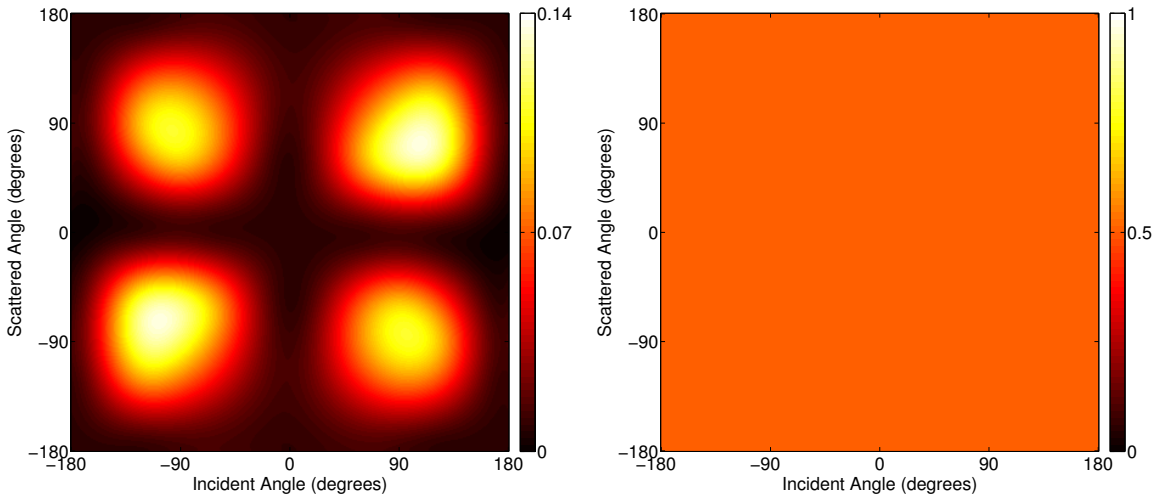

(a) 4 mm notch at 180° (b) a uniform scatterer

Figure 35: (a) An estimated scattering matrix of a 4 mm notch originate from a 5 mm diameter through-hole at a 180° orientation for the 100 kHz, 3 cycle A_0 mode. (b) A uniformly omnidirectional scatterer.

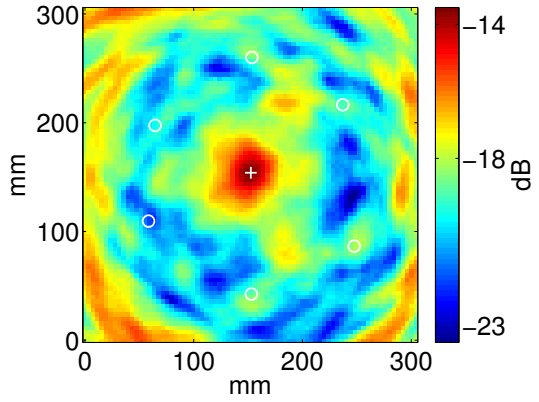

(a) DAS image of the hole

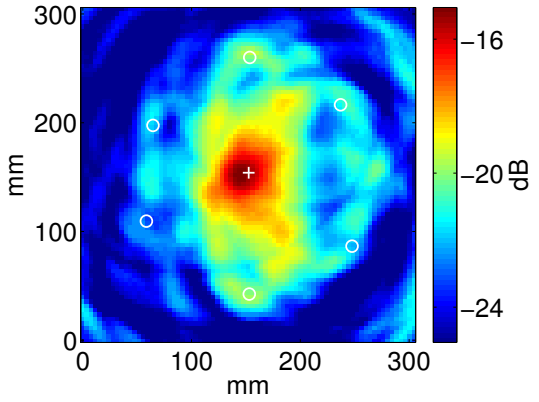

(b) load-differential DAS image of the crack

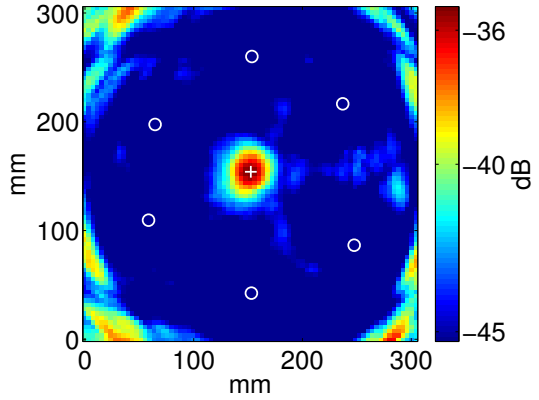

(c) MV image of the hole using the uniform scattering matrix

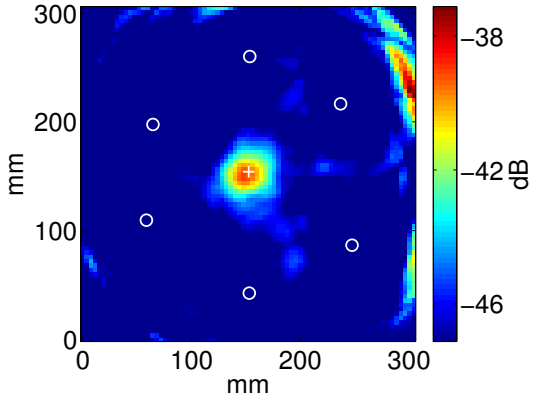

(d) load-differential MV image of the crack using the uniform scattering matrix

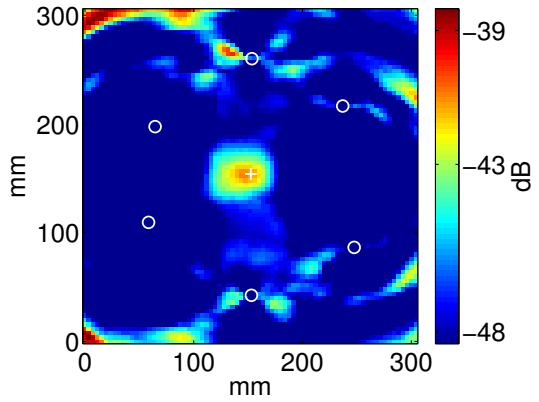

(e) MV image of the hole using the scattering matrix of a 4 mm notch

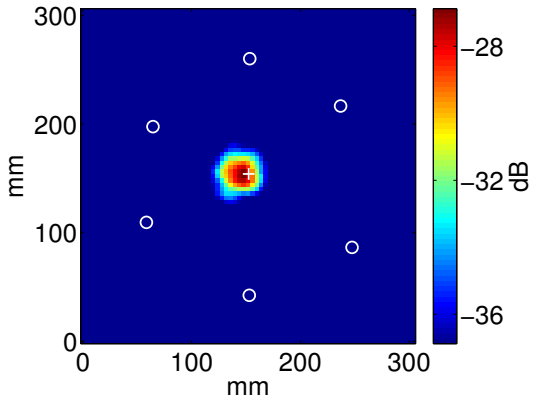

(f) load-differential MV image of the crack using the scattering matrix of a 4 mm notch

Figure 36: DAS and MV images of the 5.1 mm through-hole at zero load and the 5.4 mm crack using 30–40% load-differential signals. (a) DAS image of the hole; (b) load-differential DAS image of the crack; (c) MV image of the hole using the uniform scattering matrix; (d) load-differential MV image of the crack using the uniform scattering matrix; (e) MV image of the hole using the scattering matrix of a 4 mm notch; (f) load-differential MV image of the crack using the scattering matrix of a 4 mm notch.

Figures 36(b), 36(d), and 36(f) were generated using the 30–40% load-differential signals of dataset 7 (a single 5.4 mm crack). The load-differential DAS image of the crack is shown in Figure 36(b). By using the uniform scattering matrix, the load-differential MV image shown in Figure 36(d) is degraded compared to Figure 36(b) in terms of larger artifacts although the spot size is reduced. However, as shown in Figure 36(f), the load-differential MV image using the scattering matrix of a 4 mm horizontal notch at 180° orientation is significantly improved over the other two in terms of detection with minimal artifacts. The selection of the 180° orientation was based upon the loading direction and is a reasonable approximation of the real crack orientation, which was measured to be about 170°. A comparison of Figures 36(d) and 36(f) indicates that the scattering characteristics of the crack match those of a notch (highly directional) much better than those of an omnidirectional scatterer.

Figure 36 confirms the potential of incorporating proper scattering information for crack characterization and defect discrimination if the crack orientation is known. If the orientation information is not known, the orientation curves defined previously can be used. Figure 37(a) is the orientation curve for the hole under zero load using an 80 mm × 80 mm monitoring area centered on the hole. Although the curve is not perfectly flat, there is no obvious peak that would correspond to a scatterer orientation. This behavior is expected since the hole is approximately an omnidirectional scatterer. Figure 37(b) shows an orientation curve generated using the same monitoring area from the 30–40% loading signals of dataset 7 (a single 5.4 mm crack at 170°). Similar to the orientation curves for notches, the figure has two peaks, which clearly indicate that the crack is highly directional, and the largest peak is located at 179°, which is a reasonable estimate of the true orientation. There is a second, smaller peak at about 0°, which is approximately 180° from the main peak and is present because the scattering matrices for cracks on one side of the hole versus the other are very similar. Orientation curves with double peaks separated by about 180°

are the characteristic signatures of linear scatterers such as cracks and notches.

Figure 38 shows orientation curves of dataset 10 (two cracks, left: 13.4 mm, right: 4.7 mm) calculated from 20% load-differential MV images (i.e., 0–20%, 20–40%, 40–60%, 60–80% and 80–100%) using the same 80 mm × 80 mm monitoring area as that of Figure 37. Figure 38(a) uses the scattering matrix of a 4 mm notch, while Figure 38(b) uses that of an 8 mm notch. Both sets of plots have two dominant peaks 180° apart, which are characteristic of cracks. The larger of the two peaks for both figures is at 173° at lower loads and at −4° at higher loads (e.g., compare 0–20% curves with 60–80% curves). This shifting of the peak location with load provides an indication that there are two cracks opening at different loads; these two angles are very close to the measured crack orientations (170° for the larger left crack and −6° for the smaller right crack). The highest differential load case of 80–100% is almost zero for every angle, indicating that any cracks present are fully opened. The mean of all five load-differential curves, which are plotted with a thick gray line, can be used as a more robust feature than any individual curve to indicate crack directionality.

Another observation from Figure 38 is that the amplitude of the 0–20% curve obtained using the scattering matrix of an 8 mm notch is larger than that using the scattering matrix of a 4 mm notch. This might indicate that the degree of crack opening caused by the first 20% load is more likely close to 8 mm. However, it is not practical to use orientation curves generated with scattering matrices of different notch lengths to size fatigue cracks, since crack opening is non-linear under load. In terms of obtaining patterns that indicate the existence of cracks and estimate their orientations, at least for the data reported here, the orientation curves are relatively insensitive to the details of the assumed scattering matrices as long as they capture the directionality of the scatterer. In other words, the orientation curves are tolerant of mismatched scattering matrices to a certain extent as long as they represent a similar scatterer.

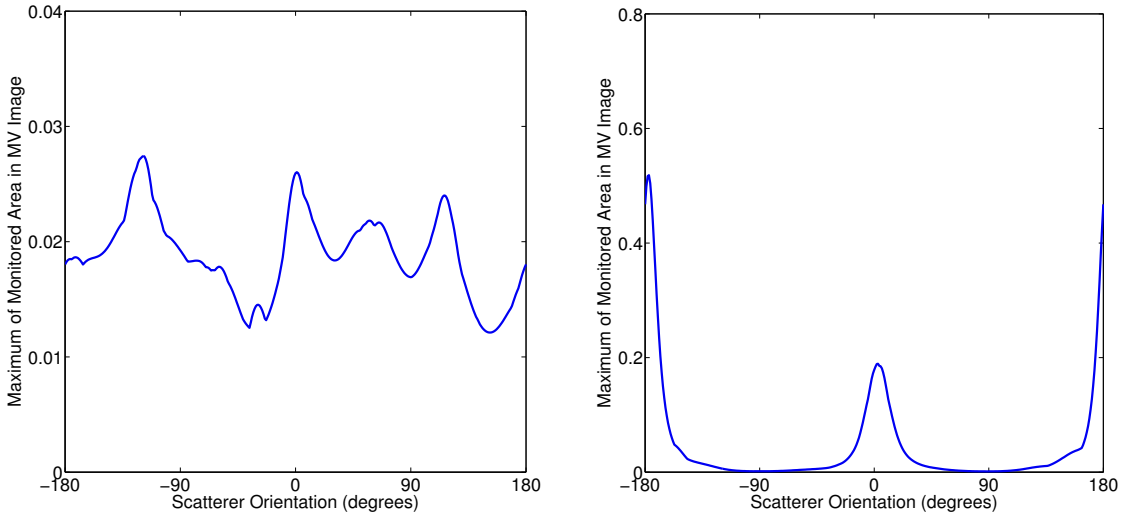

(a) the through-hole (b) the partially opened single crack

Figure 37: Orientation curves for two scatterers generated using the scattering matrix of a 4 mm notch. (a) the 5.1 mm through-hole at zero load (b) the partially opened 5.4 mm single crack under 30-40% load difference .

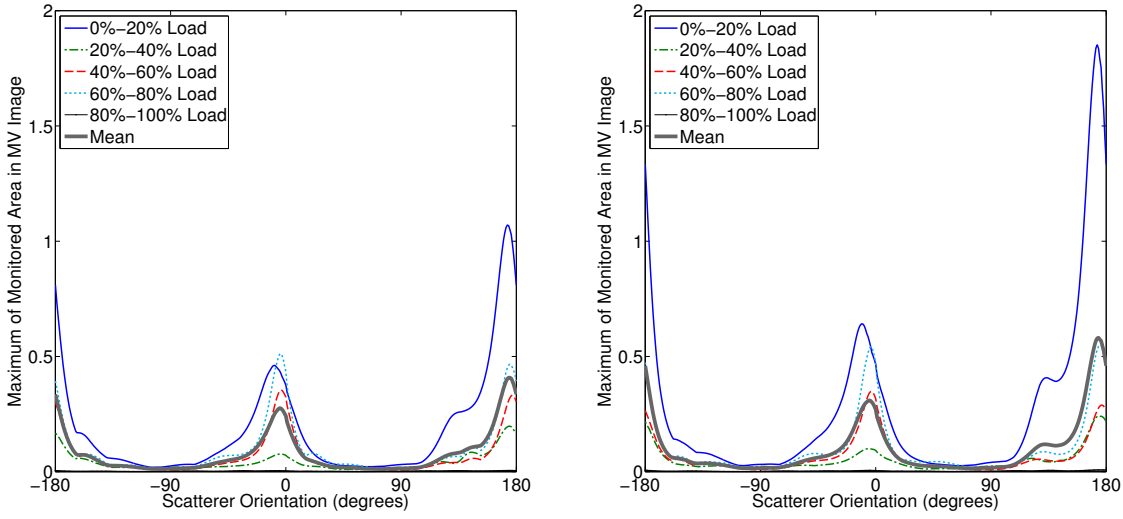

(a) using scattering matrix of a 4 mm notch (b) using scattering matrix of an 8 mm notch

Figure 38: Orientation curves for the case of two cracks generated using (a) the scattering matrix of a 4 mm notch and (b) the scattering matrix of an 8 mm notch.

5.3 Fatigue Test #1: Plate with a Bonded Doubler and Tightened Bolts

5.3.1 Experimental Setup

After the completion of fatiguing summarized in Table 2, the plate was modified by adding geometric complexities. A doubler of dimensions 305 mm × 25 mm was first bonded to the plate using epoxy, and its location is indicated by the black dashed box in Figure 39. Three holes were drilled through the doubler and the plate, and bolts were later mounted to these holes in different combinations to further reinforce the bonding. Note that the center hole is coincident with the original 5.1 mm through-hole of the plate. Recorded data sets are summarized in Table 3, and photographs of the added geometries corresponding to data sets 25, 32, and 35 are shown in the right column of Figure 39.

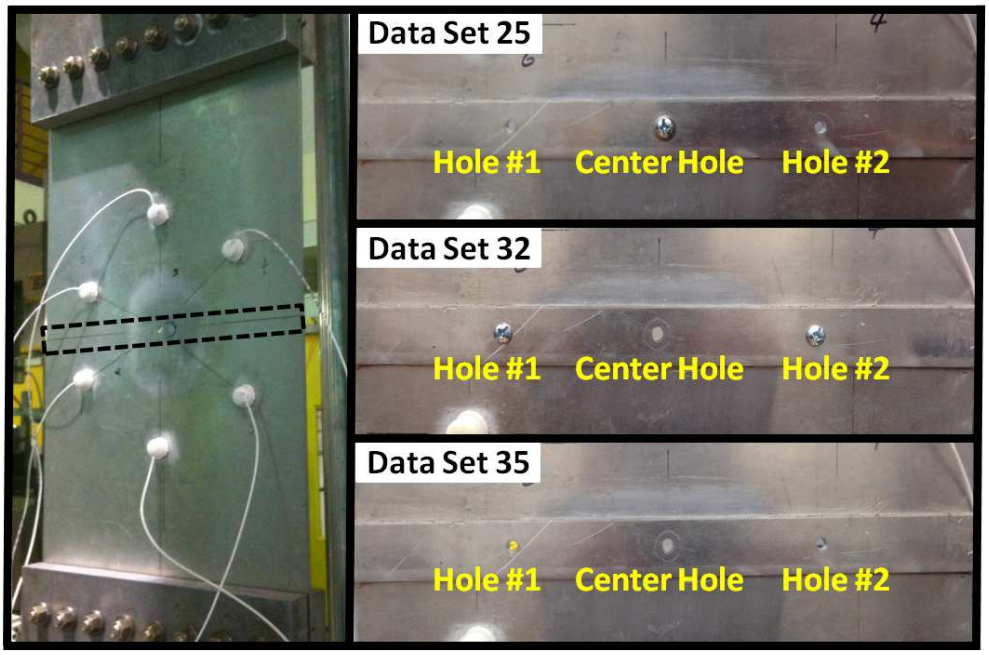

Figure 39: Aluminum plate specimen of fatigue test #1 showing the location of the installed doubler (left), and photographs of the added geometries corresponding to data sets 25, 32 and 35 (right).

Table 3: Summary of data sets acquired from fatigue test #1: added geometric complexities

Data Set(s)	Description of Additional Plate Modifications
15–18	New baselines
19–21	Added glued-on doubler
22–24	Center hole drilled through the doubler aligned with the plate center hole
25–27	A tightened bolt through the center hole
28–30	A loosened bolt through the center hole
31	Two side holes drilled, tightened bolts in all three holes
32	Tightened bolts in hole 1 and hole 2, no bolt in center hole
33	Loosened bolt in hole 1, tightened bolt in hole 2, no bolt in center hole
34	No bolt in hole 1 and hole 2, tightened bolt in center hole
35	No bolt in all three holes

5.3.2 Crack Detection Using Load-Differential DAS imaging

No additional fatiguing was performed after data set 14, so there was no additional crack growth. However, since 21 sets of load-dependent data were recorded, the plate was subjected to significant static loads that likely introduced plastic deformation. In particular, the cracks were held open under load enough times so that the degree of crack closure when the load was released likely decreased over the time of the test.

Figure 40 shows load-differential images for data sets 14 through 24. Recall that data set 14 corresponds to the final fatigue cycles, data sets 15–18 are of the unchanged specimen after fatiguing was terminated, data sets 19–21 are after a doubler was bonded to the plate, and data sets 22–24 are after a center hole was drilled through the doubler (aligned with the existing hole in the plate). There are no surprises in this figure. Data sets 15–18 have less of a load response for the lowest differential loading step, most likely because of the crack not closing to its previous degree after

the static loads of data set 14. The images from data sets 19–24, which are after bonding of the doubler, are of lower amplitude. This is not unexpected and is caused by a combination of two effects. First, the bonded doubler partially restrains the crack from responding to load changes. Such a restraint is most obviously shown in the load-differential images of data set 19, after which partial unbonding may occur such that the restraint becomes much smaller. The second effect results from the scattering of incident waves from the doubler.

Figure 41 shows load-differential images for data sets 25 through 35. The most dramatic changes can be seen in data sets 25–27 after insertion and tightening of a center bolt. This change almost entirely obscures the crack response because the tightened bolt keeps it from fully opening under load. After the bolt is loosened, in data sets 28–30, the crack response is again evident. The various bolt changes in data sets 31–34 cause similar effects. Data set 35, after all bolts are removed, again shows a larger amplitude crack response. The adhesion of the doubler around the crack site has probably become unbonded because of the multiple loading cycles. Another observation is that transducer degradation may occur after data set 31, as the energy of load-differential DAS images at the maximum load of data sets 32–35 is noticeably higher than that of the other data sets.

These results, although not completely realistic of a built-up structure, do partially indicate the potential efficacy of load-differential DAS imaging. In a real structure, it is probable that local disbonding and fastener loosening/movement would either precede or occur along with significant cracking; otherwise, it is unlikely that the local strains would be large enough for large cracks to form. The experiments with the simple plate in fatigue test #1 have not fully investigated this, but do show that successful load-differential DAS imaging can take place with a bonded doubler in place.

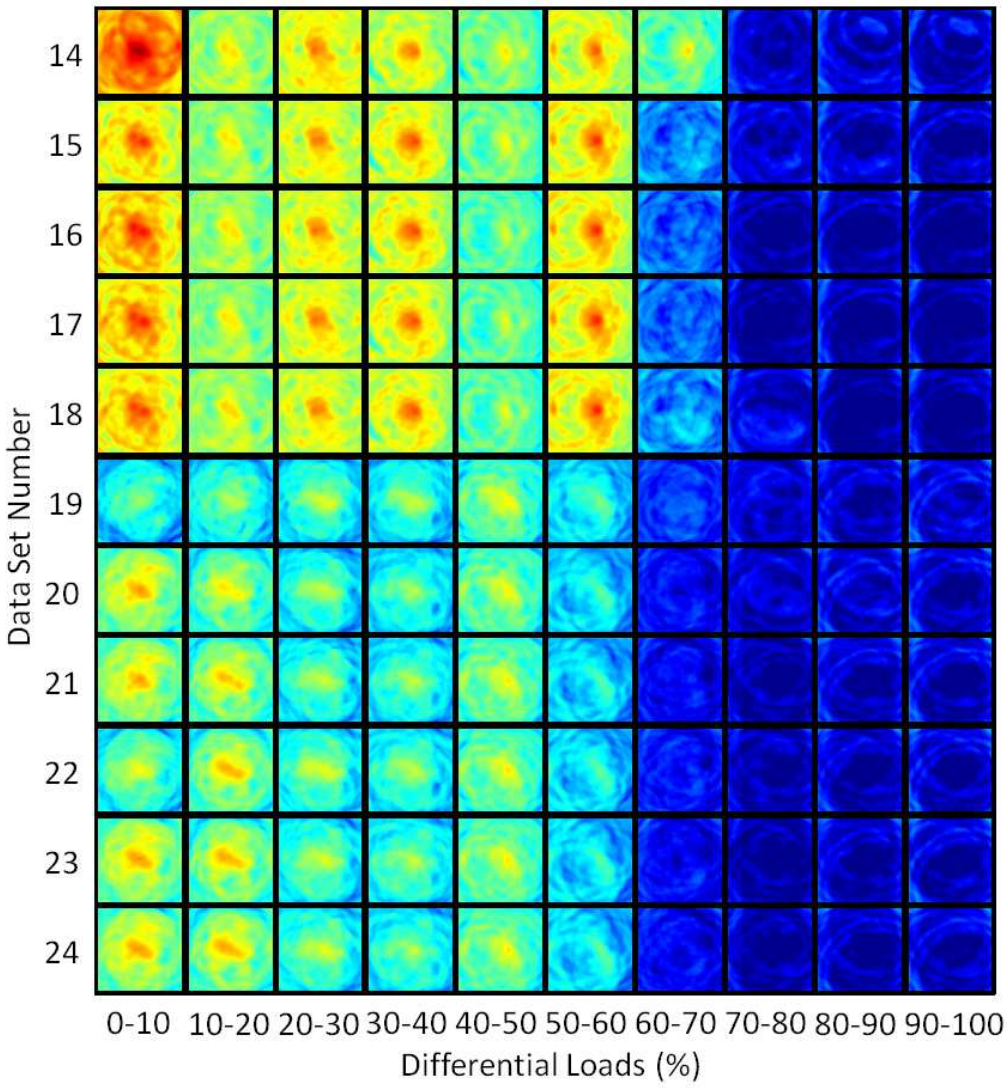

Figure 40: Load-differential DAS images from data sets 14–24 of fatigue test #1 plotted on a fixed 30 dB scale (−20 dB to 10 dB).

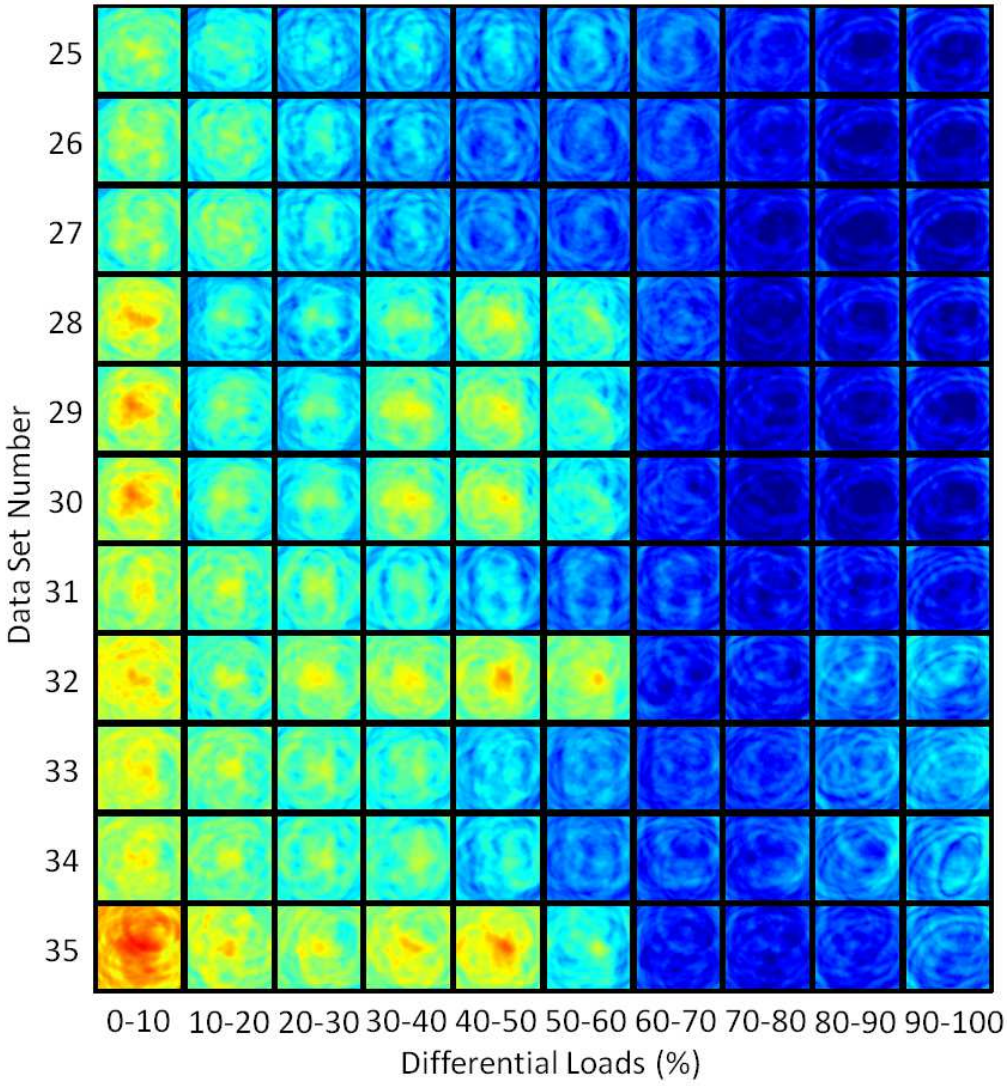

Figure 41: Load-differential DAS images from data sets 25–35 of fatigue test #1 plotted on a fixed 30 dB scale (−20 dB to 10 dB).

5.3.3 Automated Crack Detection Using Features Extracted from Load-Differential DAS Images

The previously described two features extracted from load-differential DAS images are also used here for the automated crack detection. Figure 42 shows the detection results using the total energy feature; the existence of crack(s) is successfully indicated for all data sets in spite of changes in the geometric complexities between them. The amplitude decrease of the feature after data set 18 is consistent with that of the load-differential DAS images, which shows that adding the doubler and bolts confines the crack opening. The feature values of data sets 33 and 34 are the smallest among all data sets as a result of weaker crack indications and higher background noise, which can also be observed from the load-differential images.

Figure 43 shows the detection results using the 2-D correlation coefficient feature. This feature is shown to be able to indicate the existence of crack(s) for all data sets except for data set 32. It can be seen from Figure 40 that the 90–100% load-differential image of data set 32 is much noisier than those of data sets 24–31, which may result from its highly complex geometry or transducer degradation. Although such a high energy level can also be observed in the 90–100% load-differential images of data sets 33–35, the energy centroid of the maximum load-differential image of data set 32 happens to be very close to those of the crack indication images in the same data set and such a similarity in their patterns causes the mis-detection.

The degraded performance for data sets 32 through 34 indicates the need to compensate for the high background noise or find other features that are more robust to the noise. For the two features considered here, when the detection results from them are contradictory, more information, such as that obtained from orientation curves, is needed.

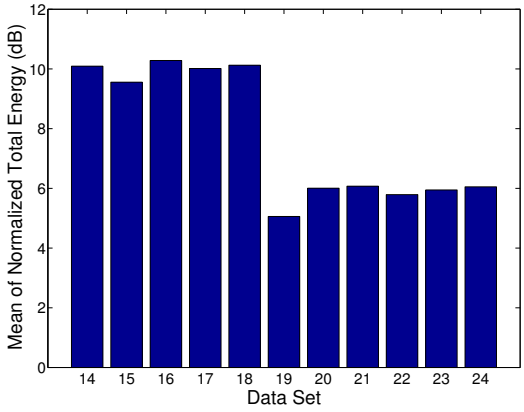

(a) Data sets 14–24 of fatigue test #1

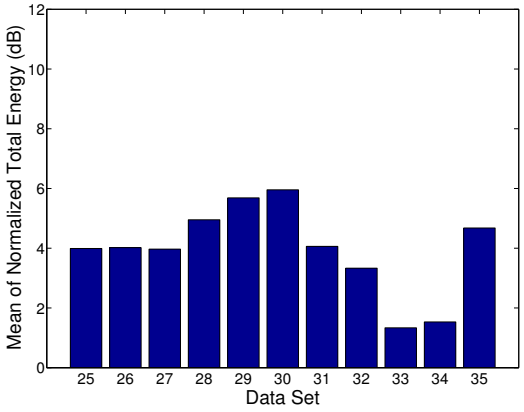

(b) Data sets 25–35 of fatigue test #1

Figure 42: Results of crack detection from the total energy feature. (a) Data sets 14–24 of fatigue test #1. (b) Data sets 25–35 of fatigue test #1.

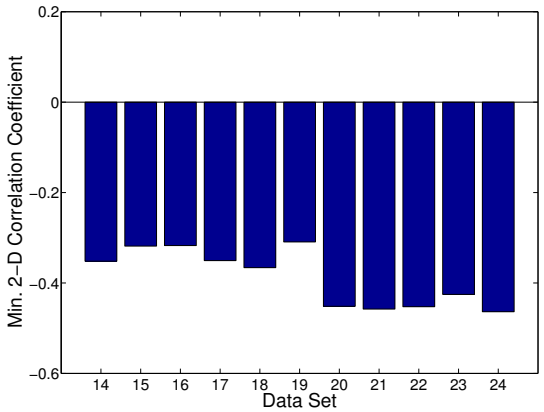

(a) Data sets 14–24 of fatigue test #1

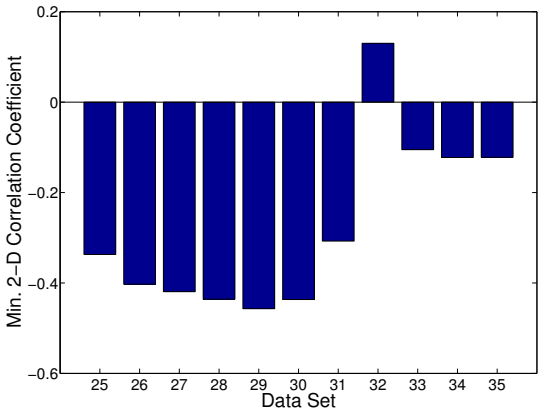

(b) Data sets 25–35 of fatigue test #1

Figure 43: Results of crack detection from the 2-D correlation coefficient feature. (a) Data sets 14–24 of fatigue test #1. (b) Data sets 25–35 of fatigue test #1.

5.3.4 Crack Characterization Using Load-Differential MV Imaging

Fatigue crack characterization is again obtained using orientation curves generated from 20% load-differential MV images. The same 80 mm × 80 mm monitoring area around the center hole and the scattering matrix of a 8 mm notch emanating from a through-hole are used for the following data sets in this section. .

Figure 44(a) shows the orientation curves from data set 18 for which the two cracks are fairly large (left: 25.2 mm; right: 18.8 mm). The 0–20% curve has two dominant peaks at the correct orientation angles, i.e., 174° vs. the measured 170° for the left crack and −6° the same as measured for the right one. Although a smaller peak appears at around 130°, it should be treated as a false alarm since no obvious peak is 180° away from it. Compared to the 0–20% curve, the four curves obtained from the other 20% load differences have much lower amplitude levels and no dominant peaks. The amplitude differences are likely caused by the large size of both cracks considered here; therefore 0–20% load opens them proportionally much more than the remaining load increments. Another observation of these curves is that the amplitudes do not approach zero in between the peaks.

The characteristic signatures of these curves do not strongly match that of curves indicating cracks. The reason could be an inappropriate selection of the predicted scattering matrix; using a scattering matrix of two notches emanating from a through-hole is expected to improve the performance because it provides a better match to the actual scatterer. Still, the mean curve provides a good indication of crack existence and a reasonable estimation of their orientations.

Figure 44(b) shows the orientation curves from data set 19 for which a doubler was installed over the existing two large cracks. Compared to those of Figure 44(a), the amplitude levels of the orientation curves here have a large drop, especially for the 0–20% curve. This observation indicates that the doubler confines the opening of cracks. As a result, the 20–40% curve, instead of having two dominant peaks, has a

third peak at around 130°, whose amplitude is comparable to that at around 170°. Similar to that of the 0–20% curve in Figure 44(a), this peak should be a false alarm due to the lack of another one at around −50°. Both the 0–20% and 40–60% curves still exhibit the peak characteristic of cracks. As a more roust feature, the mean curve provides reasonable crack indications but is less directional as compared to that of Figure 44(a).

Figure 45(a) shows the orientation curves from data set 22 for which a hole was drilled through the doubler aligned with the plate center hole. Compared to that of Figure 44(b), the 0–20% curve here has a higher amplitude level and two dominant peaks 180° apart from each other. However, the 20–40% and 40–60% curves either have multiple dominant peaks or two peaks not 180° apart. Moreover, the mean curve demonstrates even less directionality than that of Figure 44(b). These observations indicate that the hole drilling and static loading applied during taking data sets 19 through 21 may have caused possible partial disbonding of the doubler.

Figure 45(b) shows the orientation curves from data set 25 for which a bolt was installed through the center hole and tightened to reinforce the bonding of the doubler. The amplitude level changes of the 0–20% and 60–80% curves compared to those of Figure 45(a) clearly indicates that the bonding is reinforced by the tightened bolt. The 20–40% curve having the largest amplitude compared to the others confirms the bonding reinforcement effects as well. Moreover, both the 20–40% and 40–60% curves clearly shows the characteristics of cracks by having two dominant peaks 180° apart. The mean curve also exhibit the expected patterns indicating crack existence.

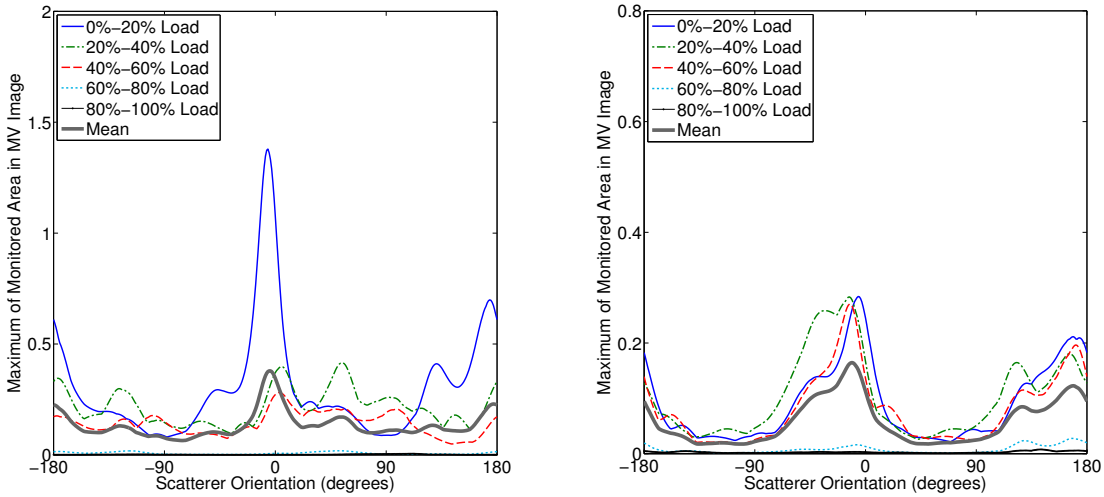

(a) Two large cracks (b) Doubler installed

Figure 44: Orientation curves for the case of two large cracks generated using the scattering matrix of an 8 mm notch. (a) Two large cracks. (b) With doubler installed.

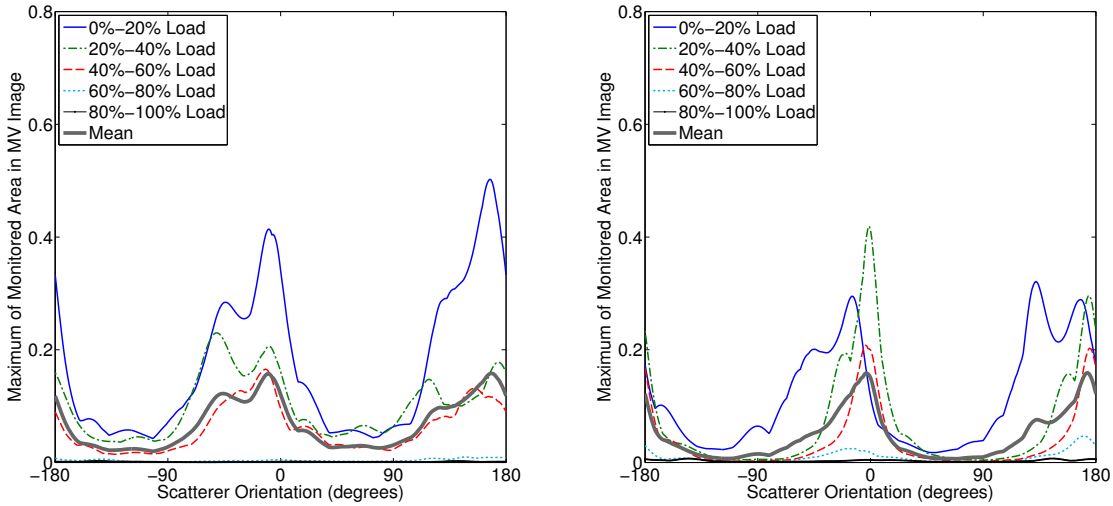

(a) Center hole drilled through doubler (b) A tightened bolt through center hole

Figure 45: Orientation curves for the case of two large cracks generated using the scattering matrix of an 8 mm notch. (a) A center hole drilled through doubler aligned with the plate center hole. (b) A tightened bolt through the center hole.

Figure 46(a) shows the orientation curves from data set 28 for which the bolt in the center hole was loosened. Without the reinforcement of the tightened bolt, the effect of partial disbonding of the doubler combines with that of the crack opening under load. As a result, the orientation curves and the mean curve no longer have clear characteristics of cracks.

Figure 46(b) shows the orientation curves from data set 31 for which two side holes were drilled and tightened bolts were installed in all three holes. The doubler was again reinforced by the three tightened bolts; therefore, the curves are able to indicate the existence of cracks and provide a good estimation of crack orientations.

Figure 47(a) shows the orientation curves from data set 32 for which only the two side holes had tightened bolts. Compared to the orientation curves of Figure 46(b), it is very likely that tightened side bolts might bend the doubler in the middle, especially given that the center bolt was missing. Such a bending has adverse effects on the bonding quality, and further deteriorates crack indication (especially for the 0–20% and 40–60% curves). The 20–40% curve and the mean are less affected in terms of their patterns. Another observation is that the 80–100% curve seems to also have crack-like characteristics, although the indicated crack orientations are incorrect. This observation matches that from the 90–100% load-differential DAS image of this data set, where the energy centroid of background noise happens to be close to the crack location. Such a crack indication can be confirmed as a false alarm since the 60–80% curve is almost flat. As mentioned previously, such an investigation can resolve the contrary results given by different features for automated crack defection.

Figure 47(b) shows the orientation curves from data set 33 for which the bolt in side hole 1 was loosened and in side hole 2 was tightened. Surprisingly, the orientation curves are very similar to those of Figure 46(b) and they clearly indicate the existence of cracks. The reason might be that the loosened bolt in side hole 1 reduces bending in the middle of the doubler and thus reinforces the bonding.

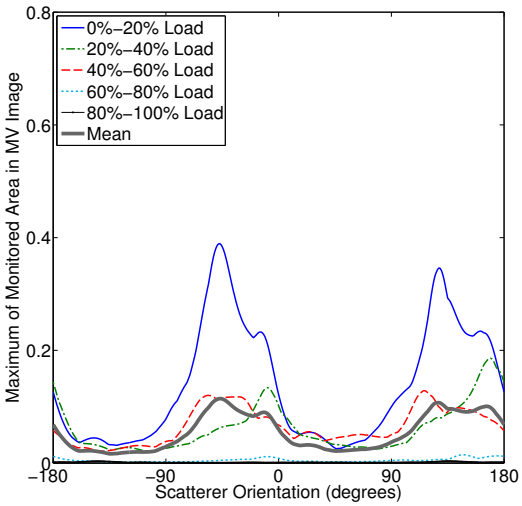

(a) A loosened bolt through center hole

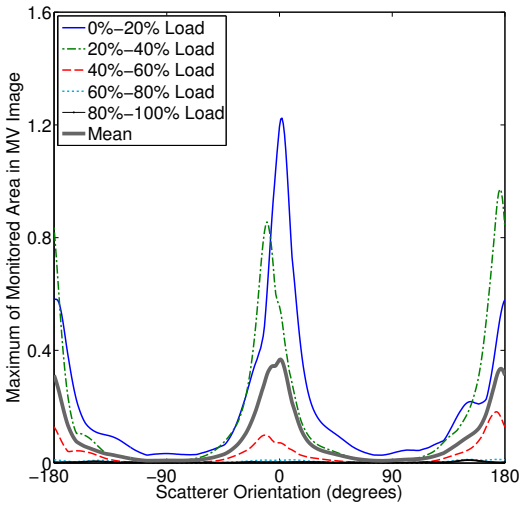

(b) Three tightened bolts

Figure 46: Orientation curves for the case of two large cracks generated using the scattering matrix of an 8 mm notch. (a) A loosened bolt through the center hole.(b) Two side holes drilled, tightened bolts in all three holes

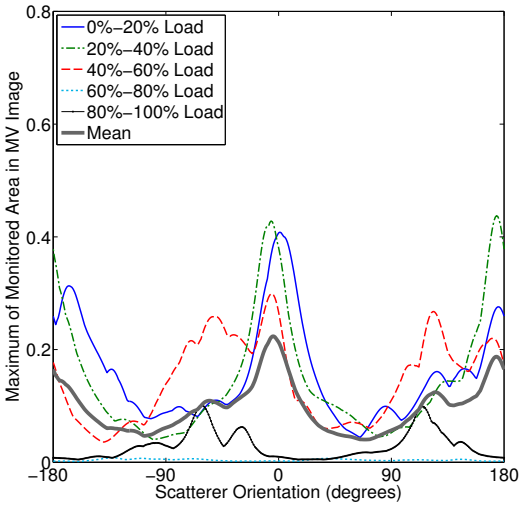

(a) Tightened bolts in two side holes

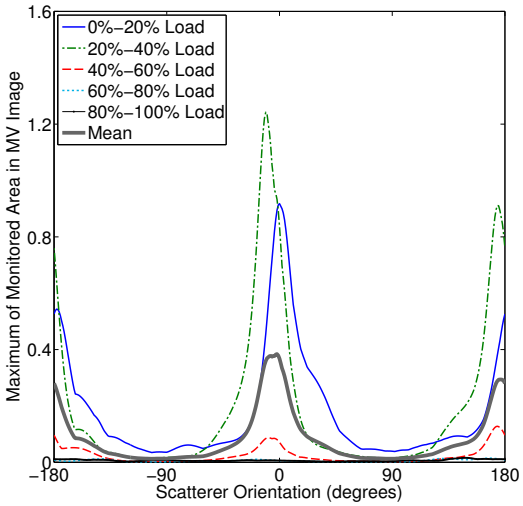

(b) Loosened bolt in hole 1 and tightened bolt in hole 2

Figure 47: Orientation curves for the case of two large cracks generated using the scattering matrix of an 8 mm notch. (a) Tightened bolts in both two side holes.(b) Loosened bolt in side hole 1 and tightened bolt in side hole 2.

Figure 48(a) shows the orientation curves from data set 34 for which only the center hole had a tightened bolt. The patterns of orientation curves are very similar to those of Figure 47(b); but the amplitudes are smaller since the tightened bolt in the center hole confines the crack opening. All in all, the orientation curves and their mean are able to indicate the existence of the fatigue cracks.

Figure 48(b) shows the orientation curves from data set 35 for which no bolts were installed. The plate geometry is very similar to that of data set 19 except for the two side holes. However, their orientation curves show some differences. The first difference is the amplitude; the curves from data set 35 have smaller values. Another difference is the pattern; the curve peaks of data set 35 are less dominant and the amplitudes between their peaks do not approach zero. These differences could be caused by the disbonding, which results from the extended static loads applied after data set 19, along with possible transducer degradation. In fact, possible transducer degradation may occur from data sets 32 through 35 as shown by the relatively higher amplitude of the 80–100% curves compared to those of data sets 19 through 31.

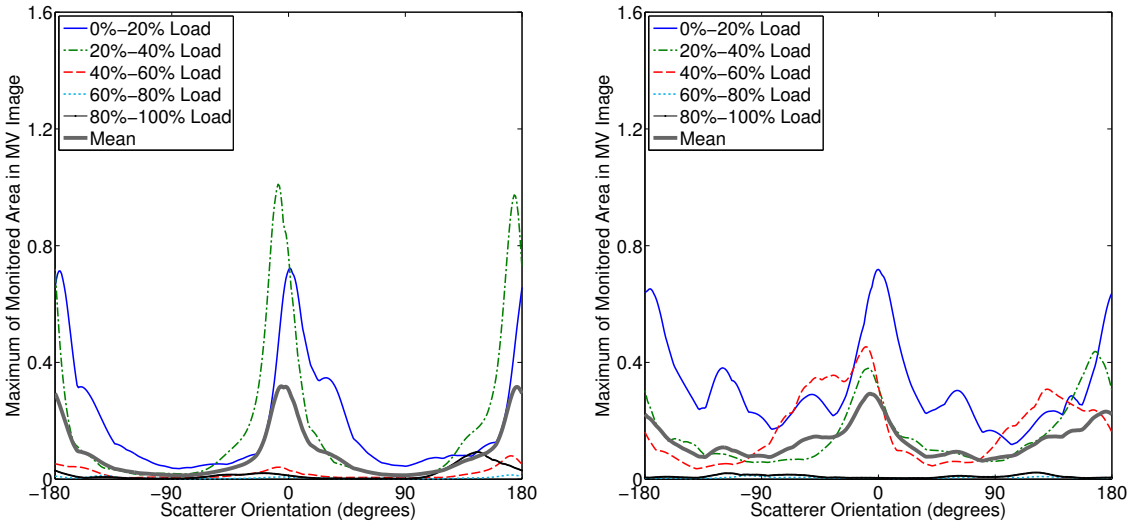

(a) Tightened bolt only in the center hole (b) No bolts in three holes

Figure 48: Orientation curves for the case of two large cracks generated using the scattering matrix of an 8 mm notch. (a) Tightened bolt only in the center hole.(b) No bolts in three holes.

5.4 Fatigue Test #2: Plate with Four Drilled Through-Holes

5.4.1 Experimental Setup

The second fatigue test used an identical aluminum plate and the same transducer array configuration as the first test. As shown in Figure 49, this plate had four initial drilled through-holes. The same fatiguing protocol was applied to the plate, and six fatigue cracks (two at hole #2, three at hole #3 and one at hole #4) were observed at the end of fatiguing. All six cracks are shown in the right column of Figure 49, where the largest one at the left side of hole #2 had a length of 12.95 mm and the smallest one at the lower left side of hole #3 had a length of 2.3 mm. Upon termination of fatiguing, the plate was insulated within a foam box with a heating pad to enable recording of load-dependent data at different temperatures. Fatigue cycles, observations of the cracks, and recorded temperatures are summarized in Table 4.

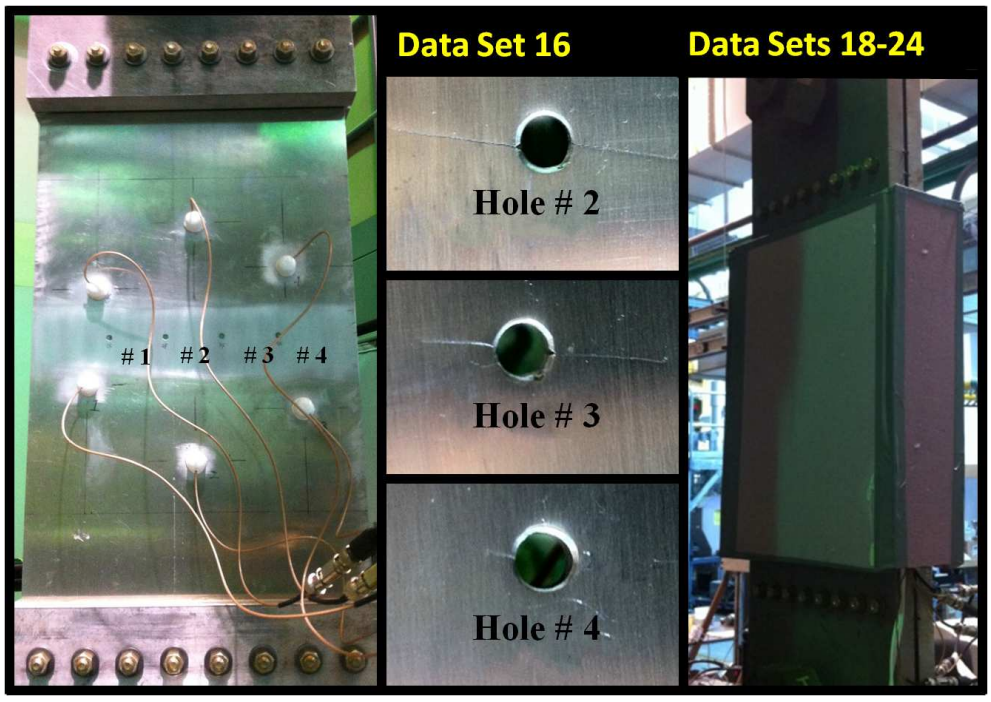

Figure 49: Aluminum plate specimen of fatigue test #2 showing four initial through-holes (left), photographs of multiple cracks at three holes of data set 16 (center), and with foam box mounted (right).

Table 4: Summary of fatiguing schedule and data acquired from fatigue test #2

Data Set	**Fatigue Cycles**	**Notes/Crack Lengths (mm)**					
		Hole 2		**Hole 3**			**Hole 4**
		Left	**Right**	**Left Up**	**Left Down**	**Right**	**Right**
1	0	Baseline, no notch					
2	0	Baseline, no notch – one bad pair					
3	0	Baseline, no notch					
4	0	Baseline, no notch					
5	0	Two starter notches					
6	2,000	0.7	----	----	----	----	----
7	2,500	1.3	----	----	----	0.6	----
8	3,000	1.7	----	----	----	1.1	----
9	3,500	2.0	----	----	----	1.5	----
10	5,500	4.1	----	----	----	3.3	----
11	6,500	4.7	1.4	----	----	4.2	----
12	7,000	5.3	2.8	----	1.4	4.7	----
13	7,500	6.3	3.6	1.6	1.6	5.4	----
14	8,500	8.2	5.4	2.3	1.9	6.8	----
15	9,500	10.3	7.9	3.9	1.9	8.8	1.1
16	10,400	13.0	10.5	7.0	1.9	11.5	2.3
17	10,400	Data recorded at finner loading steps (2%)					
18	10,400	Temperature $\sim 18.6°$					
19	10,400	Temperature $\sim 21.3°$					
20	10,400	Temperature $\sim 18.8°$					
21	10,400	Temperature $\sim 20.1°$					
22	10,400	Temperature $\sim 20.8°$					
23	10,400	Temperature $\sim 20.8°$					
24	10,400	Temperature $\sim 20.8°$					

(Orientation relative to side with transducers)

5.4.2 Crack Detection Using Load-Differential DAS imaging

The original intent of fatigue test #2 was to include multiple holes so that signals would include multiple scattering from both the holes and cracks. Notches were cut in two of the four holes (outside of the two inner holes) with the expectation that cracks would primarily grow from these two notches. However, as can be seen from Table 4, that was not the case. Crack growth was very complicated with multiple cracks growing from the two inner holes, and ultimately cracks also grew from one of the other holes.

Figure 50 shows 10% load-differential images from data sets 3 through 16, which is from the undamaged condition up through the end of fatiguing. Data sets 1 and 2 are not shown; data set 2 has one bad signal that results in two differential images with elliptical artifacts. Data set 1 does not show any loading effects, as would be expected prior to fatiguing. The background noise level in these images indicates possible transducer problems, although there are not any data sets that are clearly bad. Data set 9 is ambiguous in terms of whether load-dependent activity is caused by bad transducers versus cracking. Indication of cracking is barely seen at 50% load from the images of data set 10 and is clearly visible by data set 11. At this point there are six cracks with the largest ones about 5 mm in length (on the surface). The minimum crack length being detected is similar to that of the simple plate case of fatigue test #1, where the unambiguously detected crack length was about 4 mm. Subsequent data sets show progression of cracking combined with possible transducer degradation issues as manifested by characteristic elliptical patterns on the images. It still can be observed from these load-differential DAS images that different cracks open at different loads, especially for data set 15. However, the images cannot identify the opening for all cracks, which is not unexpected considering the large number of cracks (six).

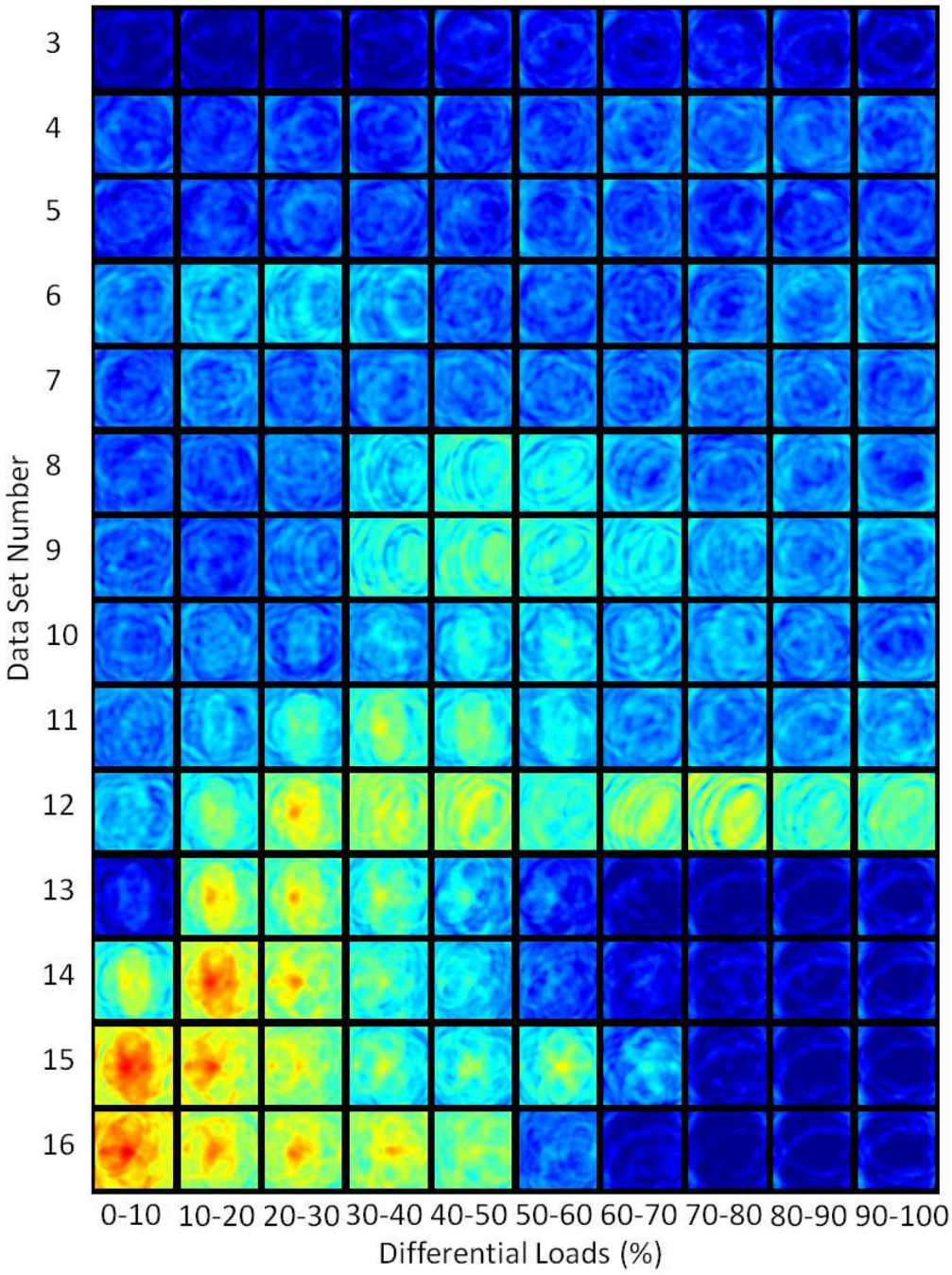

Figure 50: Load-differential DAS images from data sets 3–16 of fatigue test #2 plotted on a fixed 30 dB scale (−20 dB to 10 dB).

Figure 51 shows load-differential DAS images from data sets 16 and 18 through 25, where data set 16 is the last fatiguing data set. Data sets 18 through 25 are at nominally the same structural conditions (cracks) but were recorded at slightly different temperatures. The entire testing machine acted as a heat sink and it was not possible to raise the temperature more than about 2.5 °C. In addition, the amplitude changed by several dB between the various measurements because of an amplifier problem. It can be seen that the load-differential images for data sets 16 and 18–21 are very close to each other, illustrating that this method is inherently not dependent upon temperature. However, data sets 22–24 do show some changes, where the changes of data set 22 are most likely due to permanent deformation caused by the extended static loadings and the changes of data sets 23 and 24 are mainly caused by the amplifier gain change.

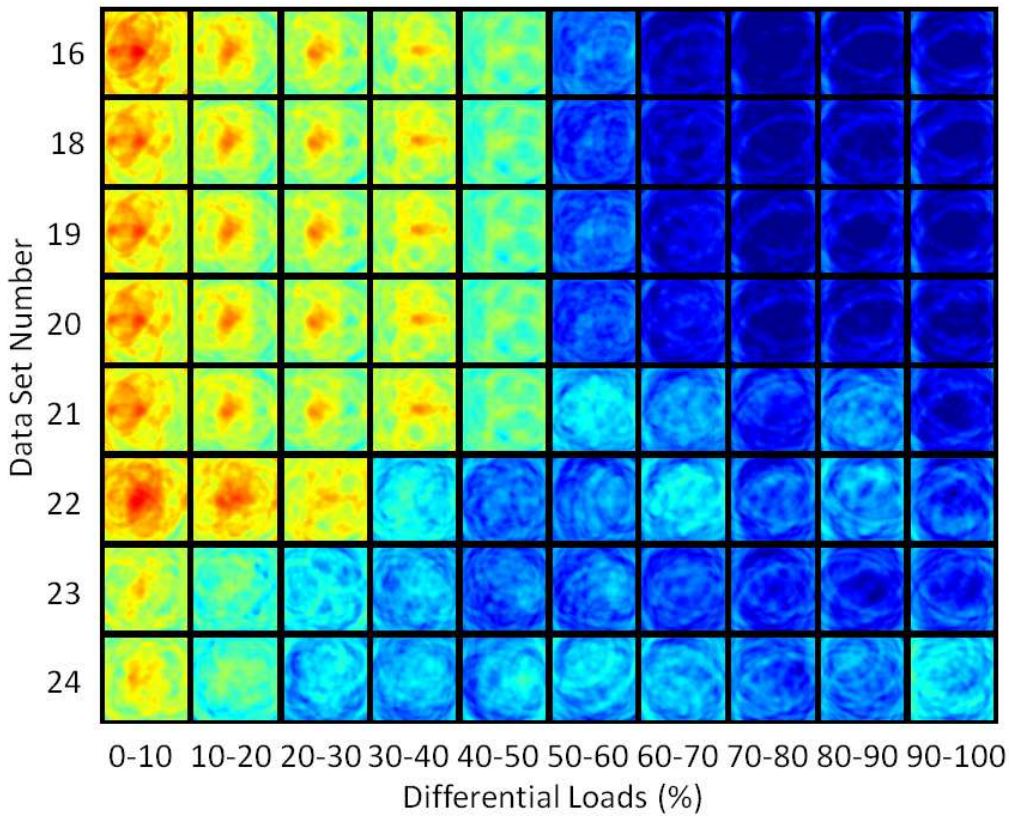

Figure 51: Load-differential DAS images from data sets 16 and 18 through 24 of fatigue test #2 plotted on a fixed 30 dB scale (−20 dB to 10 dB).

5.4.3 Automated Crack Detection Using Features Extracted from Load-Differential DAS Images

The total energy and 2-D correlation coefficient features extracted from the load-differential images of fatigue test #2 are plotted in Figure 52. Only the data sets 3 through 16 are examined since the load-differential DAS images have been shown to be independent of temperature. Both features are able to clearly indicate the existence of crack(s) from data sets 13 through 16, for which the load-differential images are clean and transducer degradation issues are minor. For data sets 9 through 12, both features still provide the correct indication in spite of the high background noise level and possible transducer problems. For data sets 4 through 8, the background noise was considerably higher such that contrary results are provided by the two features. The total energy feature detects cracks for data set 5 but not for data set 7, while the 2-D correlation coefficient feature obtains totally opposite results. To validate these results, investigations based on the orientation curves are needed. For data set 3, all load-differential DAS images are clean and both features indicate that there are no cracks.

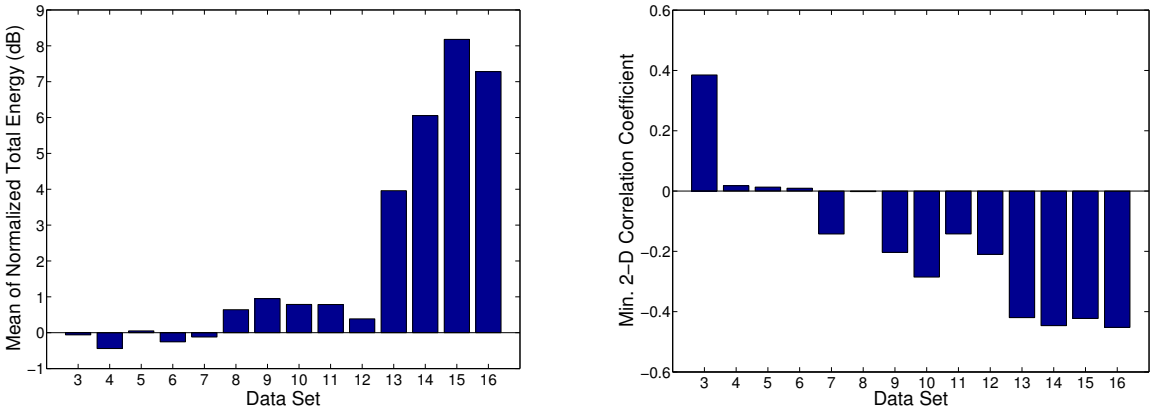

(a) Total energy feature (b) 2-D correlation feature

Figure 52: Results of automated crack detection for fatigue test #2 using the load-differential features. (a) Total energy feature. (b) 2-D correlation feature.

5.4.4 Crack Characterization Using Load-Differential MV Imaging

Figure 53 shows orientation curves from data sets 11 and 16 from fatigue test #2, which had four initial holes. The monitoring area was selected as a 232 mm × 80 mm rectangle in the center of the plate, which encompassed all four holes. Monitoring each hole separately was attempted, but the distance between them was too small to avoid interference between echoes from adjacent holes. Figure 53(a) shows the orientation curves of dataset 11 (three cracks at two holes) using the scattering matrix of a 4 mm notch, and Figure 53(b) shows the orientation curves of dataset 8 (six cracks at three holes) using the scattering matrix of an 8 mm notch. Both figures clearly indicate the existence of cracks by having dominant peaks separated by 180°, and with little additional crack opening after 60% load. Because of the uniaxial loading direction, the orientations of all the cracks are similar, that is, almost horizontal (0° or 180°), and as expected only two peaks are observed for each curve and the mean curve.

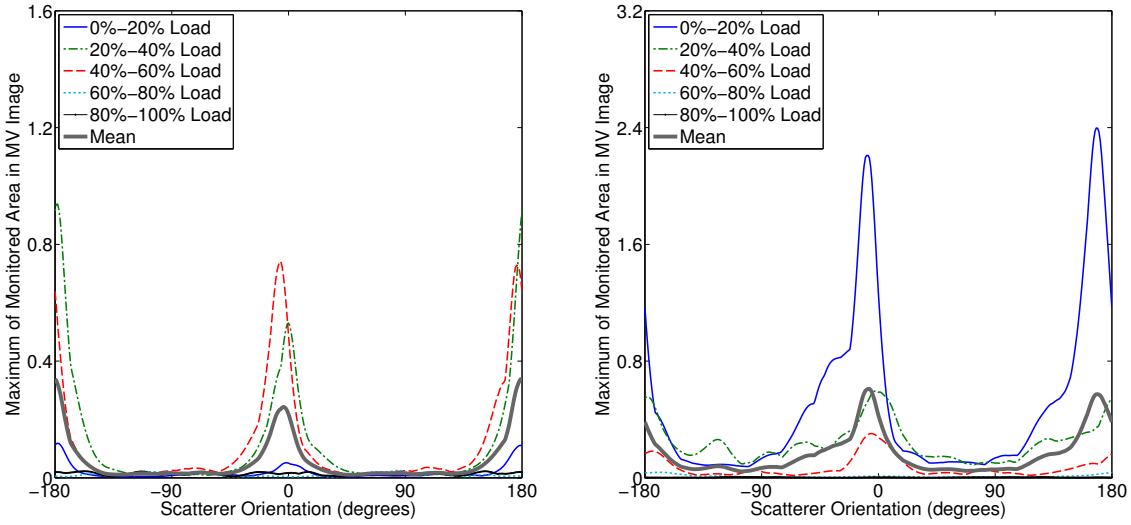

(a) Three cracks at two holes

(b) Six cracks at three holes

Figure 53: Orientation curves for the cases of four through-holes with multiple cracks. (a) Three cracks at two holes, using the scattering matrix of a 4 mm notch. (b) Six cracks at three holes, using the scattering matrix of an 8 mm notch.

Figure 54 shows orientation curves from data sets 5 and 7 of fatigue test #2; they are used to resolve the contrary crack detection results from the two load-differential features. The monitoring area was the same 232 mm × 80 mm rectangle in the center of the plate that encompassed all four holes. The orientation curves shown in Figure 54(a) do not have any patterns and their amplitude levels are very small. Such curves are typical of ones generated from the background noise signals using the scattering matrices of highly directional scatterers. The curves in Figure 54(b) are slightly different. Compared to those of Figure 54(a), each individual curve in Figure 54(b) appears to have more dominant peaks, although the amplitudes are very small as well. However, these peaks are shown within a very large span of orientation angles. The mean curve clearly indicates that there are also no cracks for this data set.

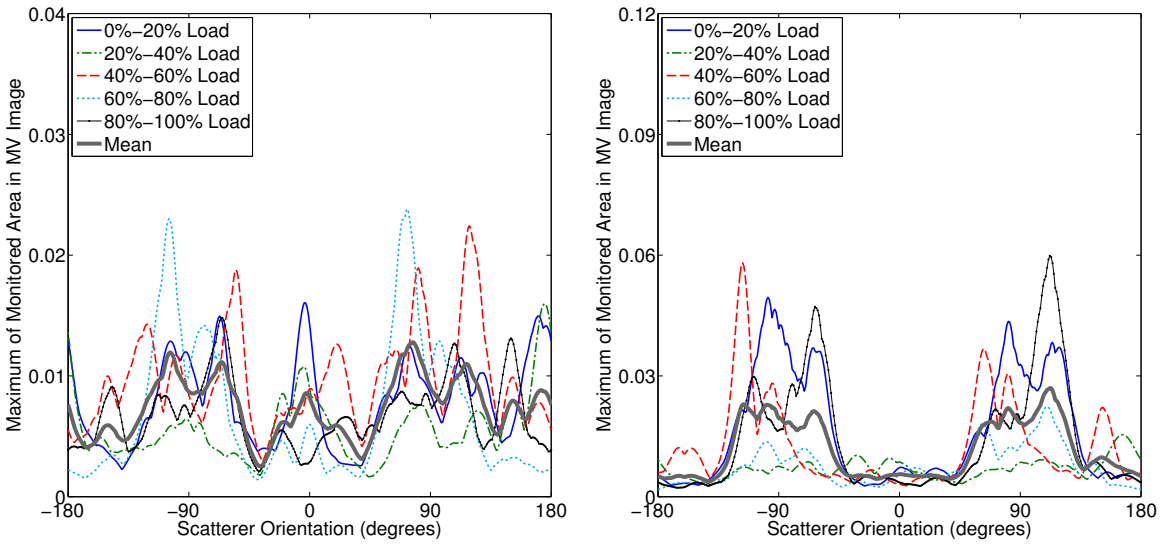

(a) Data set 5

(b) Data set 7

Figure 54: Orientation curves generated using the scattering matrix of a 4 mm notch for two data sets of fatigue test #2 (a) Data set 5. (b) Data set 7.

5.5 Fatigue Test #3: Plate with an Initially Bonded Doubler

5.5.1 Experimental Setup

The third fatigue test also used an identical aluminum plate and the same transducer array configuration as the first test. As shown in Figure 55, this plate had an initially bonded doubler. The same fatiguing protocol was applied to the plate, and it was fatigued until the largest crack was about 15 mm in length. Shortly before the test was terminated it was noticed that the doubler had become partially unbounded, at which point it was secured with bolts about 25 mm from each end. The disbonding is shown in the left part of Figure 55. Fatigue cycles and observations of the cracks are summarized in Table 5.

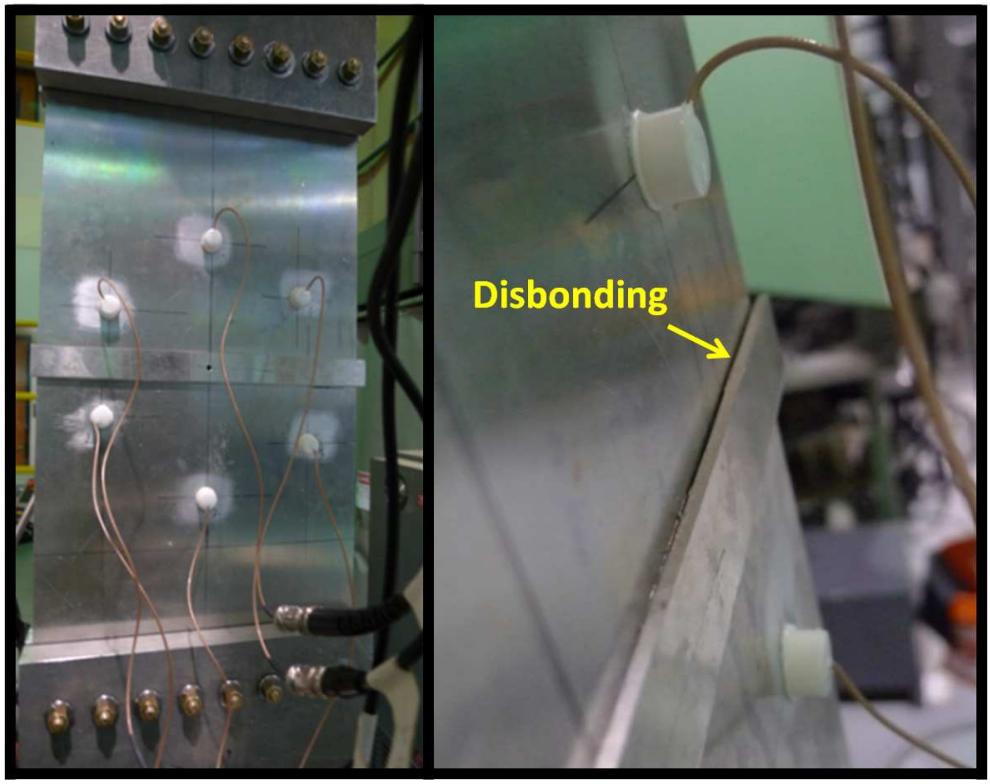

Figure 55: Aluminum plate specimen of fatigue test #3 showing four initial through-holes (left), photographs of multiple cracks at three holes of data set 16 (center), and with foam box mounted (right).

Table 5: Summary of fatiguing schedule and data acquired from fatigue test #3

Data Set	Fatigue Cycles	Crack Lengths (mm)		Data Description
		Left	Right	
1	0	----	----	Baseline with the doubler and center hole
2	0	----	----	Starter notch cut (left, front of hole)
2A	0	----	----	Data recorded at finer loading steps (2%)
3	5,000	1.5	----	Initial crack observed at the left side of center hole
4	6,500	2.6	----	
5	9,000	4.8	----	Possible transducer bonding issues at high loads
6	11,000	6.8	0.9	
7	13,000	9.1	2.7	Noticed disbond at the right edge of the doubler
8	14,000	11.5	4.6	
9	14,000	11.5	4.6	Secured doubler with bolts 25 mm from each end
10	14,000	11.5	4.6	
11	15,000	14.0	6.7	Continued fatiguing
12	15,700	15.5	8.5	

(Orientation relative to side with transducers)

5.5.2 Crack Detection Using Load-Differential DAS imaging

Figure 56 shows load differential images from all 12 data sets of fatigue test #3. The doubler was bonded to the plate prior to taking any data, and the first two data sets show some initial bonding changes in the doubler. In particular, data set 2 shows the right end of the doubler becoming partially disbonded, as can be seen from the higher amplitude indications on the right side of the image as the loads increase. This disbonding was not noticed when it occurred, so fatiguing began after data set 2 was recorded. Data sets 3 and 4 do not show any more evidence of the doubler disbonding, and the first evidence of cracking can be seen in data set 5 at high load levels. The crack continues to grow as is evidenced by the higher amplitude localization taking place at progressively lower loads. After data set 7 the disbonding of the doubler was visually observed, and after data set 8 the doubler was secured by drilling holes and installing bolts about 25 mm from either end. Fatiguing continued with data sets 11 and 12, and the installed bolts appeared to have minimal effects on the load-differential images. Fatiguing was discontinued after data set 12 when the largest crack was about 15 mm in length.

5.5.3 Automated Crack Detection Using Features Extracted from Load-Differential DAS Images

Figure 57 shows the results of automated crack detection using the features extracted from load-differential DAS images. Results from the total energy feature indicate detection for data sets 2 through 4, which are contrary to those from the 2-D correlation coefficient feature. These contrary results again indicate the limited performance of these two features when crack opening effects are not dominant in the load-differential images, such as the disbonding shown here and transducer problems shown in Figure 50. Both features indicate crack detection starting at data set 5, which is the first data set showing evidence of cracking from the load-differential images.

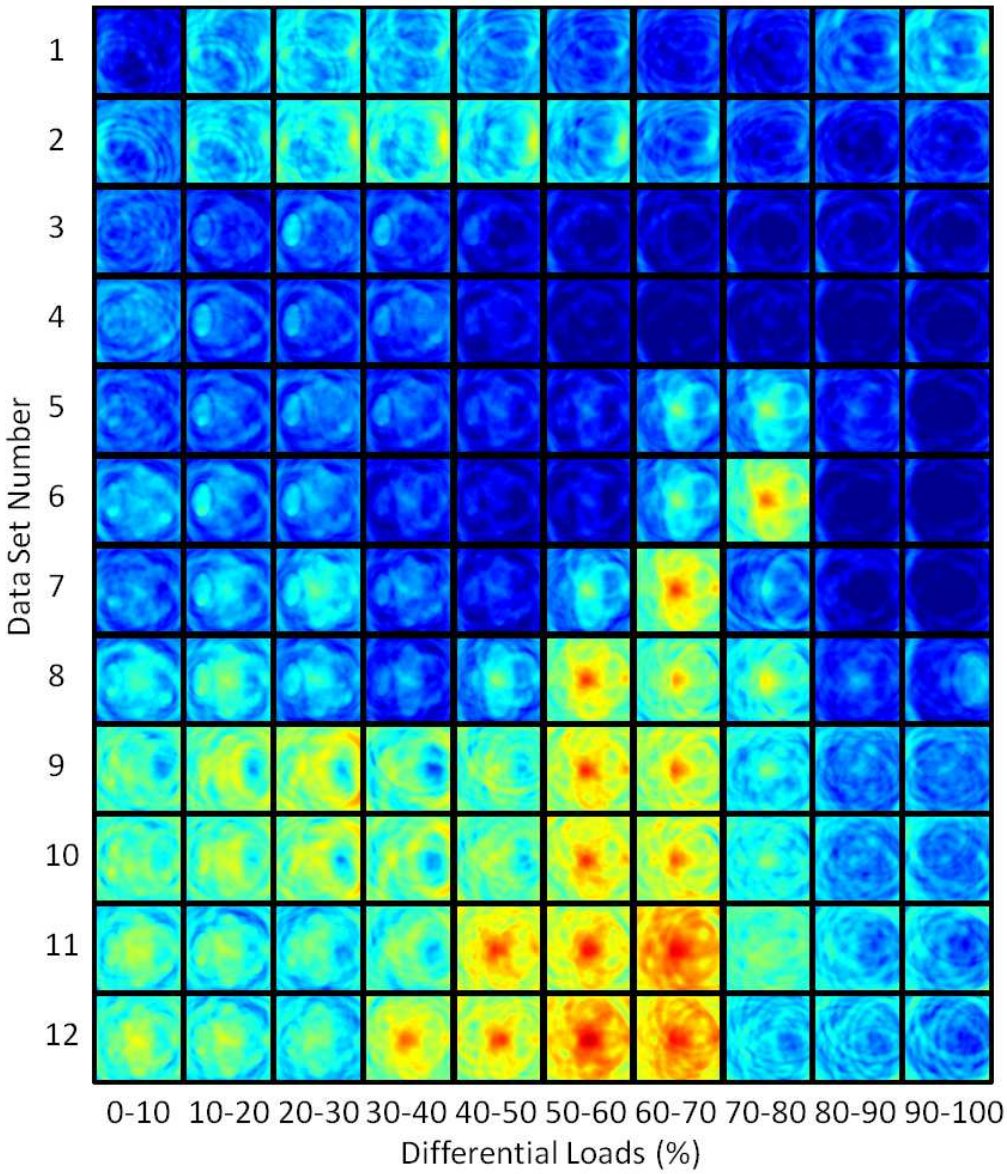

Figure 56: Load-differential DAS images from all data sets of fatigue test #3 plotted on a fixed 30 dB scale (−20 dB to 10 dB).

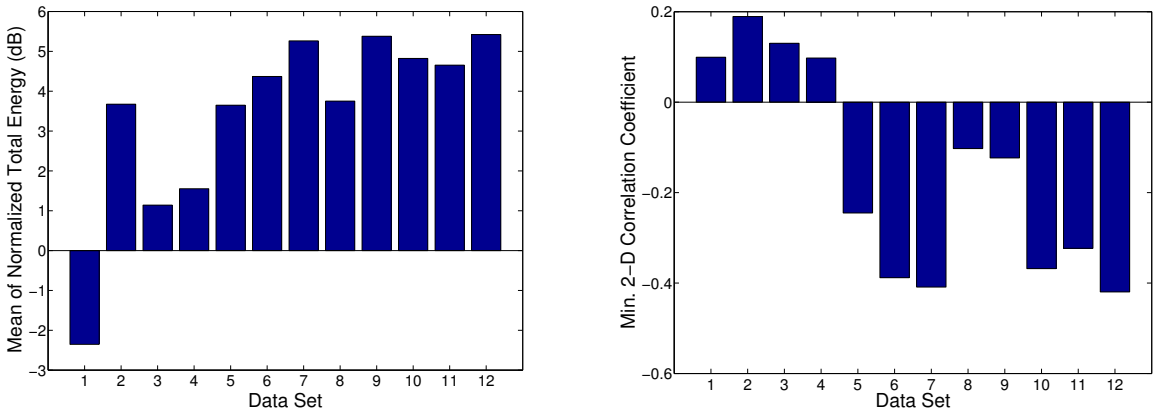

(a) Total energy feature (b) 2-D correlation feature

Figure 57: Results of automated crack detection for fatigue test #3 using the load-differential features. (a) Total energy feature. (b) 2-D correlation feature.

5.5.4 Crack Characterization Using Load-Differential MV Imaging

Two orientation curves are generated using the scattering matrix of an 8 mm notch for two types of scatterers and are shown in Figure 58 for comparison. Figure 58(a) shows the orientation curves of data set 12 (two cracks) calculated from MV images generated using 20% load differences. The curves clearly demonstrate characteristics typical of cracks. Figure 58(b) shows the orientation curves of data set 2 (a partially unbonded doubler with no crack). The monitoring area was selected as a 305 × 100 mm rectangle that contains the entire doubler. Compared to the orientation curves in Figure 58(a) that strongly indicate cracks by having two dominant peaks, the peaks in Figure 58(b) are much less dominant and the curves exhibit characteristics more typical of omnidirectional scattering. Because the disbonding occurred close to the plate edge, those peaks likely result from edge reflections that exhibit some directionality. The mean curve provides a clearer indication than the individual curves that the scattering is not highly directional. These results also confirm that the crack indications for data sets 2, as well as 3 and 4 (although not shown here), calculated using the total energy feature are false alarms.

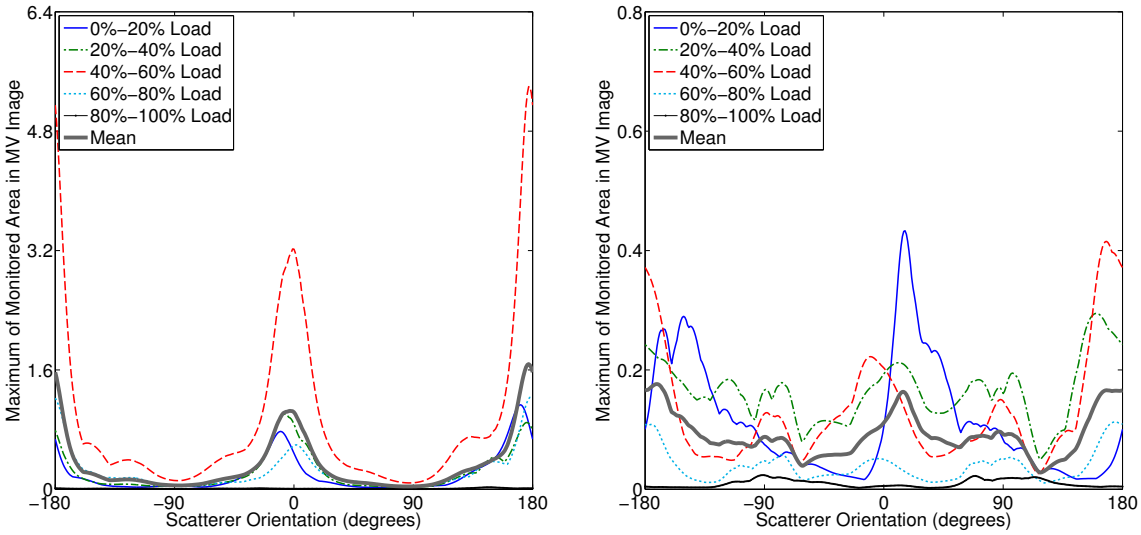

(a) Two cracks (b) Partially disbonding at plate edge

Figure 58: Orientation curves for two cases of fatigue test #3. (a) Two cracks emanating from the center hole (data set 12). (b) partially disbonding at plate edge (data set 2).

5.6 Summary

This chapter has investigated the positive and negative effects of loads on Lamb wave imaging systems that are based upon changes from damage-free reference signals. A large mismatched load causes significant changes in ultrasonic signals and can thus result in both false alarms (when there is no damage) and missed detection of damage if it is present. However, a relatively small load can open cracks to enhance their detectability. These observations have motivated the introduction and demonstration of load-differential sparse array imaging methods for fatigue crack detection, localization, and characterization for which the reference signals are taken to be at the same damage state but at different loads.

A series of DAS images generated from load-differential signals clearly shows the initiation and progression of fatigue crack growth in structures with different geometries. Furthermore, load-differential DAS imaging has the potential for identifying multiple cracks if they open at different loads. Two features of the load-differential

DAS images, the total energy and the 2-D correlation coefficient, are evaluated and are shown to be promising for automated crack detection. The results from additional experiments also confirm that the load-differential method is inherently not dependent upon temperature.

Crack characterization is obtained by using the orientation curves generated from load-differential MV images, which exhibit a characteristic signature for fatigue cracks by having peaks corresponding to the approximate crack orientation. The orientation curves generated using a highly directional scattering matrix essentially highlight scattering responses that match the directionality of the actual scatterer. Furthermore, the orientation curves generated for non-crack scatterers (a through-hole and a disbonded doubler) are shown to be substantially different from those corresponding to cracks. These results indicate that it is possible to discriminate cracks from other scatterers using permanently mounted transducers as well as determine the approximate orientation of the cracks. Although not fully investigated here, the efficacy of the proposed technique does not appear to be strongly dependent on the accuracy of the scattering matrices as long as they capture the main characteristics of discontinuities being considered, which enhances its potential applicability to a wider variety of structures with geometric complexities.

CHAPTER VI

CONCLUSIONS AND RECOMMENDATIONS

6.1 Conclusions

This research investigates the effects of loading condition changes on Lamb waves and proposes a methodology that leverages loading effects to monitor damage with Lamb waves but without a direct baseline comparison. Based upon sparse array measurements under small load changes, the load-enhanced methods were successfully demonstrated to detect fatigue cracks by their load-dependent response. In some cases localization of individual cracks was achieved. The discrimination of cracks from drilled holes and disbonds, and the approximate orientation of cracks were obtained under different plate geometric complexities. In particular, experimental results also demonstrated the importance of both stable transducers and boundary conditions during load variations, although some changes in both were fairly well tolerated. The success of the proposed methods depends upon three conditions: (1) knowledge of the load associated with each recorded signal, (2) the absence of other changes taking place during the load variations, and (3) the appropriate *a priori* information of Lamb wave scattering patterns from expected scatterers. The results of defect detection, localization, and characterization in aluminum plates with different complex geometries are shown in Chapter V.

Data recorded from fatigue tests performed as part of this research were analyzed primarily using conventional DAS imaging and adaptive MV imaging. DAS imaging not only provided a convenient way to combine data from multiple transducer pairs, it also gave confidence in the consistency of the data by providing localization information. By incorporating appropriate scattering information, MV imaging generated

orientation curves that demonstrated distinct characteristics for different scatterers, which were further used to characterize them. The performance of the two sparse array imaging methods are evaluated in both Chapters IV and V.

Scattering pattern estimation, which served as an critical steppingstone for the MV imaging method, was also a major part of this research (Chapter III). The estimation was based upon sparse array measurements such that it reduced both the time and computational requirements to a large degree compared to alternative techniques. The success of estimation relied on selecting an appropriate method for interpolating the sparse samples to obtain the scattering matrix using smooth, continuous functions. The estimation results were also compared to those obtained from a carefully designed experiment using laser wavefield scanning. In addition, the compensation algorithms used in both sparse array and laser measurements were straightforward to implement and may have a wider range of applicability for other Lamb wave SHM and NDE methods. The applications of the estimated scattering matrices are demonstrated in Chapters IV and V.

Results from this research also point out the well-known difficulty of detecting tightly closed fatigue cracks using ultrasonic methods. Many proposed SHM systems are considering permanently mounted sensors combined with ground-based instrumentation that interrogates the sensors on the ground under static conditions. The danger of this approach is that some fatigue cracks may be tightly closed under these conditions and thus undetectable. On the other hand, instantaneous measurement of dynamic loads in flight may also be problematic, as well as achieving the range of loads needed to implement a full load-differential measurement regimen. This study provides initial data to help determine if the benefits of such an approach outweigh the obstacles to implementation. It also may provide justification to change ground-based testing methods to ensure that cracks are open by application of appropriate static loads.

6.2 Recommendations for Future Work

The work performed to date has established a systematic methodology for *in situ* detection, localization, and characterization of damage using load-enhanced Lamb wave methods. However, a considerable amount of work remains if the proposed method could be robustly applied to current in-service SHM.

First, the efficacy of load-enhanced methods have been evaluated using aluminum plate specimens of one size and with several complex geometries that mimic realistic engineering components to a certain extent. More experiments considering different sizes of the interrogation structure in addition to increasing complexity should be investigated in the future work.

Second, it is beneficial to examine the efficacy of load-enhanced methods using Lamb waves of frequencies and modes other than the 100 kHz, A_0 mode. For example, the use of the S_0 mode is expected to enable the proposed methods to work under surface wetting, because its displacement is mainly in-plane and thus little leakage will occur at the surface. Another possibility is to generate load-differential images at multiple frequencies and fuse them to obtain improved performance.

Third, the basic idea of load-enhanced methods builds upon the fact that the effect of a small load difference (10% or 20%) on Lamb wave propagation is much less dominant compared to that of the appearance of defects. It is desired, however, to investigate algorithms to compensate for load differences, either small or large, and apply them for improved performance of load-enhanced methods. Such a compensation can significantly promote the applicability of the proposed methods into field practices, since load changes in operating structures can be large.

Fourth, other sparse array imaging methods, such as those based upon sparsity reconstruction and statistical approaches, could also be applied to the load-differential signals. Their results could be fused with the DAS and MV images to further improve the performance of load-enhanced methods.

Finally, more investigations should be conducted to examine additional features generated from the load-differential images for automated detection of damage. The selection of optimal thresholds for each feature is needed; this also applies to the orientation curves to obtain robust discrimination results.

REFERENCES

[1] J. E. Michaels, T. E. Michaels, S. J. Lee, X. Chen, N. Gandhi, and F. Shi, "Understanding and exploiting the effects of loading on ultrasonic sensing systems for structural health monitoring," Air Force Research Laboratory, Final Report No. AFRL-RX-WP-TR-2012-0280, February 2012.

[2] C. Boller, "Ways and options for aircraft structural health management," *Smart Materials and Structures*, vol. 10, no. 3, pp. 432–440, 2001.

[3] J. M. Brownjohn, "Structural health monitoring of civil infrastructure," *Philosophical Transactions of the Royal Society A: Mathematical, Physical and Engineering Sciences*, vol. 365, no. 1851, pp. 589–622, 2007.

[4] H. A. Kishawy and H. A. Gabbar, "Review of pipeline integrity management practices," *International Journal of Pressure Vessels and Piping*, vol. 87, no. 7, pp. 373–380, 2010.

[5] P. E. Mix, *Introduction to Nondestructive Testing: A Training Guide*. Wiley-Interscience, 2005.

[6] P. J. Shull, *Nondestructive Evaluation: Theory, Techniques, and Applications*. CRC, 2002.

[7] D. Balageas, C.-P. Fritzen, and A. Güemes, *Structural Health Monitoring*. Wiley Online Library, 2006.

[8] C. R. Farrar and K. Worden, "An introduction to structural health monitoring," *Philosophical Transactions of the Royal Society A: Mathematical, Physical and Engineering Sciences*, vol. 365, no. 1851, pp. 303–315, 2007.

[9] H. Lamb, "On waves in an elastic plate," *Proceedings of the Royal Society of London. Series A*, vol. 93, no. 648, pp. 114–128, 1917.

[10] I. A. Viktorov, *Rayleigh and Lamb Waves: Physical Theory and Applications*. New York: Plenum Press, 1967.

[11] J. E. Michaels and T. E. Michaels, "Guided wave signal processing and image fusion for *in situ* damage localization in plates," *Wave Motion*, vol. 44, no. 6, pp. 482–492, 2007.

[12] J. S. Hall and J. E. Michaels, "Minimum variance ultrasonic imaging applied to an *in situ* sparse guided wave array," *IEEE Transactions on Ultrasonics, Ferroelectrics, and Frequency Control*, vol. 57, no. 10, pp. 2311–2323, 2010.

[13] F. Yan, R. L. Royer, and J. L. Rose, "Ultrasonic guided wave imaging techniques in structural health monitoring," *Journal of Intelligent Material Systems and Structures*, vol. 21, no. 3, pp. 377–384, 2010.

[14] R. M. Levine and J. E. Michaels, "Model-based imaging of damage with Lamb waves via sparse reconstruction," *Journal of the Acoustical Society of America*, vol. 133, no. 3, pp. 1525–1534, 2013.

[15] J. S. Hall, P. Fromme, and J. E. Michaels, "Guided wave damage characterization via minimum variance imaging with a distributed array of ultrasonic sensors," *Journal of Nondestructive Evaluation*, vol. 33, no. 3, pp. 299–308, 2014.

[16] A. J. Croxford, P. D. Wilcox, B. W. Drinkwater, and G. Konstantinidis, "Strategies for guided-wave structural health monitoring," *Proceedings of the Royal Society A: Mathematical, Physical and Engineering Science*, vol. 463, no. 2087, pp. 2961–2981, 2007.

[17] A. Raghavan and C. E. Cesnik, "Review of guided-wave structural health monitoring," *Shock and Vibration Digest*, vol. 39, no. 2, pp. 91–116, 2007.

[18] J. E. Michaels, "Detection, localization and characterization of damage in plates with an *in situ* array of spatially distributed ultrasonic sensors," *Smart Materials and Structures*, vol. 17, no. 3, p. 035035, 2008.

[19] X. Chen, J. E. Michaels, and T. E. Michaels, "A methodology for estimating guided wave scattering patterns from sparse transducer array measurements," *IEEE Transactions on Ultrasonics, Ferroelectrics, and Frequency Control*, vol. 62, no. 1, pp. 208–219, 2015.

[20] X. Chen, J. E. Michaels, and T. E. Michaels, "Estimation of guided wave scattering matrices from spatially distributed transducer arrays," in *AIP Conference Proceedings-American Institute of Physics*, vol. 1511, pp. 636–643, 2013.

[21] X. Chen, J. E. Michaels, and T. E. Michaels, "Design of distributed sparse arrays for Lamb wave SHM based upon estimated scattering matrices," in *AIP Conference Proceedings-American Institute of Physics*, vol. 1581, pp. 248–255, 2014.

[22] J. E. Michaels, X. Chen, and T. E. Michaels, "Scattering measurements and *in situ* imaging with sparse guided wave arrays," in *Proceedings of the 9th IWSHM*, pp. 2177–2184, 2013.

[23] X. Chen, J. E. Michaels, S. J. Lee, and T. E. Michaels, "Load-differential imaging for detection and localization of fatigue cracks using Lamb waves," *NDT & E International*, vol. 51, pp. 142–149, 2012.

[24] X. Chen, S. J. Lee, J. E. Michaels, and T. E. Michaels, "Load-differential features for automated detection of fatigue cracks using guided waves," in *AIP Conference Proceedings-American Institute of Physics*, vol. 1430, pp. 2021–2028, 2012.

[25] X. Chen, J. E. Michaels, and T. E. Michaels, "Load-enhanced Lamb wave techniques for characterization of scatterers in structures with complex geometries," *Materials Evaluation*, vol. 72, no. 10, pp. 1314–1324, 2014.

[26] J. Michaels, S. Lee, X. Chen, and T. Michaels, "Load-enhanced imaging of fatigue cracks via sparse guided wave arrays," in *Proceedings of the 8th IWSHM*, pp. 1150–1157, 2011.

[27] S. J. Lee, J. E. Michaels, X. Chen, and T. E. Michaels, "Fatigue crack monitoring via load-differential guided wave methods," in *AIP Conference Proceedings-American Institute of Physics*, vol. 1430, pp. 1575–1582, 2012.

[28] J. W. Strutt, "On waves propagated along the plane surface of an elastic solid," *Proceedings of the London Mathematical Society*, vol. 1, no. 1, pp. 4–11, 1885.

[29] A. E. H. Love, *Some Problems of Geodynamics: Being an Essay to which the Adams Prize in the University of Cambridge was Adjudged in 1911.* CUP Archive, 1967.

[30] R. Stoneley, "Elastic waves at the surface of separation of two solids," *Proceedings of the Royal Society of London. Series A, Containing Papers of a Mathematical and Physical Character*, vol. 106, no. 738, pp. 416–428, 1924.

[31] J. D. Achenbach, *Wave Propagation in Elastic Solids.* North-Holland Amsterdam, 1973.

[32] V. Giurgiutiu, "Tuned Lamb wave excitation and detection with piezoelectric wafer active sensors for structural health monitoring," *Journal of Intelligent Material Systems and Structures*, vol. 16, no. 4, pp. 291–305, 2005.

[33] P. Wilcox, M. Lowe, and P. Cawley, "The effect of dispersion on long-range inspection using ultrasonic guided waves," *NDT & E International*, vol. 34, no. 1, pp. 1–9, 2001.

[34] D. N. Alleyne and P. Cawley, "Optimization of Lamb wave inspection techniques," *NDT & E International*, vol. 25, no. 1, pp. 11–22, 1992.

[35] J. E. Michaels, S. J. Lee, A. J. Croxford, and P. D. Wilcox, "Chirp excitation of ultrasonic guided waves," *Ultrasonics*, vol. 53, no. 1, pp. 265–270, 2013.

[36] J. Krautkramer and H. Krautkramer, *Ultrasonic Testing of Materials*. Springer-Verlag, 1990.

[37] A. A. Pollock, "Classical wave theory in practical AE testing," *Progress in Acoustic Emission III. Tokyo, Japan*, pp. 21–24, 1986.

[38] R. S. C. Monkhouse, P. D. Wilcox, and P. Cawley, "Flexible interdigital PVDF transducers for the generation of Lamb waves in structures," *Ultrasonics*, vol. 35, no. 7, pp. 489–498, 1997.

[39] P. D. Wilcox, "Omni-directional guided wave transducer arrays for the rapid inspection of large areas of plate structures," *IEEE Transactions on Ultrasonics, Ferroelectrics, and Frequency Control*, vol. 50, no. 6, pp. 699–709, 2003.

[40] P. Fromme, P. D. Wilcox, M. J. Lowe, and P. Cawley, "On the development and testing of a guided ultrasonic wave array for structural integrity monitoring," *IEEE Transactions on Ultrasonics, Ferroelectrics, and Frequency Control*, vol. 53, no. 4, pp. 777–785, 2006.

[41] L. Yu and V. Giurgiutiu, "In situ 2-D piezoelectric wafer active sensors arrays for guided wave damage detection," *Ultrasonics*, vol. 48, no. 2, pp. 117–134, 2008.

[42] C. H. Wang, J. T. Rose, and F.-K. Chang, "A synthetic time-reversal imaging method for structural health monitoring," *Smart Materials and Structures*, vol. 13, no. 2, p. 415, 2004.

[43] T. Clarke, P. Cawley, P. D. Wilcox, and A. J. Croxford, "Evaluation of the damage detection capability of a sparse-array guided-wave SHM system applied to a complex structure under varying thermal conditions," *IEEE Transactions on Ultrasonics, Ferroelectrics, and Frequency Control*, vol. 56, no. 12, pp. 2666–2678, 2009.

[44] P. Fromme, "Influence of guided ultrasonic wave scattering directionality on the detection sensitivity for SHM of fatigue cracks," in *Proceedings of the SPIE*, vol. 7650, pp. 76501M1–76501M10, 2010.

[45] A. Croxford, P. Wilcox, and B. Drinkwater, "Quantification of SHM sensor array performance," in *AIP Conference Proceedings-American Institute of Physics*, vol. 1096, pp. 942–949, 2009.

[46] J. S. Hall, J. E. Michaels, D. O. Thompson, and D. E. Chimenti, "Analysis of distributed sparse array configurations for guided wave imaging applications," in *AIP Conference Proceedings-American Institute of Physics*, vol. 1335, pp. 859–866, 2011.

[47] P. D. Wilcox, M. J. Lowe, and P. Cawley, "The excitation and detection of Lamb waves with planar coil electromagnetic acoustic transducers," *IEEE Transactions on Ultrasonics, Ferroelectrics, and Frequency Control*, vol. 52, no. 12, pp. 2370–2383, 2005.

[48] M. Castaings and P. Cawley, "The generation, propagation, and detection of Lamb waves in plates using air-coupled ultrasonic transducers," *Journal of the Acoustical Society of America*, vol. 100, no. 5, pp. 3070–3077, 1996.

[49] S. Pierce, B. Culshaw, W. Philp, F. Lecuyer, and R. Farlow, "Broadband Lamb wave measurements in aluminium and carbon/glass fibre reinforced composite materials using non-contacting laser generation and detection," *Ultrasonics*, vol. 35, no. 2, pp. 105–114, 1997.

[50] W. Leong, W. Staszewski, B. Lee, and F. Scarpa, "Structural health monitoring using scanning laser vibrometry: III. Lamb waves for fatigue crack detection," *Smart Materials and Structures*, vol. 14, no. 6, pp. 1387–1395, 2005.

[51] W. Staszewski, B. Lee, and R. Traynor, "Fatigue crack detection in metallic structures with Lamb waves and 3D laser vibrometry," *Measurement Science and Technology*, vol. 18, no. 3, pp. 727–739, 2007.

[52] J. L. Rose, *Ultrasonic Waves in Solid Media*. Cambridge University Press, 2004.

[53] P. Fromme and C. Rouge, "Directivity of guided ultrasonic wave scattering at notches and cracks," in *Journal of Physics: Conference Series*, vol. 269, pp. 01201801–01201811, 2011.

[54] T. Grahn, "Lamb wave scattering from a circular partly through-thickness hole in a plate," *Wave Motion*, vol. 37, no. 1, pp. 63–80, 2003.

[55] J. Zhang, B. W. Drinkwater, and P. D. Wilcox, "Defect characterization using an ultrasonic array to measure the scattering coefficient matrix," *IEEE Transactions on Ultrasonics, Ferroelectrics, and Frequency Control*, vol. 55, no. 10, pp. 2254–2265, 2008.

[56] P. Fromme and M. B. Sayir, "Measurement of the scattering of a Lamb wave by a through hole in a plate," *Journal of the Acoustical Society of America*, vol. 111, no. 3, pp. 1165–1170, 2002.

[57] O. Diligent, T. Grahn, A. Boström, P. Cawley, and M. J. Lowe, "The low-frequency reflection and scattering of the S_0 Lamb mode from a circular through-thickness hole in a plate: Finite element, analytical and experimental studies," *Journal of the Acoustical Society of America*, vol. 112, no. 6, pp. 2589–2601, 2002.

[58] J. McKeon and M. Hinders, "Lamb wave scattering from a through hole," *Journal of Sound and Vibration*, vol. 224, no. 5, pp. 843–862, 1999.

[59] D. N. Alleyne and P. Cawley, "The interaction of Lamb waves with defects," *IEEE Transactions on Ultrasonics, Ferroelectrics, and Frequency Control*, vol. 39, no. 3, pp. 381–397, 1992.

[60] M. J. Lowe and O. Diligent, "Low-frequency reflection characteristics of the S_0 Lamb wave from a rectangular notch in a plate," *Journal of the Acoustical Society of America*, vol. 111, no. 1, pp. 64–74, 2002.

[61] M. J. S. Lowe, P. Cawley, J. Y. Kao, and O. Diligent, "The low frequency reflection characteristics of the fundamental antisymmetric Lamb wave A_0 from a rectangular notch in a plate," *Journal of the Acoustical Society of America*, vol. 112, no. 6, pp. 2612–2622, 2002.

[62] Y. Lu, L. Ye, Z. Su, and C. Yang, "Quantitative assessment of through-thickness crack size based on Lamb wave scattering in aluminium plates," *NDT & E International*, vol. 41, no. 1, pp. 59–68, 2008.

[63] Z. Chang and A. Mal, "Scattering of Lamb waves from a rivet hole with edge cracks," *Mechanics of Materials*, vol. 31, no. 3, pp. 197–204, 1999.

[64] H. Cho and C. J. Lissenden, "Structural health monitoring of fatigue crack growth in plate structures with ultrasonic guided waves," *Structural Health Monitoring*, vol. 11, no. 4, pp. 393–404, 2012.

[65] P. Fromme and M. B. Sayir, "Detection of cracks at rivet holes using guided waves," *Ultrasonics*, vol. 40, no. 1, pp. 199–203, 2002.

[66] S. Rokhlin, "Lamb wave interaction with lap-shear adhesive joints: Theory and experiment," *Journal of the Acoustical Society of America*, vol. 89, no. 6, pp. 2758–2765, 1991.

[67] M. J. Lowe, R. E. Challis, and C. Chan, "The transmission of Lamb waves across adhesively bonded lap joints," *Journal of the Acoustical Society of America*, vol. 107, no. 3, pp. 1333–1345, 2000.

[68] F. Lanza di Scalea, P. Rizzo, and A. Marzani, "Propagation of ultrasonic guided waves in lap-shear adhesive joints: Case of incident A_0 Lamb wave," *Journal of the Acoustical Society of America*, vol. 115, no. 1, pp. 146–156, 2004.

[69] F. Bendec, M. Peretz, and S. Rokhlin, "Ultrasonic Lamb wave method for sizing of spot welds," *Ultrasonics*, vol. 22, no. 2, pp. 78–84, 1984.

[70] Y. Al-Nassar, S. Datta, and A. Shah, "Scattering of Lamb waves by a normal rectangular strip weldment," *Ultrasonics*, vol. 29, no. 2, pp. 125–132, 1991.

[71] Y. Cho, D. D. Hongerholt, and J. L. Rose, "Lamb wave scattering analysis for reflector characterization," *IEEE Transactions on Ultrasonics, Ferroelectrics, and Frequency Control*, vol. 44, no. 1, pp. 44–52, 1997.

[72] L. Moreau, A. Velichko, and P. D. Wilcox, "Accurate finite element modelling of guided wave scattering from irregular defects," *NDT & E International*, vol. 45, no. 1, pp. 46–54, 2012.

[73] N. Guo and P. Cawley, "The interaction of Lamb waves with delaminations in composite laminates," *Journal of the Acoustical Society of America*, vol. 94, no. 4, pp. 2240–2246, 1993.

[74] C.-T. Ng and M. Veidt, "Scattering of the fundamental anti-symmetric Lamb wave at delaminations in composite laminates," *Journal of the Acoustical Society of America*, vol. 129, no. 3, pp. 1288–1296, 2011.

[75] H. Gao, Y. Shi, and J. Rose, "Guided wave tomography on an aircraft wing with leave in place sensors," in *AIP Conference Proceedings-American Institute of Physics*, vol. 760, pp. 1788–1794, 2005.

[76] X. P. Qing, H.-L. Chan, S. J. Beard, and A. Kumar, "An active diagnostic system for structural health monitoring of rocket engines," *Journal of Intelligent Material Systems and Structures*, vol. 17, no. 7, pp. 619–628, 2006.

[77] A. Mal, F. Ricci, S. Banerjee, and F. Shih, "A conceptual structural health monitoring system based on vibration and wave propagation," *Structural Health Monitoring*, vol. 4, no. 3, pp. 283–293, 2005.

[78] S. Banerjee, F. Ricci, E. Monaco, and A. Mal, "A wave propagation and vibration-based approach for damage identification in structural components," *Journal of Sound and Vibration*, vol. 322, no. 1, pp. 167–183, 2009.

[79] J.-B. Ihn and F.-K. Chang, "Detection and monitoring of hidden fatigue crack growth using a built-in piezoelectric sensor/actuator network: I. diagnostics," *Smart Materials and Structures*, vol. 13, no. 3, pp. 609–620, 2004.

[80] H. Sohn, G. Park, J. R. Wait, N. P. Limback, and C. R. Farrar, "Wavelet-based active sensing for delamination detection in composite structures," *Smart Materials and Structures*, vol. 13, no. 1, pp. 153–160, 2004.

[81] S. B. Kim and H. Sohn, "Instantaneous reference-free crack detection based on polarization characteristics of piezoelectric materials," *Smart Materials and Structures*, vol. 16, no. 6, pp. 2375–2387, 2007.

[82] S. R. Anton, D. J. Inman, and G. Park, "Reference-free damage detection using instantaneous baseline measurements," *AIAA journal*, vol. 47, no. 8, pp. 1952–1964, 2009.

[83] H. Sohn, H. W. Park, K. H. Law, and C. R. Farrar, "Combination of a time reversal process and a consecutive outlier analysis for baseline-free damage diagnosis," *Journal of Intelligent Material Systems and Structures*, vol. 18, no. 4, pp. 335–346, 2007.

[84] H. W. Park, H. Sohn, K. H. Law, and C. R. Farrar, "Time reversal active sensing for health monitoring of a composite plate," *Journal of Sound and Vibration*, vol. 302, no. 1, pp. 50–66, 2007.

[85] W. Ostachowicz, P. Kudela, P. Malinowski, and T. Wandowski, "Damage localisation in plate-like structures based on PZT sensors," *Mechanical Systems and Signal Processing*, vol. 23, no. 6, pp. 1805–1829, 2009.

[86] M. Engholm and T. Stepinski, "Adaptive beamforming for array imaging of plate structures using Lamb waves," *IEEE Transactions on Ultrasonics, Ferroelectrics, and Frequency Control*, vol. 57, no. 12, pp. 2712–2724, 2010.

[87] S. E. Olson, M. P. DeSimio, and M. M. Derriso, "Beam forming of Lamb waves for structural health monitoring," *Journal of Vibration and Acoustics*, vol. 129, no. 6, pp. 730–738, 2007.

[88] A. Velichko and P. D. Wilcox, "Guided wave arrays for high resolution inspection," *Journal of the Acoustical Society of America*, vol. 123, no. 1, pp. 186–196, 2008.

[89] T. Hay, R. Royer, H. Gao, X. Zhao, and J. Rose, "A comparison of embedded sensor Lamb wave ultrasonic tomography approaches for material loss detection," *Smart Materials and Structures*, vol. 15, no. 4, pp. 946–951, 2006.

[90] X. Zhao, H. Gao, G. Zhang, B. Ayhan, F. Yan, C. Kwan, and J. L. Rose, "Active health monitoring of an aircraft wing with embedded piezoelectric sensor/actuator network: I. Defect detection, localization and growth monitoring," *Smart Materials and Structures*, vol. 16, no. 4, pp. 1208–1217, 2007.

[91] X. Zhao, R. L. Royer, S. E. Owens, and J. L. Rose, "Ultrasonic Lamb wave tomography in structural health monitoring," *Smart Materials and Structures*, vol. 20, no. 10, pp. 105002–105011, 2011.

[92] J. E. Michaels and T. E. Michaels, "Enhanced differential methods for guided wave phased array imaging using spatially distributed piezoelectric transducers," in *AIP Conference Proceedings-American Institute of Physics*, vol. 820, pp. 837–844, 2006.

[93] J. E. Michaels, A. J. Croxford, and P. D. Wilcox, "Imaging algorithms for locating damage via *in situ* ultrasonic sensors," in *Proceedings of the IEEE Sensors Applications Symposium*, pp. 63–67, 2008.

[94] A. J. Croxford, P. D. Wilcox, and B. W. Drinkwater, "Guided wave SHM with a distributed sensor network," in *Proceedings of SPIE*, vol. 6935, pp. 69350E1–69350E9, 2008.

[95] E. B. Flynn, M. D. Todd, P. D. Wilcox, B. W. Drinkwater, and A. J. Croxford, "Maximum-likelihood estimation of damage location in guided-wave structural health monitoring," *Proceedings of the Royal Society A: Mathematical, Physical and Engineering Science*, vol. 467, no. 2133, pp. 2575–2596, 2011.

[96] F. Lanza di Scalea and S. Salamone, "Temperature effects in ultrasonic Lamb wave structural health monitoring systems," *Journal of the Acoustical Society of America*, vol. 124, pp. 161–174, 2008.

[97] A. Raghavan and C. E. Cesnik, "Effects of elevated temperature on guided-wave structural health monitoring," *Journal of Intelligent Material Systems and Structures*, vol. 19, no. 12, pp. 1383–1398, 2008.

[98] Y. Lu and J. E. Michaels, "A methodology for structural health monitoring with diffuse ultrasonic waves in the presence of temperature variations," *Ultrasonics*, vol. 43, no. 9, pp. 717–731, 2005.

[99] G. Konstantinidis, B. W. Drinkwater, and P. D. Wilcox, "The temperature stability of guided wave structural health monitoring systems," *Smart Materials and Structures*, vol. 15, no. 4, pp. 967–976, 2006.

[100] T. Clarke, F. Simonetti, and P. Cawley, "Guided wave health monitoring of complex structures by sparse array systems: Influence of temperature changes on performance," *Journal of Sound and Vibration*, vol. 329, no. 12, pp. 2306–2322, 2010.

[101] A. J. Croxford, J. Moll, P. D. Wilcox, and J. E. Michaels, "Efficient temperature compensation strategies for guided wave structural health monitoring," *Ultrasonics*, vol. 50, no. 4, pp. 517–528, 2010.

[102] R. Watkins, W. Cooper, A. Gillespie, and R. Pike, "The attenuation of Lamb waves in the presence of a fluid," *Ultrasonics*, vol. 20, no. 6, pp. 257–264, 1982.

[103] J. Sharma and V. Pathania, "Generalized thermoelastic Lamb waves in a plate bordered with layers of inviscid liquid," *Journal of Sound and Vibration*, vol. 268, no. 5, pp. 897–916, 2003.

[104] J. Wu and Z. Zhu, "The propagation of Lamb waves in a plate bordered with layers of a liquid," *Journal of the Acoustical Society of America*, vol. 91, no. 2, pp. 861–867, 1992.

[105] Z. Zhu and J. Wu, "The propagation of Lamb waves in a plate bordered with a viscous liquid," *Journal of the Acoustical Society of America*, vol. 98, no. 2, pp. 1057–1064, 1995.

[106] Y. Lu and J. E. Michaels, "Feature extraction and sensor fusion for ultrasonic structural health monitoring under changing environmental conditions," *IEEE Sensors Journal*, vol. 9, no. 11, pp. 1462–1471, 2009.

[107] H. Li, J. E. Michaels, S. J. Lee, and T. E. Michaels, "Quantification of surface wetting in plate-like structures via guided waves," in *AIP Conference Proceedings-American Institute of Physics*, vol. 1430, pp. 217–224, 2012.

[108] D. Husson, "A perturbation theory for the acoustoelastic effect of surface waves," *Journal of Applied Physics*, vol. 57, no. 5, pp. 1562–1568, 1985.

[109] J. Qu and G. Liu, "Effects of residual stress on guided waves in layered media," in *Review of Progress in Quantitative Nondestructive Evaluation*, vol. 17, pp. 1635–1642, 1998.

[110] P. Rizzo and F. Lanza di Scalea, "Effect of frequency on the acoustoelastic response of steel bars," *Experimental Techniques*, vol. 27, no. 6, pp. 40–43, 2003.

[111] F. Chen and P. D. Wilcox, "The effect of load on guided wave propagation," *Ultrasonics*, vol. 47, no. 1, pp. 111–122, 2007.

[112] Y.-K. An and H. Sohn, "Instantaneous crack detection under varying temperature and static loading conditions," *Structural Control and Health Monitoring*, vol. 17, no. 7, pp. 730–741, 2010.

[113] F. Song, G. Huang, and G. Hu, "Coupled piezo-elastodynamic modeling of guided wave excitation and propagation in plates with applied prestresses,"

Journal of Intelligent Material Systems and Structures, vol. 24, no. 5, pp. 598–611, 2013.

[114] N. Gandhi, J. E. Michaels, and S. J. Lee, "Acoustoelastic Lamb wave propagation in biaxially stressed plates," *Journal of the Acoustical Society of America*, vol. 132, no. 3, pp. 1284–1293, 2012.

[115] A. Pilarski, J. J. Ditri, K. Rajana, and J. L. Rose, "Utilization of non zero-order symmetric Lamb wave modes at the first critical angle," in *Review of Progress in Quantitative Nondestructive Evaluation*, vol. 13, pp. 173–179, 1994.

[116] F. Lanza di Scalea, P. Rizzo, and F. Seible, "Stress measurement and defect detection in steel strands by guided stress waves," *Journal of Materials in Civil Engineering*, vol. 15, no. 3, pp. 219–227, 2003.

[117] F. Shi, J. E. Michaels, and S. J. Lee, "*In situ* estimation of applied biaxial loads with Lamb waves," *Journal of the Acoustical Society of America*, vol. 133, no. 2, pp. 677–687, 2013.

[118] J. Frandsen, R. Inman, and O. Buck, "A comparison of acoustic and strain gauge techniques for crack closure," *International Journal of Fracture*, vol. 11, no. 2, pp. 345–348, 1975.

[119] R. Clark, W. Dover, and L. Bond, "The effect of crack closure on the reliability of NDT predictions of crack size," *NDT International*, vol. 20, no. 5, pp. 269–275, 1987.

[120] J.-Y. Kim, V. Yakovlev, and S. Rokhlin, "Surface acoustic wave modulation on a partially closed fatigue crack," *Journal of the Acoustical Society of America*, vol. 115, no. 5, pp. 1961–1972, 2004.

[121] B. Mi, J. E. Michaels, and T. E. Michaels, "An ultrasonic method for dynamic monitoring of fatigue crack initiation and growth," *Journal of the Acoustical Society of America*, vol. 119, no. 1, pp. 74–85, 2006.

[122] G. Connolly and S. Rokhlin, "Enhancement of fatigue crack monitoring by surface acoustic wave reflection and modulation in a space-cycle-load domain: an imaging approach," *Structural Health Monitoring*, vol. 11, no. 2, pp. 187–196, 2012.

[123] Y. Ohara, S. Horinouchi, M. Hashimoto, Y. Shintaku, and K. Yamanaka, "Nonlinear ultrasonic imaging method for closed cracks using subtraction of responses at different external loads," *Ultrasonics*, vol. 51, no. 6, pp. 661–666, 2011.

[124] J. Bao and V. Giurgiutiu, "Effects of fastener load on wave propagation through lap joint," in *Proceedings of the SPIE*, vol. 8695, pp. 86952101–86952112, 2013.

[125] S. Park, C.-B. Yun, Y. Roh, and J.-J. Lee, "PZT-based active damage detection techniques for steel bridge components," *Smart Materials and Structures*, vol. 15, no. 4, pp. 957–966, 2006.

[126] D. Doyle, A. Zagrai, B. Arritt, and H. Çakan, "Damage detection in bolted space structures," *Journal of Intelligent Material Systems and Structures*, vol. 21, no. 3, pp. 251–264, 2010.

[127] T. Kundu, A. Maji, T. Ghosh, and K. Maslov, "Detection of kissing bonds by Lamb waves," *Ultrasonics*, vol. 35, no. 8, pp. 573–580, 1998.

[128] B. W. Drinkwater, R. S. Dwyer-Joyce, and P. Cawley, "A study of the interaction between ultrasound and a partially contacting solid–solid interface," *Proceedings of the Royal Society of London. Series A: Mathematical, Physical and Engineering Sciences*, vol. 452, no. 1955, pp. 2613–2628, 1996.

[129] C. J. Brotherhood, B. W. Drinkwater, and S. Dixon, "The detectability of kissing bonds in adhesive joints using ultrasonic techniques," *Ultrasonics*, vol. 41, no. 7, pp. 521–529, 2003.

[130] B. W. Drinkwater, M. Castaings, and B. Hosten, "The measurement of A_0 and S_0 Lamb wave attenuation to determine the normal and shear stiffnesses of a compressively loaded interface," *Journal of the Acoustical Society of America*, vol. 113, no. 6, pp. 3161–3170, 2003.

[131] P. D. Wilcox and A. Velichko, "Efficient frequency-domain finite element modeling of two-dimensional elastodynamic scattering," *Journal of the Acoustical Society of America*, vol. 127, no. 1, pp. 155–165, 2010.

[132] P. D. Wilcox, "A rapid signal processing technique to remove the effect of dispersion from guided wave signals," *IEEE Transactions on Ultrasonics, Ferroelectrics, and Frequency Control*, vol. 50, no. 4, pp. 419–427, 2003.

[133] L. Liu and F. Yuan, "A linear mapping technique for dispersion removal of Lamb waves," *Structural Health Monitoring*, vol. 9, no. 1, pp. 75–86, 2010.

[134] M. D. Buhmann, *Radial Basis Functions: Theory and Implementations*. Cambridge University Press, 2003.

[135] C. A. Micchelli, *Interpolation of Scattered Data: Distance Matrices and Conditionally Positive Definite Functions*. Springer, 1984.

[136] R. Franke, "Scattered data interpolation: Tests of some methods," *Mathematics of Computation*, vol. 38, no. 157, pp. 181–200, 1982.

[137] E. J. Kansa, "Multiquadrics–a scattered data approximation scheme with applications to computational fluid-dynamics–I. Surface approximations and partial

derivative estimates," *Computers & Mathematics with Applications*, vol. 19, no. 8, pp. 127–145, 1990.

[138] B. Fornberg and G. Wright, "Stable computation of multiquadric interpolants for all values of the shape parameter," *Computers & Mathematics with Applications*, vol. 48, no. 5, pp. 853–867, 2004.

[139] R. Schaback, "Error estimates and condition numbers for radial basis function interpolation," *Advances in Computational Mathematics*, vol. 3, no. 3, pp. 251–264, 1995.

[140] R. L. Hardy, "Multiquadric equations of topography and other irregular surfaces," *Journal of Geophysical Research*, vol. 76, no. 8, pp. 1905–1915, 1971.

[141] G. E. Fasshauer and J. G. Zhang, "On choosing "optimal" shape parameters for RBF approximation," *Numerical Algorithms*, vol. 45, no. 1-4, pp. 345–368, 2007.

[142] W. Madych and S. Nelson, "Bounds on multivariate polynomials and exponential error estimates for multiquadric interpolation," *Journal of Approximation Theory*, vol. 70, no. 1, pp. 94–114, 1992.

[143] Z.-M. Wu and R. Schaback, "Local error estimates for radial basis function interpolation of scattered data," *IMA journal of Numerical Analysis*, vol. 13, no. 1, pp. 13–27, 1993.

[144] E. B. Flynn, M. D. Todd, A. J. Croxford, B. W. Drinkwater, and P. D. Wilcox, "Enhanced detection through low-order stochastic modeling for guided-wave structural health monitoring," *Structural Health Monitoring*, vol. 11, no. 2, pp. 149–160, 2012.

[145] J. S. Hall and J. E. Michaels, "Computational efficiency of ultrasonic guided wave imaging algorithms," *IEEE Transactions on Ultrasonics, Ferroelectrics, and Frequency Control*, vol. 58, no. 1, pp. 244–248, 2011.

[146] W. Burger, M. J. Burge, M. J. Burge, and M. J. Burge, *Principles of Digital Image Processing*. Springer, 2009.